Title
SCATTERING OF NOBLE GAS METASTABLE ATOMS IN MOLECULAR BEAMS

Permalink
https://escholarship.org/uc/item/99c7182k

Author
Haberland, H.

Publication Date
1979-03-01

To be published as a Chapter in
THE EXCITED STATE IN CHEMICAL PHYSICS,
PART 2, J. Wm. McGowan, ed., New York:
Wiley-Interscience, Inc.

SCATTERING OF NOBLE GAS METASTABLE ATOMS IN MOLECULAR BEAMS

H. Haberland, Y. T. Lee, and P. E. Siska

March 1979

Prepared for the U. S. Department of Energy
under Contract W-7405-ENG-48

DISCLAIMER

LBL-8959

SCATTERING OF NOBLE GAS METASTABLE ATOMS IN MOLECULAR BEAMS

H. Haberland
Fakultät für Physik der Universität Freiburg
Freiburg im Breisgau, West Germany

Y. T. Lee
Department of Chemistry and Lawrence Berkeley Laboratory
University of California, Berkeley California 94720

P. E. Siska
Department of Chemistry
University of Pittsburgh, Pittsburgh, Pennsylvania 15260

(submitted to Advances in Chemical Physics)

CONTENTS

I. Introduction

Although the important role played by metastable noble gas atoms in the ionization process was recognized as long as half a century ago, investigations of microscopic processes involving metastable noble gas atoms have only recently become one of the more active research areas.

In 1927 Frans Michel Penning (1894-1953) at Philips Laboratories discovered that breakdown voltages and the ionization coefficients of neon and argon were markedly influenced by the addition of minute impurities, and concluded from a series of experiments that the impurities were ionized by energy transfer from metastable neon or argon atoms that were present in discharges.[1] In addition to Penning ionization, one other type of ionization process involving electronically excited atoms was also observed in the 1920's and 1930's. It was found that the vapors of cesium and rubidium can be photoionized by light in the discrete absorption region of the atomic spectra with energy less than the atomic ionization energy.[2-5] The proper explanation of this ionization process was given by Franck[6] in 1928, as associative ionization to form diatomic molecule ions in two body collisions between an excited atom and a ground state atom; this was verified by Mohler and Boeckner in their quantitative study of the formation of Cs_2^+ in 1930.[7]

It was twenty years before the important microscopic precesses involved in early findings were "re-discovered" in several studies. In 1951, Hornbeck and Molnar[8] carried out the first thorough examination of the formation of molecule ions from electronically excited noble gases in a mass spectrometer. The presence of molecule ions was shown to be due to associative ionization, and this process is now often referred to as the Hornbeck-Molnar process in recognition of their work. In 1949, Jesse[9] discovered in his studies of high energy ionizing radiations, such as alpha and beta particles, that the absorbed energy per ion pair produced in helium gas was extremely sensitive to the presence of minute amounts of almost any impurity.[10] This sensitivity is called the Jesse effect in the field of radiation research. Although the Penning and Jesse effects describe different macroscopic phenomena, the microscopic processes which produce these effects, mainly Penning and associative ionization, are undoubtedly the same.

Substantial advances in the understanding of microscopic processes of electronically excited atoms began only in the 1960's, when improvements in experimental methods and available technology allowed scientists to obtain quantitative microscopic information under well defined conditions. This is especially true for metastable noble gas atoms. Because the lifetimes of metastable noble gas atoms are much longer than the transit time of atoms in a typical high-vacuum apparatus, $\sim 10^{-3}$ sec, it became possible to perform experiments under the single collision conditions of the molecular beam. The measurements of ionization cross sections via total ion collection by Sholette and Muschlitz[9], the velocity dependence of the total scattering cross sections by Rothe, Neynaber and Trujillo[10] and the studies of energy distributions of electrons from Penning ionization by Cermák[11] mark the beginning of a rapid growth in the amount of information related to the dynamics of microscopic processes involving metastable noble gas atoms.

Many of the chemical and dynamical properties of metastable noble gas atoms can be easily appreciated by noting that their excitation energies are higher than the ionization potentials of many diatomic and polyatomic molecules, and their polarizabilities and ionization potentials are quite close to those of alkali atoms. In addition, the long lifetime, which prevents radiative decay from competing with the efficient conversion of stored energy in collisional processes, makes it possible to use energy transfer from metastable noble gas atoms as pumping processes for gas lasers. Table I lists some important properties of metastable noble gas atoms, and Figure 1 illustrates them.

The interactions between metastable noble gas atoms and ground state noble gas atoms are relatively simple and have been investigated quite extensively. If the excitation energy is lower than the ionization potential of the collision partner, the only important inelastic process is the transfer of excitation energy.[12] The excitation transfer is usually very efficient when the process is near resonant. The process which is responsible for the operation of the He-Ne laser,[13]

$He^*(2^1S) + Ne \rightarrow He + Ne^*(3s)$ Excitation Transfer

is one such example. The other type of excitation transfer is the formation of excimers. For example, in the process

$Xe^* + Xe \rightarrow Xe_2^* \rightarrow 2Xe + h\nu$ Excimer Formation

the delocalization of excitation energy from one atom to two causes a drastic decrease in the radiative lifetime. The excitation energy is then transformed into a photon and the kinetic energy between two ground state atoms. The excimer laser is based on this process.[14-16] If the ground state atom has a lower ionization potential than the excitation energy of the metastable atom, energy transfer collisions will mainly take the form of ionization processes.[17,18] For example, the reaction

$He^*(2^1S,\ 2^3S) + Ar \rightarrow He + Ar^+ + e$ Penning ionization

$\rightarrow HeAr^+ + e$ Associative ionization

produces both atomic and molecular ions through Penning and associative ionization processes. There is no mechanistic difference between Penning and associative ionization with regard to electronic energy transfer. Whether a specific two body collision will produce an atomic or molecular ion depends entirely on whether the electron ejected will remove sufficient energy to leave He-Ar$^+$ in a bound negative energy state.

Since the electronic motion is only weakly coupled to the motion of the nuclei, the kinetic energy of the electron ejected is approximately the difference between the potential energies of the ionic state and the excited state at an internuclear distance where the transition takes place. Consequently, if the gain in potential energy during the transition is larger than the kinetic energy, a molecular ion will be formed. Of course, the transition probability as a function of internuclear distance not only depends on the coupling between the excited state and the ionic state, but also on the kinematic conditions such as relative kinetic energy and orbital angular momentum.

In the interactions between metastable atoms and diatomic and polyatomic molecules, excitation transfer and ionization processes may proceed initially with mechanisms similar to those with ground state noble gas atoms, but the outcome of the process is often more complicated.[12] After excitation transfer, the newly formed electronically excited molecules sometimes dissociate before the excitation energy is removed by radiative decay; while after ionization, in addition to possible dissociation of excited molecule ions, ion-molecule rearrangements may also occur. However, there is a type of interaction of metastable noble gas atoms with molecules which is fundamentally different from the interaction with noble gas atoms. Since the ionization potentials of metastable noble gas atoms are comparable to those of the corresponding alkali atoms, the interactions with molecules with appreciable electron affinities, such as diatomic halogen molecules or certain halogen-containing polyatomic molecules, may proceed initially with electron transfer from the metastable atom to the molecule. This is followed by the formation of an electronically excited rare gas halide molecule in a reaction similar to the formation of an alkali halide by the "harpooning" mechanism.[19] For example,[20]

$$Xe^* + F_2 \rightarrow [Xe^+F_2^-] \rightarrow XeF^* + F$$

This alkali-like behavior of metastable noble gas atoms effectively transforms the excitation energy of the metastable noble gas atom into electronic energy of a rare gas halide molecule with large reaction cross section. Because the electronically excited noble gas halides have short radiative lifetimes and the ground state noble gas halides are not strongly bound, the process of formation of electronically excited noble gas halides from metastable noble gas atoms has been shown to be ideal for the operation of the electronic transition laser, and has been successfully used in high efficiency rare gas halide lasers in recent years.[21-23]

Accompanying the recent improvements in the microscopic experiments exploring the dynamics of elementary processes involving metastable noble gas atoms, there also have been substantial advances in the theory,[24-25] especially for the ionization processes involving metastable noble gas and ground state atoms or simple diatomic molecules. For simple systems, such as $He^* + H$ and $He^* + H_2$, it has become possible to calculate the interaction potentials in the excited state and the ionic state and the coupling strength between the resonance and continuum states from first principles.[26,27] The collision process can now be described either by semiclassical or quantum mechanical treatments in terms of interaction potentials of excited states and ionic states and the coupling strength between them.[27-29] Indeed, if one knows these quantities, direct calculations of such observables as Penning electron energy spectra, velocity dependence of the ionization cross section, the branching ratio between Penning and associative ionization, and total and differential elastic scattering cross sections are reasonably straightforward. On the other hand, accurate results of microscopic experiments will enable us to understand the details of reaction dynamics by finding, in terms of an optical potential model,[30,31] the real and imaginary parts of of the interaction potentials between metastable noble gas atoms and ground state atoms, and the interaction potentials of ionic states. The advancement in this direction is best exemplified in the pioneering experiments of Niehaus and coworkers in Penning electron and ion spectroscopy,[17,18,32] and differential elastic scattering cross section measurements which will be discussed in this chapter. But the derivation of these quantities from microscopic experiments is by no means simple, because three quantities must be determined as a function of internuclear distance, and the observations might only reflect certain relations between these quantities. For example, Penning electron spectra are sensitive to the difference between the potentials of the excited state and the ionic state and its relation to the imaginary part of the potential. Consequently, only if one knows the real part of the potential of the excited state or the potential of the ionic state accurately, will it become possible to derive the imaginary part of the potential and the other interaction potential by measuring Penning electron spectra, preferably at more than one collision energy. Total ionization cross sections as a function of collision energy provide a range of combinations of real and imaginary parts of the potential which gives a satisfactory description of experimental results; the determination of these quantities from such measurements alone is not considered unique.[33] For a given real and imaginary part of the excited potential, it is possible to derive the potential of the ionic state by combining measurements of the branching ratio between Penning and associative ionization and of the total ionization cross section as a function of collision energy. It is clear that the precise determination of these potentials requires more than one type of precise microscopic experiments, and it is also important to include the type of microscopic experiment which is particularly sensitive to one or two of the potential functions.[33] Consequently, the measurements of elastic differential cross sections of the metastable noble gas atoms not only supplement Penning electron spectra and total ionization cross sections as a function of collision energy, but also contribute significantly to the understanding of the dynamics of the collisions of metastable noble gas atoms.

It is well known that one of the most direct and reliable methods of obtaining detailed information on interaction potentials of atomic systems is the measurement of elastic scattering cross sections.[34] In the past decade, precise interaction potentials for alkali-mercury, alkali-noble gas and noble gas-noble gas systems have been derived mainly from high resolution crossed molecular beams measurements of scattering intensities as a function of scattering angle at several collision energies. Well resolved structures in the differential elastic scattering cross sections, such as rainbows, supernumerary rainbows and fast oscillations, as well as measurements covering a wide angular range, are necessary for the precise determination of interaction potentials. It has also been shown in studies of reactive systems, such as alkali atoms with diatomic halogen molecules or halogen containing polyatomic molecules, that it is possible to derive some information on the reaction probability as a function of the impact parameter from depletion of the elastic scattering cross section due to chemical reaction.[35]

Crossed molecular beam studies of differential scattering of metastable noble gas atoms with ground state noble gas atoms or simple molecules is the major topic of this chapter. These studies have been carried out recently at several laboratories with the same purpose of finding both real and imaginary parts of the interaction potentials in order to further our understanding of the dynamics of collision processes involving metastable noble gas atoms.

Experimentally, the scattering studies of metastable noble gas atoms enjoy an advantage similar to that of alkali atom experiments in the ease of detection of metastable atoms. The high specificity of the detection of metastable noble gas atoms by Auger electron emission,[36] similar in some sense to the detection of alkali atoms by a hot wire detector, is immune to the presence of background gas, whose collision rate with the detector surface is usually many orders of magnitude higher than that of the scattered metastable atoms. This is part of the reason why so much information has been obtained with relatively modest experimental arrangements in a rather short period of time. Of course, the development of the high intensity, monoenergetic free jet molecular beam source[37,38] in the past decade has also contributed significantly to the possibility of carrying out differential scattering cross section measurements efficiently and with reasonably high resolution, so as to provide reliable information on interaction potentials. The first precise differential scattering cross section measurements of metastable rare gas atoms by Chen, Haberland and Lee,[39] and by Winicur and collaborators[40] as well as more extensive studies of Haberland and Siska and their coworkers are all carried out with a free jet beam source.

In this chapter, we will summarize the current status of the low energy scattering of noble gas metastable atoms in molecular beams. A brief summary of potential scattering theory which is relevant to the understanding of collision dynamics, as well as a description of the experimental method, will precede the presentation of experimental findings. The experimental results which will be presented are mainly from the authors' laboratories.

As will be seen here and in other related chapters in this volume, the field of collision dynamics of metastable noble gas atoms had made some significant advances in recent years. These advances undoubtedly will give some insight into many macroscopic phenomena involving metastable noble gas atoms. The recent development of several potentially useful lasers involving noble gas atoms makes the understanding of the collision dynamics of elementary processes involving metastable noble gas atoms even more important. We hope this chapter will serve as a useful guide to the kind and quality of information obtainable on metastable noble gas atom interactions from beam scattering methods.

II. Brief Summary of Potential Scattering Theory

Two-body collision theory for a central potential can be applied with a rigor limited mainly by the Born-Oppenheimer approximation to a large and interesting class of metastable noble gas collisions, viz., those with other atomic species. In the atom-atom cases, even when electronically inelastic channels are open, the optical model may often be applied to describe the effect on the elastic scattering. If only a few channels are important, a close-coupling treatment is feasible because of the absence of rotational and vibrational degrees of freedom and the consequent reduction in computational effort. Penning ionization is an excellent case for the application of the optical model, since the rapid departure of the Penning electron makes the process irreversible. Excitation transfer in systems such as Ar^* + Kr or He^* + Ne promises to be analyzable in a close-coupling framework with only a few states included, and analysis of the elastic scattering using a simple optical model may be adequate if the coupling is weak. Analysis of product angular distributions, of course, requires a complete close-coupling description.

Collisions with diatomic and polyatomic molecules are as usual difficult to describe due to the internal degrees of freedom, as well as to the anisotropy in the potential function. For many target molecules involved in Penning ionization, however, nearly vertical ionization occurs as indicated by Franck-Condon vibrational populations, thus inviting treatment neglecting the internal degrees of freedom. Particularly at the level of Penning ion product angular distributions, small molecules often give results very similar to the atomic cases. Effects of vibrational and rotational inelasticity and potential anisotropy prevent the extraction of truly quantitative information from nonreactive scattering with molecules, but analysis of these data using two-body mechanics can still be of value.

Many books and reviews give exemplary treatments of two-body collision theory, especially for our purposes those treating molecular collisions.[41-45] We shall therefore confine ourselves to brief discussion and statement of results essential to understanding the differential scattering, giving where possible both quantum and classical mechanical formulae.

II.A. Elastic Differential Scattering in Nonreactive Systems

In the absence of inelastic processes, and assuming a single potential curve, the outcome of a collision, specified by the relative energy E, collisional reduced mass μ, and impact parameter b or angular momentum quantum number ℓ, is described classically by the deflection angle $\chi(b,E)$ or quantally by the phase shift $\eta_\ell(E)$, both asymptotic quantities. In the semiclassical (large ℓ) limit, we may identify $\ell + \frac{1}{2} = kb$, k the wavenumber $(2\mu E)^{1/2}/\hbar$, and $\chi = 2\,\partial\eta_\ell/\partial\ell$. In terms of these, the differential cross section is given by

$$\sigma_C(\theta,E) = \sum_i b_i/(\sin\theta\,|\partial\chi(b,E)/\partial b|_{b_i});\quad |\chi\,(b_i,E)|_{\text{mod }\pi} = \theta \qquad (1)$$

classically, and

$$\sigma_Q(\theta,E) = |f(\theta,E)|^2 \qquad (2)$$

quantally, with the scattering amplitude

$$f(\theta,E) = (2ik)^{-1} \sum_\ell (2\ell+1)(e^{2i\eta_\ell(E)} - 1)P_\ell(\cos\theta). \qquad (3)$$

χ may be obtained from the potential V(r) by a simple quadrature,

$$\chi(b,E) = \pi - 2b \int_{r_0(b,E)}^{\infty} \frac{dr}{r^2[1-V(r)/E - b^2/r^2]^{1/2}} , \tag{4}$$

$r_0(b,E)$ the outermost turning point, while η results from integration of the radial Schrödinger equation,

$$\frac{d^2G_\ell(r)}{dr^2} + k^2[1 - \frac{V(r)}{E} - \frac{\ell(\ell+1)}{k^2r^2}]\, G_\ell(r) = 0, \tag{5}$$

into the asymptotic region, where the solution becomes

$$G_\ell(r) \sim kr\,[\sin\eta_\ell j_\ell(kr) - \cos\eta_\ell n_\ell(kr)], \tag{6}$$

j_ℓ, n_ℓ the spherical bessel and neumann functions respectively. Semi-classically, $\chi = 2\partial\eta_\ell/\partial\ell$ may be employed to give the JWKB expression,

$$\eta_\ell = \frac{\pi}{2}(\ell + \frac{1}{2}) - kr_0 + k \int_{r_0}^{\infty} \{[1 - \frac{V(r)}{E} - \frac{(\ell+\frac{1}{2})^2}{k^2r^2}]^{\frac{1}{2}} - 1\}dr, \tag{7}$$

which yields very accurate molecular cross sections when substituted in Eq. (3).

We note that, formally, the scattering angle θ bears no necessary relation to the angular momentum ℓ in quantum mechanics [Eq. (3)], while classically a given b leads uniquely to a deflection angle χ through a classical trajectory. In the limit of large ℓ, however, stationary phase regions of the summand in Eq. (3) lead to different groups of ℓ-values each contributing mainly to a small range of angles. Thus, for molecular collisions, where the sum in Eq. (3) generally extends to $\ell \sim 10^2$-10^4, a close connection persists between the results of quantum calculations and the classical picture. Interference features in the differential cross section, such as rainbow structure and the rapid oscillatory pattern often observed superimposed on it, can usually be interpreted as a superposition of two or more interfering classical trajectories.

The noble gas metastable atoms Ne^* through Xe^* are $^3P_{2,0}$ atoms, so that more than one potential energy curve governs the scattering even with S-state collision partners. Because spin-orbit interactions are large while weak van der Waals interactions imply only weak coupling to the internuclear axis, Hund's case (c) is probably the most appropriate coupling to use, with the projection Ω of the total electronic angular momentum on the internuclear axis being conserved. $^3P_2$ metastables scattering from $^1S_0$ partners thus gives $\Omega = 2, 1, 0^-$, while $^3P_0$ yields $\Omega = 0^-$ only. At the detector, $^3P_2$ atoms scattered on the various curves are indistinguishable because Ω no longer has meaning. The differential cross section is thus

$$\sigma_Q(\theta) = \left|\sqrt{\tfrac{2}{5}}\, f_2(\theta) + \sqrt{\tfrac{2}{5}}\, f_1(\theta) + \sqrt{\tfrac{1}{5}}\, f_{0^-}(\theta)\right|^2 \qquad (8)$$

for $^3P_2$ scattering, while only one amplitude contributes for $^3P_0$ scattering. Metastable helium (2^1S, 2^3S) scatters from other S-state atoms on a single potential curve. For non-S-state collision partners, the formula (8) is easily generalized to a sum over allowed values of the "good" electronic quantum number. If the coupling between the electronic angular momentum and nuclear rotation is strong, [e.g., Hund's case (d)], formulas like (8) cannot be used, as the individual angular momenta need not be conserved. A theory which accounts for intermultiplet transitions must then be invoked. On the other hand, it is possible that the Ω quantum number does not affect the electronic energy in the case of van der Waals interactions, so that only the possible values of J, the total electronic angular momentum, need be considered. Then $^3P_2 + {}^1S_0$ results in only one state or potential energy curve labelled by J = 2, and the problem for collisions with non-S-state partners is correspondingly simplified. The superposition of amplitudes in (8) may produce an interference pattern in the angular distribution, but thus far only the Ar^*-Kr system has shown any wide-angle structure (see below), and this is likely due to other effects.

II.B. Elastic Scattering in Inelastic Systems

Molecular nonreactive scattering angular distributions in systems with nonelastic channels open have been traditionally analyzed in terms of the optical model, a tool borrowed from nuclear scattering. Micha[31] has recently reviewed the use of the optical model in molecular collisions. In the quantal version of the model, the inelastic processes are viewed as removing or "absorbing" flux from each elastic partial wave (a view which is quite rigorous). Since the ratio of actual to collisionless outgoing partial wave amplitudes is given by the elastic S-matrix,

$$S_\ell = e^{2i\eta_\ell}, \tag{9}$$

attenuation of an outgoing wave can be represented by allowing the phase shift η_ℓ to take on complex values,

$$\eta_\ell = \delta_\ell + i\,\xi_\ell, \tag{10}$$

with the condition $\xi_\ell > 0$ assuring that the square modulus of S_ℓ,

$$|S_\ell|^2 = e^{-4\xi_\ell}, \tag{11}$$

is no greater than unity. It may be shown rigorously, and is easily seen by inspecting the Born approximation for η_ℓ, that a complex potential,

$$V(r) = V_0(r) - \frac{i}{2}\,\Gamma(r), \tag{12}$$

with $\Gamma(r) > 0$ gives rise to a complex phase shift, Eq. (10). $\Gamma/\hbar$ may be interpreted as the absorption rate at internuclear distance r. The quantal differential cross section formulas, Eqs. (2) and (3), remain unchanged.

cross section is then

$$\sigma_C^{inel} = 2\pi \int_0^\infty P(b)bdb, \qquad (21)$$

a formula analogous to Eq. (17). A semiclassical extension of the classical result (19) to include attenuation of the rainbow structure has been given by Harris and Wilson.[48]

The classical theory makes especially clear the inherent ambiguity of data analysis with the optical model, and this ambiguity carries over into the quantum model. If one wishes to use experimental differential cross sections to gain information about $V_0(r)$ and $P(b)$ or $\Gamma(r)$, he must assume a reasonable parametric form for $V_0(r)$ that determines the shape of the cross section "in the absence of reaction". $P(b)$ is then determined (or $\Gamma(r)$ chosen) by what is in essence an extrapolation of this parametric form. In the classical picture, a $V_0(r)$ with a less steep repulsive wall yields a lower reaction probability from the same experimental cross section data. The pair of functions $V_0(r)$, $P(b)$ or $V_0(r)$, $\Gamma(r)$ is thus underdetermined. The ambiguity may be relieved somwhat (to what extent is not yet known) by fitting several sets of data at different collision energies, and, especially, by fitting other types of data such as total elastic and/or reactive cross sections simultaneously.

II.B.1. Optical model in Penning systems

As mentioned in Section IIA, the Penning ionization (PI) process is ideal for the application of the optical model. This is clear in the classical and semiclassical PI theory,[24,25] for which opacity and cross section formulas are completely equivalent to those given above. The quantal optical model is also rigorously related to the elastic component of the quantal PI theory. Miller[49] has shown that $\Gamma(r)$, identified in PI as the autoionization width of the excited electronic state, may be accurately obtained by a standard Born-Oppenheimer electronic structure calculation as

$$\Gamma(r) = 2\pi\rho \; |\langle\phi_\varepsilon|H-E|\phi_0\rangle|^2 \qquad (22)$$

where $|\phi_0\rangle$ is the initial (discrete) electronic state, $|\phi_\varepsilon\rangle$ the final (continuum) electronic state degenerate with it, H and E the electronic Hamiltonian and energy, respectively, and ρ the density of final continuum states. The $He^*(2^3S)$-$H(1^2S)$ PI width and potential curves were the first to be calculated with some accuracy.[27] The meeting ground between ab initio PI theory and differential scattering experiments is currently in the He^*-H_2 system (see Sec. III).

II.B.2. Optical Model in Excitation Transfer Systems

In the projection operator formalism which leads to a rigorous basis for the optical potential, the absorptive imaginary part is associated with transitions out of the elastic channel from which no return occurs. While PI transitions are in this category, excitation transfer (ET) transitions are not, since return ("virtual excitation") can occur during the ET collision. In the event that a localized avoided curve-crossing with one other state dominates the inelastic process (expected for many endoergic transfers), the total absorption probability (opacity) can still be defined,

$$P_{01}(b) = 2p_{01}(1-p_{01}), \qquad (23)$$

where p_{01} is the probability of making a diabatic transition (hopping between adiabatic potential curves), and the crossing point is outside and not too near the turning point. p_{01} may be calculated by, e.g., Landau-Zener-Stückelberg (LZS) theory.[50-52] The probability of purely elastic scattering on an adiabatic incoming potential $V_0(r)$ is then

$$P_0(b) = (1-p_{01})^2 \tag{24}$$

and the probability of making two diabatic transitions (return) is

$$P_{010}(b) = p_{01}{}^2 \tag{25}$$

Naturally $P_0 + P_{01} + P_{010} = 1$. In order to apply a <u>conventional</u> optical model analysis to elastic differential scattering in an ET system, we must have $P_{010} << 1$, i.e. the probability of return must be small. If not, the "recrossing" trajectories will at least alter the relative intensities of small and wide-angle scattering, and perhaps produce new interference patterns in the angular distribution. Such effects cannot be accounted for in fitting a local absorptive optical potential to experiment, since $\Gamma(r)$ accounts only for P_{01}, i.e., absorption, and $V_0(r)$ cannot reproduce the recrossing dynamics. If V_0 is chosen as a diabatic curve, the same argument ensues with P_0 and P_{010} interchanged.

The LZS form for p_{01} is

$$\begin{aligned} p_{01} &= e^{-v_{01}/v_b} \,, \quad r_0 < r_x \\ &= 0 \qquad\quad\;\, , \quad r_0 > r_x \end{aligned} \tag{26}$$

with

$$v_{01} = 2\pi V_{01}^2(r_x)/\hbar \left|\left(\frac{dV_0}{dr} - \frac{dV_1}{dr}\right)\right|_{r_x} \tag{27}$$

where $V_0(r)$ and $V_1(r)$ are diabatic potential curves intersecting at r_x,

$V_{01}(r)$ is the nonadiabatic coupling potential, and the velocity

$$v_b = v[1 - \frac{V_0(r_x)}{E} - \frac{b^2}{{r_x}^2}]^{1/2} \tag{28}$$

The overall LZS opacity (23) may be improved for the region $r_0 \sim r_x$ by properly considering the interference between incoming and outgoing transitions.[52] This produces oscillations in $P_{01}(b)$ which may appear in the differential scattering. For n open inelastic channels accessible by pairwise curve-crossing from state 0, Eq. (23) can be generalized to give $P_{0j}(b)$ for the $0 \rightarrow j$ transition, $j < n$.[53] The total opacity for the elastic channel is then

$$P(b) = \sum_{j=1}^{n} P_{0j}(b) \tag{29}$$

The sum over states is likely to damp out any oscillations in P(b).

For exoergic channels it often happens that there is no accessible avoided crossing, in which case the trajectory assumptions underlying the LZS theory are violated. The nonadiabatic coupling region may extend over a considerable range of internuclear distance, and semiclassical methods using exact classical trajectories represent the minimal necessary improvement over LZS.

II.B.3. Close-coupling treatment in excitation transfer systems.

Assumptions limiting the usefulness of LZS theory and its extensions may be removed only at the expense of losing the closed-form solution. The coupling of LZS to an optical model analysis introduces further limitations. The optical model may be applied without recourse to the LZS interpretation of P(b), but when done rigorously it is as difficult as a two-state close-coupled calculation. Since excellent computational algorithms now exist for solving coupled sets of Schrödinger equations for many-channel scattering on today's high-speed computers, this approach has become a feasible alternative, especially if only a few channels are involved. In addition, the case of no near approach of the channel potentials can be treated on an equal footing with the familiar diabatic curve-crossing case. For two-body nonadiabatic collisions, the coupled equations are

$$\frac{d^2G^j_\ell(r)}{dr^2} + k_j^2[1 - \frac{V_j(r)}{E_j} - \frac{\ell(\ell+1)}{k_j^2r^2}]G^j_\ell(r) = k_j^2 \sum_{i\neq j}^{n} \frac{V_{ij}}{E_j}(r)G^i_\ell(r) \qquad (30)$$

$$j = 0, 1, \ldots, n$$

where $\underset{\sim}{\underset{\sim}{V}}$ is a potential matrix, chosen in most cases to be in the diabatic representation, and

$$\begin{aligned} E_j &= E_0 - V_j(\infty) \quad (V_0(\infty)\equiv 0) \qquad (31) \\ &= \hbar^2k_j^2/2\mu \end{aligned}$$

is the final kinetic energy for channel j. The equations uncouple asymptotically, and the S-matrix is obtained formally as the ratio of amplitudes of the outgoing spherical partial wave in the jth channel to the collisionless outgoing wave. Various numerical algorithms are available for evaluating the S-matrix from close-coupled solution of the equations (30).[54] The similarity between the resonant two-state equations and the optical model equations (14) is notable.

II.C. Scattering in symmetric systems with one atom excited.

When the collision partner is the ground state of the same atom as the excited one, special resonance effects come into play. Classically one may speak of "direct" and "resonant exchange" collisions, but quantally these are inextricably intertwined in principle, due to the indistinguishability of A* + A from A + A*. Proper symmetrization of the electronic wavefunction with respect to these two arrangements leads to a gerade and an ungerade electronic state for each value of the electronic angular momentum projection Ω. The identity of the atoms allows a strong "chemical" (as opposed to only van der Waals) exchange interaction with bond energies of $\sim$1 eV or more for the favorable (for the noble gases, u) overlap of the atomic wavefunctions.

The cross section may be computed from the scattering amplitudes for the g and u potentials using

$$\sigma(\theta) = \frac{1}{4}|f_g(\theta) + f_g(\pi-\theta) + f_u(\theta) - f_u(\pi-\theta)|^2 \qquad (32)$$

for spinless nuclei (^{4}He, ^{20}Ne, ^{40}Ar, ^{84}Kr, ^{132}Xe). The isotopes with nonzero spin require the admixture of a term similar to the RHS of Eq. (32) with the signs of the $\pi-\theta$ amplitudes reversed. When various projections Ω are possible, each g, u amplitude must be calculated as a weighted sum of projection amplitudes, as in Eq. (8). The expected coherent interference between $f(\theta)$ and $f(\pi-\theta)$ is similar in nature to that for symmetric ground-state scattering, as in He-He. This interference may be discussed in terms of deflection functions for the g,u potentials. A detailed discussion specialized to the case of He$^*(2^1S,2^3S)$ + He will be given in Section III.C.

II.D. Inelastic Events

II.D.1. Penning ionization heavy-particle angular distributions

In a classical picture of Penning ionization,[24] the molecules approach along a trajectory on the initial $A^* + B$ (real) potential $V_0(r)$. Ionization occurs at a specified (but random) value of the internuclear distance, r_i, and the products then complete their trajectories on an ion-molecule potential $V_+(r)$ for $A + B^+$. Neglecting the momentum of the ejected electron, deflection functions can be computed according to whether the ionization occurs on the <u>in</u>coming or <u>out</u>going part of the $V_0(r)$ trajectory. These are

$$\begin{aligned} \chi_{in}(b,E,E') &= \chi_+(b',E') - \Delta\chi_+(b',E') + \Delta\chi_0(b,E) \\ \chi_{out}(b,E,E') &= \chi_0(b,E) - \Delta\chi_0(b,E) + \Delta\chi_+(b',E') \end{aligned} \tag{33}$$

with

$$\begin{aligned} \chi_0(b,E) &= \pi - 2b \int_{r_0}^{\infty} \frac{dr}{r^2[1-V_0(r)/E-b^2/r^2]^{1/2}} \\ \Delta\chi_0(b,E) &= -b \int_{r_i}^{\infty} \frac{dr}{r^2[1-V_0(r)/E-b^2/r^2]^{1/2}} \end{aligned} \tag{34}$$

where E' is the recoil energy of the products and r_0 is the turning point on V_0. χ_1 and $\Delta\chi_1$ are given by expressions identical to Eqs. (34) with $b \to b'$, $E \to E'$, $r_0 \to r_+$ and $V_0 \to V_+$. Conservation of orbital angular momentum requires $b' = b(E/E')^{1/2}$. A vertical (Franck principle) transition from V_0 to V_+ is assumed, wherein the local kinetic energy of the nuclei at $r = r_i$ is conserved. This determines E' through

$$E' = E - V_0(r_i) + V_+(r_i) \tag{35}$$

with the potentials both referred to zero energy at $r = \infty$. The energy of the ionized electron is then

$$\begin{aligned}\varepsilon &= E - E' + \varepsilon_0 \\ &= \varepsilon_0 + V_0(r_i) - V_+(r_i)\end{aligned} \tag{36}$$

with ε_0 the ionization exoergicity at $r = \infty$, given by the difference between the excitation energy of A^* and the ionization potential of B, and the second equality obtained from Eq. (35). The impact parameter b must be small enough to make $r_i > \max\,(r_0, r_+)$. The classical differential cross section is then

$$\sigma_K(\theta,E,E') = \sum_{j=\mathrm{in,out}} \sum_{\nu} \frac{P_j(b_\nu, E, r_i)b_\nu}{|\sin\chi_j\,\partial\chi_j/\partial b_\nu|};\ |\chi_j(b_\nu)|_{\mathrm{mod}\,\pi} = \theta. \tag{37}$$

The sum over ν is analogous to the sum over i in Eq. (1); the values of b contributing will depend on j. $P_j(b,E,r_i)$ is the probability of ionization at r_i, given by

$$\begin{aligned}P_{\mathrm{in}}(b,E,r_i) &= \frac{\Gamma(r_i)}{\hbar v_b(r_i)}\ \exp\,[-2\Delta\xi(b,E)] \\ P_{\mathrm{out}}(b,E,r_i) &= \frac{\Gamma(r_i)}{\hbar v_b(r_i)}\ \exp\,[-4\xi(b,E) + 2\Delta\xi(b,E)]\end{aligned} \tag{38}$$

where

$$\begin{aligned}\Delta\xi(b,E) &= \frac{1}{2}\int_{r_i}^{\infty} \frac{\Gamma(r)dr}{\hbar v_b(r)} \\ \xi(b,E) &= \frac{1}{2}\int_{r_0}^{\infty} \frac{\Gamma(r)dr}{\hbar v_b(r)}\end{aligned} \tag{39}$$

and

$$v_b(r) = v\ [1 - V_0(r)/E - b^2/r^2]^{1/2}. \tag{40}$$

$\xi(b,E)$ may be identified as the classical limit expression for the imaginary part of the phase shift, Eq. (15), and $v_b(r)$ is the local velocity. The total reaction cross section is

$$\sigma_R(E) = 2\pi \int_0^\infty b\,db \int_{r_0}^\infty dr_i [P_{in} + P_{out}] , \qquad (41)$$

which reduces to the optical model expression, Eq. (21), upon integrating over r_i analytically.

Miller[24] gives the quantum mechanical S-matrix as

$$S_\ell(E,E') = -2i(2\mu/\hbar^2)^{1/2} (EE')^{-1/4} \exp[i(\eta_\ell + \eta_\ell^+)] \qquad (42)$$

$$\times \int_0^\infty dr [G_\ell(r)]^* \mathcal{V}(E'-E;r) G_\ell^+(r)$$

where η_ℓ and η_ℓ^+ are phase shifts in $V_0(r) - \frac{i}{2}\Gamma(r)$ at E and $V_+(r)$ at E' respectively, and G_ℓ and G_ℓ^+ are the corresponding radial wavefunctions, normalized to unit amplitude sine functions asymptotically. $\mathcal{V}(E'-E;r)$ is an electronic discrete-continuum matrix element given by

$$\mathcal{V}(E'-E;r) = \langle\phi_\varepsilon|H-E|\phi_0\rangle \qquad (43)$$

as in Eq. (22), with ε, the energy of the ionized electron, given by $\varepsilon = \varepsilon_0 - E' + E$. It is noted that

$$\Gamma(r) = 2\pi\rho|\mathcal{V}(E'-E;r)|^2; \quad E'-E = V_0(r)-V_+(r) \qquad (44)$$

by comparing Eqs. (43) and (22). The scattering amplitude for the heavy particles is then

$$f_R(\theta,E,E') = (2ik)^{-1} \sum_\ell (2\ell+1)\, S_\ell(E,E')\, P_\ell(\cos\theta) \qquad (45)$$

Miller shows[24] that stationary phase evaluation of the integral in Eq. (42)

using WKB wavefunctions leads to a semiclassical theory, in which the classical Franck condition (Eq. (35)) holds and $S_\ell(E,E')$ is given in the classical limit by

$$S_\ell(E,E') = \sum_i \left[\frac{P_{in}(\ell,E,r_i)}{\frac{d}{dr}[V_o(r)-V_+(r)]_{r=r_i}}\right]^{1/2} e^{i\phi_{in}(r_i)} \tag{46}$$

$$+ \left[\frac{P_{out}(\ell,E,r_i)}{\frac{d}{dr}[V_0(r)-V_+(r)]_{r=r_i}}\right]^{1/2} e^{i\phi_{out}(r_i)}$$

where the sum is over r_i satisfying Eq. (35), the P's are given in Eq. (38), and the phases are

$$\phi_{in}(r_i) = 2\eta_\ell^+ - \Delta\eta_\ell^+ + \Delta\eta_\ell^0, \tag{47}$$

$$\phi_{out}(r_i) = 2\eta_\ell^0 - \Delta\eta_\ell^0 + \Delta\eta_\ell^+ ,$$

with η_ℓ^0, η_ℓ^+ JWKB phase shifts in $V_0(r)$ at E and $V_+(r)$ at E' as in Eq. (7), and

$$\Delta\eta_\ell^0 = k\int_{r_i}^{\infty} [1-V_0(r)/E - (\ell + \tfrac{1}{2})^2/k^2r^2]^{1/2}dr \tag{48}$$

with transcriptions for $\Delta\eta_\ell^+$ as above for χ, with $k\to k'$. Thus in the classical limit a real trajectory is specified on V_0 and V_+ by imposing the classical Franck condition. The probability moduli in Eq. (46) will possess singularities at extrema in the potential difference as well as when $r_i = r_0$. These can only be removed by redoing the stationary phase integration in a "uniform" manner. Hickman and Morgner[30] have used a model which removes these singularities while still employing a local $\Gamma(r)$. They approximate the $\mathcal{V}$ matrix by

$$\mathcal{V}(E'-E;r) \simeq \left(\frac{\Gamma(r)}{2\pi\rho}\right)^{1/2} , \tag{49}$$

while performing the radial integral in Eq. (42) numerically. This essentially replaces the classical Franck (stationary phase) approximation by a Franck-Condon-like approximation, and treats all the singularities and interferences uniformly. The theory was used to calculate the Penning ionization angular distribution for $He^*(2^3S)$ + Ar (see Section III.D.1.b).

II.D.2. Excitation transfer differential cross sections

Just as calculation of the Penning ion angular distributions requires V_0, V_+ and Γ, the angular distribution of products of electronic energy transfer in a two-state approximation demands V_0 and V_1, where V_1 is the product potential, along with the transition probability, contained in the off-diagonal coupling V_{01}. It is usually convenient (see above) to work in the diabatic representation, and we will assume that V_0 and V_1 are diabatic potentials which may cross at some real value of r. The classical formulation [Eqs. (33), (34) and (36)] ensues nearly exactly as given above if one specifies a transition radius r_t in place of the ionization radius r_i. In this case the product kinetic energy E' is determined by asymptotic energies only:

$$E' = E + \varepsilon(A^*) - \varepsilon(B^*) \tag{50}$$

where the ε's are bound-state electronic energies, taken relative to the ground state of each atom or molecule. Thus the classical Franck condition (35) holds only if the transition occurs at a crossing point, r_x, of V_0 and V_1. For $r_t = r_x$, evaluation of the transition probabilities appearing in Eq. (36) can be done using the LZS theory (which employs classical trajectories). The total transfer cross section in the LZS approximation may be evaluated as a one-dimensional quadrature if straight-line trajectories are used.[55]

Quantally this problem is in the usual close-coupled equations category. For analysis of product angular distributions it seems reasonable that a two-state analysis might suffice, provided that the different product channels are not strongly coupled themselves, and the absorption into channels other than the one considered is weak.

III. Experimental differential cross section measurements and interpretation

III.A. Special techniques for excited state scattering studies

Scattering studies with metastable atoms are in many cases easier (and less expensive) than experiments with ground state atoms. The discussion below will be mainly concerned with helium, as most of the information is available for this atom. Fig. 2 show a skeletal setup of the experiment. A helium beam from a supersonic nozzle source is excited by electron impact to its two metastable states. The singlet state can be quenched by the 2μ-radiation from a He-gas discharge lamp:

$$\begin{aligned} \mathrm{He}(2^1S) + h\nu(2\mu) \rightarrow \mathrm{He}(2^1P) &\rightarrow \mathrm{He}(1^1S) + h\nu(584\ \mathring{A}), \\ &\rightarrow \mathrm{He}(2^1S) + h\nu(2\mu). \end{aligned}$$

The branching ratio is 1 : 1000 in favor of the ground state. The beam is scattered from a second supersonic beam and the electronically excited atoms are detected. As excitation transfer can occur during the collision (e.g., $\mathrm{He}^* + \mathrm{Ne} \rightarrow \mathrm{He} + \mathrm{Ne}^*$) a second quench lamp is sometimes installed in front of the detector, in order to be able to study the energy transfer process separately.

III.A.1. The detector

The detector used is very simple. It consists of an open multiplier or channeltron, usually operated in the pulse counting mode. The high electronic excitation of the particle causes electron emission on the first dynode or entrance cone. The probability for electron emission has been measured absolutely by Stebbings et al.[56] and by Borst.[57] It depends on the material of the detector, its gas coverage and its past history. It is universally assumed that the emission probability is independent of the kinetic energy of the excited atom. But only recently Brutschy[58] has shown that this is true for kinetic energies in the range from 17 to 86 meV, at least for He^* on a dirty (10^{-6} Torr) surface. The differential cross section for scattering of $\mathrm{He}(2^1S)$ from He was measured twice at the same center of mass energy (E = 42 meV), but under different LAB

conditions. One of the two beams was alternately cooled to liquid nitrogen temperature, the other one left at room temperature.
Fig. 3 shows the two Newton diagrams for the two runs. The velocity of the He^* impinging on a surface changes by a factor of 2.2. The largest energy (E = 86 meV) is obtained for $\theta = 45°$. Fig. 4 shows the experimental results. They differ by up to a factor of 4 at some angles, because of the Jacobian transformation factor. After converting the two differential cross sections to the center of mass system, they should be identical, save for the velocity dependence of the detection probability. Fig. 5 shows the c.m. distributions. They are identical within experimental error. This implies that the emission probability is independent of the kinetic energy in the 17 to 86 meV range. The group at Saclay (Manus, Watel and coworkers) is planning to measure the velocity dependence of the emission coefficient absolutely with a laser technique.[59]

It is generally not necessary to differentially pump the detector. An electric field perpendicular to the detector axis is used to prevent any charged particles from reaching the detector. The background count rate, with the He^* beam turned off and the quench lamp(s) burning, should not exceed 5 to 10 counts per second. The large angle fall-off of the He^* beam profile is also much better than in ground state scattering. For sufficiently collimated beams the large angle ($\theta > 30°$) beam profile is mainly determined by scattering of the He^* beam from the background gas. For a 10^{-6} Torr vacuum a value of 10^{-9} is typically attained between the intensities at $\theta = 0°$ and $\theta = 90°$. This low background is 2 to 3 orders of magnitude lower than that for the best detectors for ground-state particles, which use electron impact ionization and UHV-techniques. Because of the extreme simplicity of the detector, a stationary monitor detector can be installed easily, whose count rate can be used to compensate for shifts and fluctuations in the beams and quenchlamps, though not for gain shifts in the two detectors.

The intensity at small scattering angles is very high, which can lead to count rate dependent gain variations and a rapid deterioration of the detector. Copper-beryllium multipliers can be rejuvenated easily by heating them first with a hot air gun to 100-120°C, and then rinsing the hot multiplier in cold methanol.

III.A.2. The quench lamp

Gas discharge lamps are used to optically pump the metastable helium atoms into a higher excited electronic state, which has a dipole allowed transition to the ground state. Only $He^*(2^1S)$ can be pumped selectively, thereby producing pure $He(2^3S)$ beams. For the heavier rare gases both metastable states are equally pumped by gas discharge lamps. The use of cut-off filters to selectively pump one state is not adequate because of the temperature dependence of the filter transmission and the low f numbers of the pumping transition. Metastable Ne can be selectively pumped by a cw dye laser,[60] while Ar^*, Kr^* and Xe^* have so far only been selectively pumped by pulsed dye lasers.[61]

A detailed investigation of the 2μ output of capillary He gas discharges has shown the features collected in Table II to be optimal.[58] Four to five turns of a 3 mm inner diameter pyrex tube is wound helically around a 35 mm mandrel. The anode is a small (1 mm diameter) tungsten pin. The hollow cathode is made from aluminum 20–30 mm diameter, 50 mm high. A slow, continuous stream of gas flows from anode to cathode. The lamp has to be cooled effectively for smooth operation. The following procedure has proved to be very satisfactory. All outer parts of the lamp are coated by a thin (1-2 mm) layer of a silicone rubber[62] and put into a splittable aluminum housing. The space between the housing and the lamp is then filled with the same silicone rubber, which gives good thermal contact and electrical isolation. The lamp housing is clamped on a precision machined water cooled rod. The total length of the lamp and housing is 40 mm. For a He^* beam above a kinetic energy of about 100 meV one needs a larger lamp for adequate (> 99%) quenching power. It is more convenient to work with two short lamps instead of a longer one. For many experiments the lamps have to be switched on and off periodically. The maximal usable frequency is around 10 kHz; above this limit the pulse shape deteriorates because of the long-lived afterglow.[58]

III.A.3. Description of a scattering apparatus

Fig. 6 shows that central part of the Freiburg scattering apparatus, for which the best resolution has been obtained so far. The helium gas is expanded from a very high pressure (20-100 bar) through a small nozzle hole (12-100 μm) into the first differential pumping chamber. The temperature of the gas before the expansion can be varied between T = 80 K and 1600 K. Figure 6 shows beam sources which are used at and below 300 K. The final kinetic energy of an atomic nozzle beam is given by $E = \frac{5}{2}$ kT ($\frac{3}{2}$ kT from the random motion, 1 kT from the work gained in the expansion), so that the beam energy can be varied between 16.5 and ∿ 350 meV. The central part of the beam passes through a Campargue-type skimmer[63] into the excitation chamber. It traverses a hole in the indirectly heated cathode, which has a spherical electron emitting surface. The electrons are accelerated by a concentric grid to typically 150-200 eV kinetic energy. The two beams interact over a distance of 4 cm in the electromagnet, whose field compensates the diverging effect of the space charge of the electrons. After the excitation region the singlet metastables can be de-excited by the quench lamp. Charged particles and helium atoms in very high Rydberg states are removed from the beam by the quench condenser. The last defining slit collimates the beam to 0.4°. A second quench lamp in from of the detector is used for kinetic energies above 100 meV, when one lamp is not sufficient for an adequate (> 99%) quenching efficiency, or to quench metastable Ne atoms, which have been produced by excitation transfer (see Sec. III.D.2). A more detailed description has been given elsewhere.[64]

III.A.4. Velocity distributions

The excitation of an atomic beam by electron impact is surprisingly intricate, although little more than momentum and energy conservation is needed for a basic discussion. The kinematics of the excitation process has been discussed in detail and will not be repeated here.[64] It turns out that the narrow velocity distribution of the ground state beam is best preserved by directing the electron beam parallel or antiparallel to the gas beam. The detailed shape of the velocity distribution depends on a number of parameters: electron energy and current, compensating magnetic field, angle of divergence of the electron beam, background and gas pressure etc. In the apparatus of Fig. 6 the velocity distributions of the He^* beam can be observed during the measurement of an angular distribution by the time-of-flight (TOF) method. The beam is mechanically chopped and the TOF spectra are recorded by a fast multiscaler. Figure 7 shows some TOF distributions. The overall experimental resolution is $t = 10$ μs for a flight path of 121 cm. A detailed analysis of the surprising bimodal structure clearly visible in figure 6 for flight times greater than 0.5 ms has been given elsewhere.[64] Only the results are quoted here. The peak at smaller flight times is due to He^* atoms from the primary excitation process:

$$He + e^- \rightarrow He^* + e^- .$$

The second peak, at larger flight times, which has exactly the velocity of the unexcited helium beam, is due to a subsequent resonant energy transfer:

$$He^* + He \rightarrow He + He^* .$$

The difference in flight time between the two peaks is caused by the momentum transfer of the electron to the helium atom during the excitation process. The cross section for the resonant energy transfer process is to a first approximation proportional to the g-u splitting of the two corresponding excited-state potential curves of the He_2 molecule.[65] The van der Waals constants for the singlet state differ by 15%, while they are equal for the triplet state.[66] This leads to a larger splitting and therefore an increased rate of energy transfer and a better velocity resolution of the singlet He^* beams. The exchange peaks at longer flight times are in general larger then the direct excitation peak. This means that most He^* atoms will have experienced more than one excitation transfer collision in the beam. A simple calculation shows that >98% of the excitation transfers occur before the atoms reach the scattering center, so that the measured velocity distributions are the appropriate ones. At higher stagnation temperatures the velocity distribution from nozzle beams deteriorates. The relative momentum transfer from the electron also becomes smaller for increased He^* velocities so that the two peaks finally coalesce.

The TOF distribution for E = 540 meV has been obtained in a completely different way. The He plasma of a high current arc discharge has been expanded through a small nozzle hole, giving directly a supersonic $He(2^3S)$ beam of higher kinetic energy (see Section III. A. 6).

III.A.5. Intensities

The intensity of the He^* beam of the apparatus of Fig. 5 collimated to 0.4° FWHM is typically 10^{10} singlets/sec (or $3 \cdot 10^{14}$ atoms/sec·sr) and $1.5 \cdot 10^9$ triplets/sec for beam energies between 66 and 350 meV and about one fifth of this value at 16.5 meV (liquid-nitrogen-cooled nozzle). The triplet intensity can be increased at the expense of a poorer velocity resolution by a lower electron acceleration voltage.

There is roughly a seven orders of magnitude difference in the intensity of the ground state helium beam compared to the metastable helium beam. This large ratio may appear unfavorable but it cannot be improved easily without unfavorable effects on the velocity and angular resolution. The electron beam excites $\approx 10^{-3}$ of the ground state beam to the metastable state, a fraction which connot be increased very easily under beam conditions. But only $\approx 10^{-4}$ of the excited He^*

atoms remain in the final beam. All others have too large scattering angles and hit some collimating diaphragms and are therefore removed from the He^* beam before it can enter the collision chamber. A comparison of beam intensities for different designs has been given.[64]

III.A.6. Other He^* sources

The highest kinetic energies available from a nozzle source are limited by the melting point and tensile strength of the nozzle materials to energies below ∿ 400 meV. Beams energies above ∿ 10 eV can be obtained by charge exchange in Cs vapor.[93,94] To obtain He^* beams between these two extremes, two different gas discharge devices have been tried.

Searcy[68] operated a low current, high voltage (0.1 mA, 8 KV) discharge between a positively charged needle through a nozzle hole onto a skimmer. The He^* atom beam has an energy of 4.6 eV and an intensity of 10^{10} atoms/sr·sec. One scattering experiment has been reported using this source.[69]

Schmidt[70] has tried a low voltage, high current arc discharge (30 V, 40 A). The hot He plasma expands through a relatively large nozzle (∿ 0.1 - 0.3 mm). A sufficient number of He^* atoms, more than 98% in the triplet state, are produced directly by this plasma jet. The beam intensity is roughly a factor of 5 less intense, compared to electron impact excitation, but nearly four orders of magnitude more intense than that from Searcy's design. By varying the electrical power, gas pressure, and nozzle diameter the kinetic energy can be varied up to .8 eV for He^* and 1.6 eV for Ar^*. The beam intensity and energy is (sometimes) stable enough for several hours that angular distributions can be measured (see Figs. 18 and 30). Higher energies could not be obtained, because of the very low momentum transfer cross section between electrons and helium atoms (Ramsauer minimum) and due to cooling of the beam at the water cooled nozzle hole. Because of the large power density in the discharge region (2 - 5 kW/cm^3), efficient water cooling was necessary. A modified version of Maecker's cascade plate design[70,71] was used for confining the arc.

For ground state He beams, Knuth's group[72,73] has obtained energies up to 5 eV with a different arc source. Large nozzle holes (∿ 2 mm) and very high pumping speeds were used in the first chamber. It would be surprising if this design could not also be made to yield higher energy metastables. The larger nozzle hole might drastically reduce the cooling of the hot He plasma.

III.A.7. The influence of photons on the differential cross sections

Two cases are known where the experimental differential cross sections are strongly perturbed over a narrow angular range by uv photons. Both cases will be discussed in detail to make the identification of similar effects easier in future work.

For the scattering of He(2^3S) + He Haberland *et al.*[74] observed a very narrow spike at $\theta_{LAB} = 90°$ in the angular distribution as shown in Fig. 8 . The ratio of the intensity at $\theta = 90°$ to that at some other angle was independent of nearly every experimental parameter (beam intensity, electron current and voltage, magnet current, background and secondary beam pressure) so that it was thought that the 90°-spike was not an experimental artifact. Only after it was impossible to produce a similar spike in a theoretical computation, a second detailed investigation revealed the following cause. There are always some photons from the He resonance transition ($2^1P \rightarrow 1^1S$, E = 21.21 eV) in the beam. Because of the extremely large cross sections for resonance absorption, they can be effectively trapped in a strong beam. Some of those photons will be absorbed by helium atoms from the secondary beam in the scattering center. Most of them will decay back to the ground state, but a fraction of 10^{-3} will make a transition to the metastable 2^1S state, and these atoms will be detected on the multiplier. The shape of the 90° peak is given exactly by the convolution of angular profiles of the detector and secondary beam, as the momentum transfer by the photon is negligible in this case.

A similar peak at $\theta^{\circ}_{LAB} = 90°$ was observed by Martin _et al_.[75] and by Haberland _et al_.[76] in scattering studies of He^{*} + Ne. An interpretation similar to that for He^{*} - He was given first by the latter authors, but proved not to be correct.[75] The following two step process is presently thought to be the most likely cause.[77] An excitation transfer occurs from $He^{*}(2^{1}S)$ to $Ne^{*}(3s_2)$ in the scattering center. The $3s_2$-state has a lifetime of only $\sim 10^{-8}$ sec, so that most of the atoms will radiate when the two atoms have separated but are still in the scattering center. More than 50% of the excited Ne atoms will make a transition to the ground state. The emitted UV photon can be reabsorbed by any Ne atom nearby. The strongest absorption will occur from atoms in the intense (10^{-4} T) secondary beam. If these decay to the metastable states they are detected at $\theta_{LAB} = 90°$.

In summary any sharp peak at $\theta_{LAB} = 90°$ is very valuable for testing the resolution of the apparatus but should be regarded with suspicion.

III.B. Pure Elastic Scattering

As outlined in Section II.B, optical model analysis of elastic scattering, even in the Penning systems, may be ambiguous because of the interplay between the real and imaginary parts of the optical potential. It was therefore desirable to examine systems for which the absorption or inelasticity would be vanishingly small. While this is difficult for electronically excited atoms, evidence from static afterglow experiments[78-80] attests to fairly slow quenching of metastables in pure noble gas discharges (although very rapid resonant energy exchange). For Ne through Xe, quenching by the bath gas occurs mainly by intermultiplet mixing,[2,3] e.g.,

$$\mathrm{Ne}^*(^3P_{2,0}) + \mathrm{Ne} \rightarrow \mathrm{Ne}^*(^3P_1, {}^1P_1) + \mathrm{Ne} \rightarrow \mathrm{Ne} + \mathrm{Ne} + h\nu,$$

and the measured rates correspond to thermal cross sections of $\sim 5 \times 10^{-3}$ Å^2 or less. If the ground state noble gas partner is lighter, e.g. $\mathrm{Ne}^*(^3P_{2,0})$ + He, intermultiplet mixing is the only possible inelastic process at thermal energy. Such systems are therefore likely to behave nearly elastically, and one can safely use a real two-body potential to analyze the angular distributions.

Experimentally it is not feasible to detect the scattered ground state atom because of the enormous background of ground state atoms in the excited beam (see Section III.A). Although detection of the heavier scattered atom is kinematically unfavorable because its recoil velocity is smaller than the velocity of the center-of-mass, analysis of differential scattering can still be carried out, since the c.m. → LAB transformation is unambiguous. In addition, it becomes possible to observe backward scattering in the normal range of LAB angles. In the fitting procedure, a parametric potential function is assumed, a center-of-mass angular distribution calculated (usually by numerical integration of Eq. (5)) and transformed to the LAB system with appropriate resolution averaging for comparison with experiment. Parameter values are adjusted by the Marquardt nonlinear least squares method[81] to give a best fit.

Fig. 9 shows scattering data for Ne^* + He and Ar^* + He[82] from the Pittsburgh laboratory. The wide-angle maxima are kinematic artifacts ("Jacobian rainbows") owing to the infinite density of c.m. scattering angles contributing at the edge of the recoil velocity shell for the heavier atom. If the beams were monochromatic and angular resolution perfect, no scattering would be observed outside the Jacobian rainbow angle. The observed scattering intensity thus drops off rapidly, and is a measure mainly of the velocity resolution. The calculated curves are fits from assumed potential functions. The absence of interference features attests to the repulsive character of the interactions as well as to the lack of significant splitting of the potential curves for different Ω. A sufficiently fine-grained oscillatory pattern would not be resolved, however. Because the Jacobian rainbows are very sensitive to apparatus resolution, their angular region was excluded in the fitting procedure.

Potential functions used[82] were an exp-6 function with two free repulsive parameters, and a modified exp-6 with three repulsive parameters. The modification was introduced as a screened ion-induced-dipole attraction, which softens the repulsion at small r. The fitted potentials are shown in Fig. 10. The dashed curves in Fig. 9 show the fits obtained with the simple exponential repulsion and the solid curves with the modified repulsion. The bend in the potentials at r ≃ 3 Å is clearly required for a good fit to the higher energy. The part of the repulsion probed at each energy is indicated in Fig. 10. Fitting of He^* scattering has also required modification of the low-energy repulsion (see below). Further experimental work on these and other systems of the heavy metastable-light atom variety is in progress.

III.C. Symmetric Noble Gas Systems

III.C.1. Symmetry properties of potentials and scattering amplitudes

We begin by specializing the discussion of Section II.C to the He^*-He case. If a metastable helium atom collides with a ground state helium atom, one has the interaction of two identical atoms in different electronic states. This simple fact has a strong influence on the scattering patterns.

Asymptotically one prepares one beam to carry electronically excited atoms (A) and the other ground state atoms (B), and consequently the wavefunction can be written as

$$\phi_1(A) \cdot \phi_0(B)$$

where $\phi_1(A)$ means that atom A is in the excited state and $\phi_0(B)$ that B is in the ground state. As the Hamiltonian is invariant with respect to interchange of atom A and B

$$\phi_1(B) \cdot \phi_0(A)$$

is also a possible wavefunction. A linear conbination will then give the correct asymptotic eigenfunction

$$\chi^{g,u}(r\to\infty) \sim \phi_1(A)\ \phi_0(B) \pm \phi_1(B)\ \phi_0(A)$$

where g (gerade) corresponds to the plus sign and u (ungerade) to the minus sign. The asymptotically prepared state is not an eigenstate of the Hamiltonian when the atoms are close together, leading to a rapid exchange of the excitation energy between the two atoms. The electronic wavefunctions χ^u and χ^g are orthogonal for all internuclear distances r; in addition, all coupling terms vanish for identical isotopes. Within the Born-Oppenheimer approximation the total interaction is averaged over the electronic wavefunctions for fixed r. As one averages over different electronic wavefunctions one obtains different interaction potentials V_g and V_u. These are shown for the lowest electronic states of He_2 in Fig. 11, and are discussed below. Within the Born-Oppenheimer approximation the potential does not depend on the mass of the heavy particles; the potentials for ^{4}He^{4}He, ^{4}He^{3}He, and ^{3}He^{3}He are therefore identical.

The scattering amplitudes on the other hand depend strongly on the combination of isotopes. The total scattering amplitude for distinguishable particles, e.g. ^{4}He + ^{3}He becomes

$$f(\theta) = \frac{1}{2}\,[f_g(\theta) + f_u(\theta)];$$

for indistinguishable particles this has to be symmetrized appropriately. The ^{4}He nucleus is a boson, and therefore the total wavefunction does not change sign when interchanging the nuclei. One obtains for the properly symmetrized scattering amplitude

$$f(\theta) = \frac{1}{2}[f_g(\theta) + f_g(\pi-\theta) + f_u(\theta) - f_u(\pi-\theta)]$$

The amplitude f_u is antisymmetric with respect to interchange of the nuclei, which is a direct reflection of the symmetry property of the corresponding electronic wave function. This implies that the cross section need not be symmetric about $\theta_{cm} = 90°$. One can define a scattering amplitude $f_d(\theta)$ for direct scattering

$$f_d(\theta) = \frac{1}{2}[f_g(\theta) + f_u(\theta)],$$

and for exchange scattering,

$$f_{ex}(\theta) = \frac{1}{2}[f_g(\pi-\theta) - f_u(\pi-\theta)].$$

The total scattering amplitude becomes

$$f(\theta) = f_d(\theta) + f_{ex}(\theta).$$

The corresponding scattering process can be visualized as shown in Fig. 11. The direct and exchanged excited particles come from different beams. But the detector in principle cannot distinguish between them; thus, the amplitudes add coherently. If the overlap between direct and exchange amplitudes is small, the exchange contribution can be isolated.[65] For noble gas exchange scattering at thermal energies, however, the overlap is substantial. (But see Section III.C.5 below).

Other exchange processes may be described similarly, e.g., spin exchange, charge exchange, or at much higher kinetic energies neutron- or π^--exchange.[83]

III.C.2. General features of the noble gas excimer states

The potential energy curves of the noble gas diatomic molecules are rather unusual.[65,84,85] The ground state of the He_2 molecule is purely repulsive save for a weak van der Waals minimum (well depth $\sim$ 1 meV), which might not support a bound state. The next four excited states correlate asymptotically with $He(2^1S)$ and $He(2^3S)$, respectively. As can be seen from Fig. 11 these states have deep chemical wells at ~ 1 Å and intermediate maxima at 2 - 3 Å.

The He_2 A $^1\Sigma_u^+$ state has nearly the same dissociation energy as the He_2^+ $(^2\Sigma_u)$ ion. This supports the idea that the excited He_2 configurations can be described at small interatomic distances as an inner He_2^+ core with an outer Rydberg orbital. This description is less quantitative for the heavier rare gas pairs. The unusual maxima result either from curve crossing, e.g. C $^1\Sigma_g^+$, or as for the A $^1\Sigma_u^+$ state by a changeover in the dominant exchange energy. At large r the electron clouds overlap only weakly, and one has the usual repulsion from the Pauli principle. At smaller r the attractive He_2^+ ionic core is formed. An extensive discussion of the He_2 potentials has been given by Guberman and Goddard.[84]

Transitions from the $A^1\Sigma_u^+$ potential become optically allowed for small internuclear distances and give rise to the well known Hopfield continuum and the 600 Å emission and absorption bands.[86] From the analysis of the optical spectrum, the inner attractive parts of the potentials have been determined quite accurately. Information on the long range parts, however, has been only semi-quantitative at best.

For the heavier noble gases the core multiplicity of the metastable states gives rise to eight potential curves (six for $^3P_2$, two for $^2P_0$). The Ne_2 potentials have been calculated by Schneider and Cohen,[87] who have also performed scattering calculations for this system. For Ar_2 theoretical and experimental data exist,[88] whereas for Kr_2 and Xe_2

only qualitative estimates of the potentials are available. These excited states play a prominent role in the rare gas excimer lasers.[89,90]

III.C.3. Experimental results and potentials

Figs. 13, 16, 18 and 19 show the experimental results for He^*-He scattering in the LAB system. The intensity in arbitrary units is plotted against the LAB scattering angle. For two particles of equal mass - as is the case here - the c.m. scattering angle is obtained by multiplying the LAB angle by a factor of two. For the thermal energy results the potential parameters were determined by trial and error. Piecewise analytical functions, coupled by Spline interpolation polynomials, were used to represent the shape of the potential. The phase shifts were calculated numerically by the Numerov procedure. The calculated cross section was then transformed into the LAB system and averaged over experimental resolution. The broadening of the data due to the limited velocity resolution was taken into account by increasing the breadth of the angular resolution appropriately, so as to conserve computer time. The free potential parameters are determined by the Marquardt non-linear least squares routine.[81] The analytical form of the potential is rather complicated, but not too much effort was made to keep the number of free parameters small, because of the complicated shapes of the potentials. Due to the extensive interference patterns the potential parameters had to be close to their final values to allow convergence of the Marquardt routine. A rather large amount of manual adjustment of the potential parameters was therefore necessary.

III.C.3.a. $He^*(2^1S)$ + He

The angular distributions for $He^*(2^1S)$ + He are shown in Fig. 13 for six different kinetic energies. That part of the potential which can be derived from the data is given in Fig. 14. (Note the change in energy scale above -50 meV.) The horizontal arrows give the collision energies used in the experiments. The potential is given in Table III (energies are in electron volts and distances in Angstroms). A Morse type potential V_1 has been obtained by Sando[86] for the inner part ($r \leq 1.7$ Å) of the A $^1\Sigma_u^+$ potential from the analysis of optical data. He also gives some numerical values for larger r, which were fitted by subtracting a sine function from $V_1(r)$, giving $V_2(r)$. The small r side of the potential maximum was represented by a parabola (V_4) which was smoothly joined at both ends by cubic spline interpolation (V_3,V_5). The long range part was found to be well represented by a modified exponential function (V_6). The long range part of the $C^1\Sigma_g^+$ curve could also be represented by a modified exponential (V_g). Only the parameters of V_4, V_6 and V_g were varied by the Marquardt routine. V_1 and V_2 have been determined by Sando, and V_3, V_4 are spline interpolations.

The potential minima of the van der Waals attraction[58,91] are at $r \geq 6$ Å, where they have only a negligible influence on the differential cross section. They were therefore neglected in the calculation. At $r = 6$ Å the well depth would be smaller than 1 meV. The 15% difference in the van der Waals constants for the two potentials thus affects the differential cross sections only indirectly.[109] But this difference has a significant influence on the form of the velocity distribution of the He^* beam,[64] where the relative kinetic energies are much lower (10^{-2} to 10^{-5} eV). The fit to the data is quite good, especially at lower energies, but could still be improved.

For one particular energy a much better fit could usually be obtained, but then the fits at the other energies deteriorate rapidly. The χ^2-values for the fits are 8.4, 13.6, 108, 63, 57, 131 from the lowest to the highest energy. These values are relatively large because of the very small error bars of the experimental results. A more flexible potential and proper treatment of the velocity averaging could probably yield much smaller χ^2-values.

Buckingham and Dalgarno[92] were the first to calculate the interaction bewteen $He^*(2^1S)$ and He. Recently Guberman and Goddard[84] performed a generalized valence bond (GVB) calculation for many excited He_2 states. Their results are given by the dashed lines in Fig. 13. The calculated barrier height is 60.7 meV at 3.09 Å compared to $47 \pm^{2}_{1}$ meV at 3.14 ± 0.05 Å from the analysis of the differential cross section. A GVB calculation always gives an upper limit to the exact result[84], and in fact the theoretical results are 5 to 20 meV higher everywhere.

Fig. 15 shows the difference between the experimental and calculated potentials. Because the splitting is very small for $R > 3$ Å, this difference is nearly independent of the g-u symmetry, reflecting mainly differences in the mean potential. Guberman and Goddard propose a 10 to 20% reduction of their results, to account for the neglected part of the correlation energy, but this reduction is sufficient only between 3.2 and 4.0 Å. Assuming the accuracy of the potentials derived from differential scattering, Fig. 15 represents, for large r, the remaining correlation energy.

Electronic transitions are optically forbidden only for large internuclear distances r. For finite r dipole transitions to the $X\ {}^1\Sigma_g^+$ ground state are possible. They give rise to the well-known Hopfield continuum and 600 Å emission and absorption bands.[86] Only those collision partners which surmount the barrier of the ungerade potential are likely to radiate. The cross section for light emission[65] is typically 10^{-4} Å^2, which is much too small to have a noticeable influence on the differential cross sections and was therefore neglected.

III.C.3.b. $He(2^3S) + He$

The thermal energy results are shown in Fig. 16. The data are noisier as the triplet intensity is a factor 5 to 7 smaller than the singlet intensity. The overall structure of the data is similar to that for singlet scattering. The solid line gives again the differential cross-section from the potential shown in Table IV and Fig. 17. The maximum in the interaction potential is at a smaller distance and roughly 10 meV higher than in the singlet case.

The potential maximum could not be fitted by a parabola as in the singlet case; a r^4 functional dependence was found to be more adequate. The deep chemical well at 1.045 Å was represented by a Morse function, which reproduced Ginter's spectroscopic results.[160]

The long range part of the potential has been calculated by Das[161] in a multiconfiguration S.C.F. computation. He obtains a van der Waals minimum at ∿ 7 Å with a well depth of 0.16 meV, which is consistent with out results. The dotted lines have been determined by Hickman and Lane[162] from thermal diffusion and exchange measurements. The agreement is satisfactory below 40 meV. The data they analyzed were limited to this energy range. Earlier attempts to obtain the triplet potentials from bulb experiments have been reviewed by Fugol.[163]

Fig. 18 shows differential cross sections measured using the He plasma jet described in Section III.A.6. It is surprising that so much structure is still resolved, although the velocity resolution of the beam is only 30%. No fit has so far been attempted for these data.

$He(2^3S)$ atoms can also be produced by the charge exchange of He^+ ions in Cs-vapor.[93] This technique has been used extensively by the Stanford Research Institute group to measure differential cross sections at higher energies (5 to 10 eV). Some of the data[94] in reduced units are shown in Fig. 19. The kinetic energy is high enough that endoergic inelastic processes substantially affect the scattering. Analysis of these data requires a multichannel treatment.

III.C.4. The heavier noble gas symmetric systems

Ne^* + Ne, Ar^* + Ar, and Kr^* + Kr scattering has been measured by different groups at thermal energies, but no data and potentials have been published so far, as the analysis is quite involved. First, it is impossible to quench one of the two metastable states without an expensive laser, so that one is generally forced to work with mixtures; and second, 6 potentials contribute coherently for the dominant $^3P_2$ species. The cross sections for fine structure changing collisions are small[78-80] and can therefore be neglected. At higher kinetic energies the Ne^* + Ne and Ar^* + Ar scattering has been studied by the SRI group.[93]

III.C.5. Total Cross Sections

The total cross sections calculated from the potentials in Table III and IV are shown in Fig. 20 and 21. The solid line is for identical particles, while the dotted line has been calculated assuming distinguishable particles. For $He(2^3S)$ + He the experimental data of Trujillo[95] are included in Fig. 21. The total cross section for $He^*(2^1S)$ is roughly 40 $\mathring{A}^2$ larger than that for $He^*(2^3S)$. For energies below the barrier heights the cross sections for distinguishable particles can be well approximated by

$$Q = A \cdot v^{-B} \; [\mathring{A}^2],$$

with A = 503, B = 0.14 for $He^*(2^1S)$ and A = 529, B = 0.18 for $He^*(2^3S)$, and v in m s^{-1}. The oscillations below ∿ 50 meV must be symmetry oscillations as they vanish for distinguishable particles. They result from the interference of collisions with large impact parameters, which are nearly forward scattered ($\theta \approx 0$), with energy transfer collisions at small impact parameters and $\theta \approx \pi$. The relative difference between the two cross sections is given by the curve I (arbitrary scale). The position of the different maxima is nearly entirely given by the energy dependence of the S-wave phase shift, as discussed elsewhere.[58]

The sharp structures above 50 meV are due to orbiting resonances from the deep attractive well of V_u. All particles can tunnel through the maximum in V_u. The amplitude for finding a particle inside the maximum will be resonantly enhanced if the kinetic energy matches the energy of a quasibound state of V_u. For energies much below the barrier height, the tunneling probability and therefore also the width of the resonance will be small, and could therefore only accidentally be detected with the grid used in calculating the curves for the total cross section. If the kinetic energy is only a bit smaller than the barrier height, the width of the resonance will become larger. These orbiting or shape resonances play a large role in the calculation of the 600 Å band emitted by $He(2^1S)$ particles crossing the barrier. This spectrum and the resonances have been calculated by Sando[86] using his potential (V_1 of Table III). The resonances can be classified according to their vibrational (v) and rotational (J) quantum number, which can be deduced from inspection of the calculated wave functions.

III.C.6. Excitation transfer cross section

In principle there is no way to measure the exchange process directly for ${}^4He^* + {}^4He$ scattering, as the particles are indistinguishable. But the cross section for metastability exchange can of course be calculated from the determined potentials assuming distinguishable particles.[65] The expression for the total excitation transfer cross section is

$$\sigma_{trans} = \frac{\pi}{k^2} \sum_{\ell=0}^{\infty} (2\ell + 1)\sin^2(\eta_\ell^g - \eta_\ell^u)$$

where $\eta_\ell^{g,u}$ are the ℓ-th phaseshift calculated from $V_{g,u}$. The transfer cross section is mainly determined by the difference potential. The calculated excitation transfer cross section for ${}^3He(2^3S) + {}^3He$ is shown in Fig. 22 as a function of the kinetic energy. Because of the increasing splitting of the two potentials for smaller r, the cross section rises with kinetic energy. It starts to oscillate when the energy becomes larger than the barrier in the ungerade potential. The rate of excitation transfer [σ_{trans} · relative velocity, averaged over a Maxwellian distribution] is compared to experimental results in Fig. 23. These rates have been measured in two remarkable optical pumping experiments in ${}^3He$.[96,97]

The ${}^3He$ nucleus has spin 1/2, so that the hyperfine state can be different before and after a collision. This leads to a loss of coherence and a broader linewidth in the optical pumping experiments. The linewidth is measured as a function of temperature and the rate of excitation transfer is obtained after an involved analysis.[97,98] The agreement with the higher temperature data of Colegrove _et al_.[96] is very good if the correction factor of $\frac{9}{4}$ is applied to their data, as shown by Dupont-Roc _et al_.[98] The agreement is not as good with the lower temperature results of Rosner and Pipkin shown in the insert. This may be due to the neglect of the van der Waals attraction, which has a negligible influence on the differential cross sections.

III.C.7. Discussion of the interference structure

The interference structure in the differential cross sections is quite complicated, first because two potentials of unusual shape contribute coherently, and second because of the identical nuclei. The effect of the latter is easily studied by calculating the differential cross section assuming distinguishable particles. This is shown in Fig. 24 for $He(2^1S)$ + He using for the total scattering amplitude $f(\theta) = \frac{1}{2}[f_g(\theta) + f_u(\theta)]$ as discussed above. The regular oscillations at lower energies are completely absent; they must therefore be due to nuclear symmetry. For the higher energies the peak at 90° is much smaller but still present, and the intensity at large angles is markedly decreased, because of the loss of the exchange contribution. This is indicated by the hatched area of the 139 meV curve in Fig. 24. At low kinetic energies, only the long range part of the potentials is probed, where the splitting of the potentials is rather small, i.e., $V_g \stackrel{\sim}{\sim} V_u$. Therefore the scattering amplitudes will also be similar, $f_g \stackrel{\sim}{\sim} f_u$. Inserting this into the properly symmetrized scattering amplitude for identical particles, one obtains the result that the symmetrized and unsymmetrized scattering amplitudes are identical for $V_g = V_u$. As this is a very good approximation for $He(2^1S)$ + He at large r, the symmetry oscillations are washed out at the two lowest energies (see also Fig. 24).

The discussion of interferences in ground state atom-atom scattering relies heavily on the classical deflection function, which can be calculated from Eq. (4) if the potential is known. For He^*-He scattering one has phase shifts calculated quantally only for integer ℓ. It has proved very convenient to define a "quantal deflection function"[99] by analogy with semiclassical equivalence as

$$\chi(\ell + \frac{1}{2}) = 2(\eta_{\ell+1} - \eta_\ell)$$

The phase shifts are calculated only modulo 2π, but the variation from one ℓ to the next is rarely larger than 2π, so that deflection functions are easily constructed. Fig. 25 shows the (quantal) deflection function for the 42 meV measurement. It shows the behavior expected for the scattering from a purely repulsive wall. The classical deflection function would give $\chi(\ell = 0) = \pi$ and it is surprising how closely this value is attained. Fig. 26 shows the deflection functions for the higher kinetic energies. For the gerade potentials one still gets the same monotonic behavior as at lower energies, but dramatic differences can be seen for the deflection functions for the ungerade potential χ^u. The very sharp minima result from orbiting in the deep inner well, while the structure on the rainbow maxima is due to orbiting resonances (see above). The classical differential cross section can be calculated from the deflection function using Eq. (1). If $\sin\theta$ vanishes ($\chi = -n\pi$, $n = 0,1,2...$) one has glory scattering; if $\partial\chi/\partial b$ is zero, rainbow scattering occurs. The rainbow peaks are very small in this case. They are indicated by vertical arrows in Fig. 27, which compares the differential cross section calculated from the ungerade potential only $[f(\theta) = f_u(\theta)]$ with the experimental result.

The other oscillations can be understood with the help of Fig. 28, which shows schematically a typical deflection function including the effect of nuclear symmetry. The dashed lines correspond to the exchange contributions. The large angle oscillations of Fig. 15 result from interference of ℓ_1 with ℓ_3, the g–u oscillation from interference of ℓ_1, ℓ_3 with ℓ_2. This qualitative discussion can be made quantitative, as shown elsewhere.[58] The wavelengths of the oscillations $[\Delta\Theta = 2\pi/|\ell_i \pm \ell_j|]$ read off from the deflection function agree with a remarkable precision with the experimental results.

III.D. Asymmetric Noble Gas Systems

III.D.1. Scattering in Penning Systems

III.D.1.a. Elastic Scattering

As outlined in Section III.A, recent advances in experimental technique have made possible a new series of measurements on the He^* Penning systems with sufficient resolution to expose quantum interference structure at small angles in the differential cross section. This allows a much better determination of the long-range part of the potential, where $\Gamma(r)$ is small and the scattering is determined by $V_0(r)$ only. These experiments have been carried on mainly in Freiburg by Haberland and collaborators[100-104] with the Penning target species Ar, Kr, D_2, N_2 and CO over a wide energy range. With one exception, earlier published measurements by Grosser and Haberland,[105] by Lee _et al._[106,39,33] and by Winicur and Fraites[40] on He^* Penning scattering showed at most hints of the elusive undulatory structure. Somewhat better resolved structure was reported by Bentley, Fraites and Winicur[107] on $He^* + Kr$, but $He^*(2^1S)$ and $He^*(2^3S)$ were not separated by optical quenching, and the measurements were restricted to small scattering angles. Jordan, Martin and Siska[108,109] have recently reported $He^*(2^1S)$ + Ar, Kr and Xe scattering data of comparable resolution to those of Haberland _et al._ $Ne^*(^3P_{2,0})$ also Penning ionizes the heavier noble gases and all known molecules; at present there is only a limited amount of scattering data available[40,109,110] which will be reviewed later in this section. Much of the work to be presented in this section is only recently published, in press or in preparation, making this description as much a progress report as a review.

The well-studied systems $He^*(2^1S, 2^3S)$ + Ar comprise a natural and interesting prototype for excited-state intermolecular forces and

Penning ionization; in several ways these systems are unique, however, as will be seen. One is struck at the outset by the experimental observation of quite different angular distributions for singlet and triplet; this is illustrated in Fig. 29[100-102] for a collision energy of 66 meV. The singlet scattering shows a pronounced maximum at θ_{LAB} = 30°, while the triplet curve is monotonic with only subtle changes in slope. The quantum structure at small angles is also much better resolved for the singlet, while the wide angle intensity is much lower relative to small angles than for triplet. The 30° maximum in $He^*(2^1S)$ + Ar, which shifts with collision energy in much the same way as a rainbow maximum, as shown in Fig. 30,[101,102] has been the subject of some interesting qualitative speculation and quantitative interpretation. First observed as a shoulder by Lee and coworkers,[39] it was analyzed as a quantum reflection from a steeply rising opacity function. Later, Bentley _et al._[107] speculated that the hump might be electronically excited Ar formed by direct excitation transfer from He^*. More recently, Haberland and Schmidt[102] have presented a complete optical analysis of their singlet data in which they interpreted the hump, now a well resolved maximum, as a rainbow arising from a local maximum embedded in the low-energy repulsion of the real part of the optical potential. Fig. 30 shows their experimental results, over a range of energy, and the fit they obtained. The existence of a barrier in the singlet potential had earlier been postulated[111,112] on the basis of Penning ion angular distribution data (see Section III.D.1.b). Jordan _et al._[108] have demonstrated by time-of-flight measurements that the hump is almost certainly purely elastic, ruling out excitation transfer as a possibility. They also showed that the rainbow maximum in the cross section can be reproduced by a real part of the optical potential having a _slope_ maximum in the repulsive part, without an actual barrier. Fig. 31 shows the data and fit obtained at Pittsburgh.[109] The real parts of the potentials of Haberland and Schmidt[102] and of Jordan et al.[108,109] are compared in Fig. 32. Since the data from the two groups compare very well at 21 and 66(63) meV, the potentials are obtained on the same basis. The optimum potential has not yet been chosen; this may require further refinements, and perhaps further experiments. The results for large r are in excellent agreement, while those at small r, at and inside the repulsive structure, disagree mainly because of the different $\Gamma(r)$ functions used (see below). One may fairly conclude that the potential is not well-determined at small r in detail, though its gross features, e.g., the repulsive structure, are nearly beyond question.

In contrast, the lack of an intensity maximum in $He^*(2^3S) + Ar$ scattering shown in Fig. 33, again over a wide energy range,[100] augurs against such structure in the triplet potential. The fit derived by Brutschy et al.,[100] also shown in Fig. 33, produced a much smoother, though still structured potential function given in Fig. 34, with two unusual bends in the repulsive part. (These features only become apparent on a semilogarithmic plot.) The bend at lower energy, where the slope of the potential decreases markedly, is needed to describe the "flattening out" of the angular distributions at wide angles for the higher collision energies, while the high energy bend results from joining the fitted potential to the He^+-Ar ion-atom repulsion of Smith et al.[113,114] and is not determined by experiment. The unusual nature of the repulsion in both the singlet and triplet systems is discussed in Section III.D.1.d.

The widths derived are also of interest, since it has long been believed that they should be at least approximately exponential. Haberland and Schmidt[102] adopted an exponential-plus-floating gaussian form for

$He^*(2^1S)$ + Ar, obtaining a width with a shoulder (arising from the gaussian) approximately at the position of the minimum inside their barrier maximum.[115] This enhancement of the width, which enabled a good fit to the data (Fig. 30), prevented some of the interference structure which would have been caused by the barrier from appearing in the calculated cross section. Jordan _et_ _al_.[108,109] on the other hand, used a simple exponential width in deriving their potential, since the slope maximum does not produce an extensive interference pattern.[109] The $He^*(2^3S)$ + Ar scattering[100] was fit satisfactorily with an exponential Γ. The widths are compared in Fig. 35.

Current work in the Freiburg[103,104] and Pittsburgh[108,109] laboratories gives evidence that the type of repulsive structure inferred for the He^* + Ar potentials is probably a general phenomenon for noble gas partners as well as D_2. In a recent communication, Altpeter _et al_.[103] compared the He^* + Ar potentials of Brutschy _et al_.[100] and Haberland and Schmidt[102] to He^* + Kr and D_2 potentials obtained from scattering data to be published.[104] Jordan _et al_.[108,109] have also given data and potentials for $He^*(2^1S)$ + Kr and Xe. These potentials are presented in Figs. 36 and 37. While the potentials from the two groups differ in certain details, and arise from two quite different parametric potential functions, several conclusions may be drawn: (1) The van der Waals well depth ε increases monotonically as the polarizability of the ground state partner increases, while the location of the well, r_m, remains roughly constant at $\sim 6\mathring{A}$. This is expected by analogy with the well-known alkali-noble gas potentials,[116-119] though the r_m's are larger than for the alkali case, as shown in Table V. (2) The potential energy V_s at which the repulsive structure for $He^*(2^1S)$ occurs decreases monotonically as the polarizability of the ground state partner increases. (3) The position, r_s, of the repulsive structure increases for heavier partners. This point is less certain since, as usual for rainbow scattering, the experimental maxima correlate strongly with the energy of the structure in the potential, only weakly with its range. (4) At internuclear distances outside the repulsive structure, the triplet repulsive energy lies lower than the singlet, for Ar, Kr and D_2 partners,[103] as well as for He (see Section III.C).

The $He^* + D_2$ system is of particular interest, since ab initio calculations by two groups[26,120,121] have now appeared. Cohen and Lane's calculation[120] showed a substantial difference between singlet and triplet potentials, but very similar, nearly exponential widths. While both interactions were found to be only weakly anisotropic, the spherically symmetric part of the interaction showed a shallow slope maximum in the repulsion for the singlet, but smoother behavior for the triplet. These potentials are compared with experimental ones in Fig. 36. The experimental potentials were derived assuming zero anisotropy. On the other hand, Hickman, Isaacson and Miller[26,121] while also obtaining markedly different singlet and triplet interactions, found a highly anisotropic singlet potential surface, with a pronounced shoulder in the repulsion for C_{2v} geometry, and a relatively smooth curve for $C_{\infty v}$. There is generally good agreement between both theoretical potentials and the spherically symmetric experimental potential for triplet as shown in Fig. 36, but for singlet the three diverge substantially. If the large singlet anisotropy found by Isaacson et al.[121] proves to be valid, then the scattering analysis becomes much more complicated due to rotationally inelastic collisions, and the experimental potential is probably not correct. Preston and Cohen[122] have initiated classical trajectory-surface-leaking (TSL) dynamics calculations on this system, but on potential surfaces[120] with only weak anisotropy.

Predictions of total ionization cross-sections and quenching rate constants from these potentials are compared with experiment in Section III.D.1.c, and the structure in the potentials is discussed qualitatively in Section III.D.1.d.

Published work on Ne^* + Kr scattering[40] from the Notre Dame laboratory has been interpreted through the use of the potential function derived by Buck and Pauly[116] for the alkali-rare gas systems. This is a two-piece Lennard-Jones (LJ) potential, with the region $r < r_m$ described by a LJ (11,4) function, $r > r_m$ by a LJ (14,6). It was tacitly assumed that the four potential curves resulting from the various electronic angular momentum states are identical. The measurements give no evidence to the contrary. The general conclusion is that the van der Waals well depth and position are nearly identical to those of Na + Kr.[116] The data, however, did not extend to wide scattering angles (maximum angle reported was 22° LAB), and the cross section from fitted potential actually fell below the data at the widest angles, making an optical model analysis impossible. Fig. 38 shows c.m. cross sections extending to wide scattering angles, from unpublished work at Pittsburgh, for Ne^* + Ar, Kr and Xe. The absence of structure in the wide-angle intensity is in marked contrast to the $He^*(2^1S)$ case, with optical model analysis requiring recourse to other types of data, e.g., total ionization cross sections (see Section III.C.1.c). An immediate conclusion is that the van der Waals repulsion in these systems does not bear the same relation to the attraction as for the alkalis, though the difference is not as great as for He^* interactions versus those of Li.

III.D.1.b. Product angular distributions

Leu and Siska[111,112] have communicated measurements of Penning ion angular distributions for He^* + Ar, H_2, N_2, CO and O_2 at several collision energies. Unpublished work from the Pittsburgh laboratory includes He^* + CO_2, CH_4, C_2H_6, and C_2H_4, and Ne^* + Ar, with measurements on all observable fragment ions in the polyatomic systems. These experiments are performed with beam sources similar to those described in Section III.A (though with somewhat lower Mach numbers, ∿20 for each beam). The open electron multiplier detector is replaced by a quadrupole mass filter and scintillation ion counter of the type described by Lee _et al_.[123] Care was taken to eliminate stray electric fields near the collision volume; this was accomplished by enclosing the volume in a stainless steel plate-and-mesh cage whose inner surfaces were coated thinly with aquadag. After 4 cm free flight, the ions were accelerated and focussed into the quadrupole filter. A small ionizer and retarding field energy analyzer placed in front of the ion lens system allowed calibration of the mass filter and energy analysis of ionic collision products. Since the scintillation counter was an off-axis type, elastically scattered metastables and product photons were not detected, and the background was due only to the dark-counting rate of the ion counter, always less than 5 cps. Signal counting rates typically ranged from 5 to 1000 cps. Product ions with energies as low as 100 meV were successfully detected. Many of the experiments were run with the crossed beam seeded in 85-99% H_2 or He. This assured efficient collection of ions due to the resulting high centroid velocity and laboratory energy of the product ions. With unseeded beams, a likely wide spread in laboratory energy of products enhances undesirable discrimination against the lower energy ions. However, the kinematics and dynamics of the He^* systems often favor a narrow laboratory distribution, enabling reasonably low-energy measurements. A singlet quenching lamp (Section III.A) had not yet been installed for these experiments. At the 250 eV electron energy used, the He^* beam consists of ∿85% singlets, so that the measurements are representative of the singlet ionization process.

Fig. 39 shows angular distributions of Ar^+ and $HeAr^+$ for $He^*(2^1S)$ + Ar over a range of collision energies. The recoil momentum of the Penning electron may be neglected for all but the smallest heavy-particle c.m. recoil energies. The $HeAr^+$ ion is then constrained to travel with the center of mass. The measured $HeAr^+$ angular distributions agree well with calculated centroid distributions averaged over the acceptance angle (3°) of the detector; this indicates that stray fields near the collision volume or flight path do not exceed a few mV/cm. The Ar^+ ions are pitched sharply forward at each energy, the sharpness of the peaks limited mainly by the angular resolution. The narrow angular range implies recoil energies comparable to the initial energy, as expected from Penning electron spectra.[18] An approximate transformation to the c.m. system using the fixed recoil velocity approximation[124] yields $Q = E' - E$ for each energy, as given in Fig. 39. The reaction is translationally endoergic at all energies studied, with Q approximately constant at -25 ± 5 meV at the higher energies. This feature is nicely explained by the repulsive structure in the $He^*(2^1S)$ + Ar potential found from the elastic scattering (see above). For impact parameters allowing passage over the structure, the local velocity near the turning point is reduced, and the ionization probability, $\Gamma(r)/\hbar v_b(r)$, thereby enhanced. In addition, the difference function $V_0(r)-V_+(r)$ may have an extremum there, which produces a strong peak (classically infinite) in the energy distribution. If $V_+(r)$ is very weak, as expected for the Ar^+-He interaction, the peak translational endoergicity Q should be very nearly equal to the potential energy V_s at which the structure in $V_0(r)$ occurs. Reasonably close agreement between Q and V_s is evident by inspection of Fig. 32.

The derived c.m. angular distributions, shown in Fig. 40, are not quantitative owing to the approximations in the LAB→c.m. transformation, but their form is highly suggestive of rainbow scattering, non-forward peaking at lower energies shifting to forward at higher energies. This also can be plausibly attributed to the repulsive structure, following reasoning similar to that used for the elastic angular distribution. Quantitative calculations of doubly differential cross sections $\sigma_{PI}(\theta,E,E')$ using theory outlined in Section II.D.1 are currently in progress at Pittsburgh. Experiments employing ion energy analysis have been carried out for He^* + Ar at E = 154 meV which support the kinematic analysis results, but which are of insufficient resolution to allow construction of a contour map of the cross section. Time-of-flight experiments should improve this situation.

Hickman and Morgner[30] have used a quantum mechanical Franck-Condon model (see Section II.D) to calculate a c.m. angular distribution for $He^*(2^3S)$ + Ar. While the singlet and triplet systems are governed by different excited-state potentials, the calculation shows strong forward scattering, in qualitative agreement with the experiments, which pertain to $He^*(2^1S)$. The cross section is actually differential in the recoil energy E' also, so the the calculation (for which E' was averaged over) cannot be compared in a more quantitative way with experiment.

For canonical examples of diatomic molecules, we select H_2 and O_2. Fig. 41 shows measured angular distributions[112] for Penning ionization of these molecules by $He^*(2^1S)$. The strongly forward scattering with E' < E for H_2 is quite similar to the situation for Ar. Again the Q value is very close to V_s as found in the nonreactive scattering analysis (see Fig. 36).

Similar results (not shown) obtain for N_2 and CO targets;[112] the non-reactive results for these systems[104] are in preparation for publication. Reliable distributions for production of HeH^+ through rearrangement ionization have not yet been obtained, though abundant HeH^+ product has been observed in a total ion collection mode. Merged beam results of Neynaber _et_ _al_.[125] strongly support forward scattering of HeH^+ at higher relative energies; these data pertain to a singlet-triplet mixture (∿12:1 ^3S to ^1S). Further discussion of the merged beam experiments is given below and in Section III.D.1.c. The observation of a nearly Franck-Condon vibrational population in H_2^+ [18] is consistent with the relatively large internuclear distances for ionization required by the potential surface, as well as with the similarity between the H_2 and Ar angular distributions.

Penning ionization of O_2 apparently proceeds through qualitatively different interactions than that of closed-shell atoms and molecules. The angular distributions are much broader, with considerable energy released into translation, as indicated in Fig. 41. It is plausible that the lowest $^3A''$ potential surface (C_s symmetry) is highly attractive due to a covalent-ionic avoided crossing with another $^3A''$ state (crossing radius ∿4 Å); ionizing transitions occurring over a deep potential well will give enhanced product translation in a two-body approximation. The attractive surface also is likely to cross lower-lying repulsive surfaces correlating with dissociating O_2 states, thus giving rise to competition between Penning ionization and dissociative excitation. Observation of atomic O emission in flowing afterglow spectroscopy[126] by collision of O_2 with triplet He^* has been similarly interpreted. The form of the angular distributions, with a bump occurring near the usual closed-shell peak position and overlying a broader, flatter curve, suggests that both the usual weakly repulsive (in this case diabatic) and the attractive (adiabatic) mechanisms are at play. Product energy analysis will be highly informative on this point. Other support for the attractive mechanism comes from the observation of "sticky collision bumps" in the angular distribution of K + O_2.[127] The non-Franck-Condon vibrational distributions in O_2^+ states formed from reaction with ^{3}S He[126] is also consistent with an attractive surface, since harder collisions at smaller distances would strongly perturb O_2 during the ionizing transition. Reaction to form HeO^* on the ionic surface is not energetically possible for O_2, but can be expected for more weakly bound O atoms on the basis of similar reactions seen with Ar^*.[128]

Measurements on $He^*(2^1S)$ Penning ionization of closed-shell polyatomic molecules[129] give results very similar to Ar and the closed-shell diatomic systems. Fig. 42 displays CO_2^+ and CH_4^+ angular distributions from ionization of the parent molecules. While $Q < 0$ for CH_4, $Q \simeq 0$ for CO_2, suggesting a somewhat less repulsive interaction in this case. As in the diatomic systems, relatively large amounts of electronic and vibrational energy (usually several eV) are generally deposited in the Penning molecular ion, and in the polyatomic systems especially this produces fragmentation of the parent ion similar to that found in mass spectrometry. Measurements of the fragment ion angular distributions[129] show peaking at the same laboratory angle as the parent, with broadening due to recoil imparted by the neutral fragment. Fig. 43 gives the results for CH_3^+ from $He^*(2^1S) + CH_4$, compared to a prediction from the quasi-equilibrium theory (QET) of mass spectra.[130] The energy deposition function for CH_4^+ is taken from the He I photoelectron spectrum, and the analysis assumes a two-step sequence of Penning ionization followed by fragmentation.

Penning ionization in the Ne^* + Ar system also yields sharp forward scattering, as shown in Fig. 44. Here the product distributions may be much more important to the determination of the incoming potential, since the elastic scattering (Fig. 38) is structureless at wide angles, and the kinematics of the product angular distributions are more favorable than for He^*. The Ne^* experimental work is still in progress at Pittsburgh.

Neynaber and Magnuson[125,131-135] have carried out merged-beam experiments on a number of the Penning systems, including He^* + H_2, H, and D, and Ne^* + Ar, Kr. Although the contributions of singlet and triplet He cannot be separated experimentally, statistical arguments were used to deduce that the composition of the He^* beam, formed by charge exchange with Cs vapor, is $2^3S/2^1S = 12$. While the merged-beams technique cannot yield angular distributions of the product ions, displacement of the measured product energy distributions with respect to the center-of-mass indicates the preferred hemisphere (forward or backward) for product scattering. Penning ionization of H_2 was not reported, but, as mentioned above, HeH^+ was found predominantly in the forward hemisphere.[125] Penning ionization of D,[134] while beset by experimental difficulties, gave sharp forward scattering at high energies (E > 1 eV), and a distribution symmetric about the center-of-mass at 100 meV. The symmetric distribution suggests that most of the D^+ is formed by tunnelling through the centrifugal barrier in the HeD^+ effective potential. This phenomenon may also be responsible for the small but significant amount of backward scattering in the $He^*(2^1S)$ + Ar distributions. Ar^+ and Kr^+ energy distributions from Ne^* Penning ionization[133,135] also indicated mainly forward scattering, in agreement with the crossed beam results cited above.

III.D.1.c. Total and Ionization cross sections

The total cross sections can easily be calculated once the potential has been determined. As the magnitude of the total cross section is mainly determined by the long range van der Waals attraction, the width of the potential has only a negligible influence. The velocity dependence of the total elastic cross section calculated from the potential for $He(2^3S)$ + Ar (see Fig. 34) is shown in Fig. 45. For energies above 10 meV the cross section shows the well-known glory oscillations. At lower energies the effect of the orbiting resonances is clearly noticeable. The total cross section, i.e. the sum of the elastic and inelastic cross sections, has been measured by Rothe et al.[10] and by Trujillo.[136] As the inelastic cross section is negligible compared with the elastic one, the data are directly compared with the calculation in the figure. The average cross section calculated from the Schiff-Landau-Lifshitz (SLL) approximation[42] is given by the straight line. The absolute size of the total cross section averaged over the glory oscillations in determined only by the van der Waals constant, and should be given quite accurately by the SLL formula. Both experimental results lie below the predicted curve. Trujillo states an absolute uncertainty of 5% for his recent data, which are ∿40% below our calculation at the glory maximum 1.4 km s^{-1}. The van der Waals constant, C, has an estimated error of less than 15%,[137] which introduces a 6% error in the calculated cross section σ since $\sigma \propto C^{2/5}$. Therefore the magnitudes of the experimental and theoretical curves are outside their stated uncertainties, although the positions of the glory maxima agree well.

The calculated total elastic cross section for $He(2^1S)$ + Ar is given elsewhere.[102] There are currently no data for comparison. Trujillo has also measured cross sections for $He(2^3S)$ + Ne and Kr.[136] Using essentially the same apparatus Harper and A. C. H. Smith[138] have extended the cross section measurements to He(2^3S) + H_2, CO, O_2, N_2 and Ne^* + He, Ne, Ar, Kr, H_2, CO, N_2, O_2.

Assuming that Penning and associative ionization represent the only quenching channel, total quenching cross sections calculated from Eq. (17) using an optical potential fitted to the differential scattering data may be compared directly to measured total ionization cross sections. Fig. 46 shows a comparison between the total ionization cross section energy dependence predicted from the potential of Fig. 34 and experimental results. Experimental data from three different groups are included. Illenberger and Niehaus[139] and Pesnelle et al.[140] have measured the velocity dependence of the total ionization cross section. Their relative data have been normalized to the absolute flowing afterglow rate constants of Lindinger et al.[141] Within the quoted accuracy of <30% for the absolute value, all the data are in very good agreement. On a relative scale the data of Illenberger and Niehaus coincide with the calculation within experimental error, while the data of Pesnelle et al. disagree somewhat at higher collision energies. The one data point from Riola et al.[142] is an absolute determination in a crossed-beam experiment. The relative velocity was not measured at the same time as the total cross section, but was determined in a later experiment. As the He^* beam source was modified between the two experiments, it is believed that the velocity was changed by this modification.

The point at which the kinetic energy equals the well depth is indicated by ε in Fig. 46. At lower energies one observes the expected increase in the ionization cross section. The sharp peaks superimposed on the gradual rise are due to orbiting or shape resonances. They are caused by partial waves with high orbital angular momentum quantum numbers J, as indicated in Fig. 46, which can no longer overcome the centrifugal barrier, but must tunnel through it. If the kinetic energy coincides with that of a quasibound, predissociating state, the probability for finding the particle inside the barrier becomes large. As these resonances are very narrow, the particle stays for a long time in a region where the width $\Gamma(r)$ is non-negligible and is strongly absorbed.

The vibrational quantum number v for a resonance was obtained by counting the nodes in the wavefunction; the J value can be obtained directly by inspecting the calculated opacities. For $v = 0$ there should also be resonances below $J = 16$, but they are so narrow that they have not been found, although the cross section has been calculated at 75 energies below ε. For the $v = 1$, $J = 10$ resonance the cross section reaches a value of 131 $\mathring{A}^2$, which is off the scale in Fig. 46. For the higher partial waves the resonances become broader and quickly blend into the smooth background. These resonances are very sensitive to the exact form of the attractive part of the potential. So far, they have not been observed experimentally. Their observation will be very difficult because they are so narrow and their energy lies below 1 meV.

It is generally assumed that the close-collision approximation, which gives an inelastic cross section proportional to $E^{-1/3}$ for a r^{-6} potential, should be valid at low collision energies. The chain curve, marked cc (for close collision), in Fig. 46 has an $E^{-1/3}$ dependence, and it can be seen that the average cross section rises faster and does not show any simple power law. The close-collision approximation assumes that all particles which can overcome the centrifugal barrier are equally absorbed independent of the angular momentum. By inspecting the calculated opacities one sees that this approximation does not hold.

For He(2^1S) + Ar the shape of the total ionization cross section is substantially different. It is shown in Fig. 47 . The solid curve has been calculated from the potential determined in Freiburg, while the dashed curve gives the Pittsburgh result. They both agree reasonably well with the experimental data, which have been measured by Illenberger and Niehaus[139] and by Pesnelle _et al_.[140] Their relative data have again been normalized to the absolute rate constants measured by Lindinger _et al_.[141] On a relative scale the agreement is very good, except at low velocities where the resolution broadening of the experiment is largest. The absolute value of the rate constant is known to within 30% so that the agreement is also satisfactory on an absolute scale. The total cross section has also been measured by Riola _et al_.[142] in a beam experiment. Their value is given by the one data point at 60 meV. Good agreement is obtained within experimental error.

The temperature dependence of the quenching rate constant k(T) as measured by Lindinger _et al_.[141] can be obtained by a thermal average over the velocity dependence of the cross section. Good agreement is obtained, both for $He(2^1S)$ and $He(2^3S) + Ar$, as shown in Fig. 48.

III.D.1.d. Qualitative Interpretation of Structure in He^* Potentials.

In seeking to rationalize the repulsive structure found in the $He^*(2^1S)$ + Ar, Kr, Xe and D_2 interactions, we will examine the model for noble gas partners proposed by Siska *et al.*[108,109,112] and the rationale presented by Isaacson *et al.*[121] for $He^*(2^1S) + D_2$. In the model potential function of Siska *et al.*,[108,109] the low-energy repulsion is represented by a switchover from alkali-like--closed shell repulsive behavior to ion core (He^+)--closed shell Rydberg-like behavior with decreasing internuclear distance, i.e.,

$$V_0(r) = [1-f(r)]V_+(r) + f(r)V_*(r), \qquad (51)$$

with $V_*(r)$ the alkali-like potential, representing the dispersion attraction and overlap repulsion involving the 2s electron on He^*, $V_+(r)$ the ion-molecule interaction (He^+-X), including the attractive part, and f(r) a switchover function, $f \to (0, 1)$ as $r \to (0, \infty)$. Jordan *et al.*[108,109] were able to fit $He^*(2^1S)$ scattering from Ar, Kr, and Xe varying only $V_*(r)$ and f(r), while leaving $V_+(r)$ fixed as determined by the ion-atom scattering experiments of Smith *et al.*[113,114] and Weise and Mittmann.[144] This potential model appears to favor the substantial anisotropy found by Isaacson *et al.*[121] for $He^*(2^1S) + H_2$, since the core He^+-H_2 interaction V_+ is likely to resemble strongly the Li^+-H_2 interaction, which is known from *ab initio* calculations and from experiment to be highly anisotropic. The model does not provide a way of rationalizing the marked dissimilarity between singlet and triplet interactions, but the *ab initio* calculations offer a reasonable explanation. Examination of the electronic wave function reveals that in the region of the repulsive structure for

$He^*(2^1S) + H_2$, the 2s orbital has acquired appreciable 2p character, i.e., it is hybridized. This enables the outer electron to remove itself largely to the far side of He, since its exchange interaction with the partner's closed shell is repulsive. The He^+ core is thus partially bared to the partner, and the ion-atom interaction becomes important. The hybridization is enhanced by the small energy gap (0.602 eV) between the $1s2s2^1S$ and $1s2p2^1P$ states of He. For triplet He^*, the 2^3S-2^3P gap is nearly twice as large (1.144 eV) and hybridization becomes less favorable energetically; hence the ion-atom core interaction is more effectively shielded by the 2s electron. The triplet repulsion is thus expected to increase more smoothly in the low-energy regime, nicely illuminating the experimental finding of a much subtler structure in the repulsion for $He^*(2^3S) + Ar$.[100]

This description appears to bear some relation to the avoided crossing between the $2s\sigma_g$ and $2p\sigma_g$ states in the kindred $He^*(2^1S) + He$ system.[84] This avoided crossing produces a $C\,^1\Sigma_g^+$ potential curve with a barrier maximum (217 meV, 2.06 Å) and a deep inner minimum. While the corresponding states in $He^*(2^1S) + Ar$ are not expected to approach each other closely, some interaction between them seems plausible. Such an interaction would be weaker for the triplet system, again because of the larger asymptotic splitting.

III.D.2. Scattering in Excitation Transfer Systems

III.D.2.a. Elastic Scattering

As a general rule, when Penning ionization is energetically possible, it is overwhelmingly preferred to other electronically inelastic channels. Thus, He^* efficiently Penning ionizes every collision partner except He and Ne at thermal energies. $He^*(2^1S,\ 2^3S)$ + Ne is therefore a prototype system for electronic excitation transfer at thermal energies, both because of its relatively unique accessibility to ab initio as well as experimental methods, and because it lends itself to model calculations using a spherically symmetric potential matrix.

Elastic scattering measurements for He^* + Ne have now been reported by Chen, Haberland and Lee,[39] by Haberland, Oesterlin and Schmidt,[77] and by Martin et al.[75] and Fukuyama and Siska.[145] The differential cross sections are complicated by the contributions of Ne^* metastables, formed by excitation transfer and subsequent radiative cascade, and of product uv photons to the scattered intensity. The Ne^* contribution was isolated in the double-quenching-lamp experiments of Haberland et al.,[76,77] by use of a Ne quenching lamp in the detector; however, because the Ne lamp was less than 100% efficient (∿70-85%), quantitative elastic scattering data could not be extracted except at very low energy (25 meV) where the Ne^* signal was negligibly small. These data are shown in Fig. 49, along with a fit for an assumed single-channel potential. Both the Pittsburgh and Freiburg laboratories have used time-of-flight (TOF) measurements to separate the elastic scattering from product Ne^* and photons; these results will be discussed below (see Sec. III.D.2.c).

In the 64 meV angular distribution for $He^*(2^1S)$ + Ne of Fukuyama and Siska,[145] shown in Fig. 50 along with a single-channel fit to small angles, a shoulder appears at θ_{LAB} ∿30-35°. This feature is similar in form to that for $He^*(2^1S) + D_2$, and was interpreted again as a repulsive rainbow. However, from work in progress at Pittsburgh on the higher energies, a second hump appears at wider angles. This effect may only be interpretable in a multichannel framework, where the effective single-channel potential is strongly perturbed by avoided crossings. Optical model and two-state close-coupling analysis have been performed for the 64 meV distribution.[145] Unpublished data from Freiburg indicate that the $He(2^3S)$ + Ne potential has a shoulder near 90 meV.

Other work in atom-atom systems includes $Ar^*(^3P_{2,0})$ + Kr and Xe[75] and Kr^* + Xe.[110] The Ar^* + Kr angular distribution at 63 meV, given in Fig. 51, shows, in addition to a normal rainbow expected by analogy with K + Kr, an additional array of bumps at wider angles centered around = 31°. Earlier interpreted as Kr^* arising from the excitation transfer,[146] this structure has now been shown by TOF measurements[75] to be elastic scattering. The bump at 90° is established as a Kr^* peak. The origin of the secondary features is likely related to curve crossing with the product channels, speculated to occur in the attractive part of the interaction for the major Kr $5p[\frac{3}{2}]_2$ channel.[147] Model calculations are under way at Pittsburgh to assess this question. Ar^* + Kr van der Waals parameters derived by Winicur _er al_.[146] establish a very close similarity with K + Kr. Results for Ar^* + Xe, however, indicate an appreciably smaller well depth[75] than for K + Xe. It also seems quite likely that the low-energy repulsion is not as similar to that of the alkalis as is the attractive part of the potential. Winicur _et al_.[146] have carried out an approximate optical model analysis, but this suffers from the uncertainty in the repulsion for the input channel as well as from the basic limitations discussed in Section II.

Winicur _et al_.[149-151] have also published studies of $Ar^* + N_2$[150] and HBr[149,151] scattering. While the potential surfaces of the input channels may be highly anisotropic, optical model analysis in these cases is less likely to suffer from "recrossing" contributions, because part of the electronic energy must be rapidly and nearly irreversibly converted to vibrational energy in the newly excited molecule. The Ar^* + HBr cross section and van der Waals potential closely resemble those of K + HBr;[151] this suggests indirectly that covalent-ionic interaction may govern the quenching in this system. Reaction to form $ArBr^*$ is also energetically possible, and is considered probable. Nonetheless, the total quenching cross section derived is nearly an order-of-magnitude smaller than that obtained from flowing afterglow experiments.

III.D.2.b. Excitation Transfer Cross Sections

Very little information exists on magnitudes or energy dependences of electronic energy transfer cross sections in atom-atom systems, aside from that inferred from classical kinetics. Some information on metastable noble gas-molecule quenching cross sections from observation of molecular emission in crossed beams is now becoming available, and is discussed below. The usual optical model analysis of elastic scattering employs a local, absorptive potential which may not be very useful in the atom-atom systems, and the cross sections therefrom may not be reliable. For $He^*(2^1S)$ + Ne, the earlier results of Chen, Haberland and Lee[40] from optical model analysis of the elastic scattering at 63 meV are likely to be less reliable because the data were not corrected for Ne^* contributions. Fukuyama and Siska[145] have used both optical model and close-coupling (two-channel) methods at 64 meV on corrected data to obtain cross sections in the range 2-3.5 $\mathring{A}^2$. These compare well with the flowing afterglow work of Schmeltekopf and Fehsenfeld,[151] who find a thermal cross section of 4.7 $\mathring{A}^2$. The crossed beam experiments at Freiburg[76,77,152] and Pittsburgh[75,145] show, from the appearance of the Ne^* contribution, that the cross section rises rapidly with collision energy. Each channel cross section appears to increase quickly near threshold and then level out, producing an increase in the total quenching as each new channel opens. Integration of transformed Ne^* angular distributions (see below, Section III.D.2.c) promises to provide the first reliable energy dependencies for the various channels. Flowtube results of Lindinger _et al_.[141] on $He^*(2^3S)$ + Ne show a strong positive temperature dependence from 300K to 900 K, which correlates with a marked rise in scattered Ne^* intensity with collision energy observed by Oesterlin, Haberland and Schmidt.[152]

Cross section energy dependencies for specific product channels in the Ar^* + N_2 system have been directly investigated by Lee and Martin,[153] Muschlitz et al.[154,155] and Bel Bruno and Krenos[156] through observation of N_2^* emission from beam-gas cell or crossed beam arrangements. Total quenching cross sections for Ar^* and Kr^* by O_2 have been reported by Gersh and Muschlitz[157] using the beam-gas method, in which the $^3P_0$ and $^3P_2$ states were resolved through the use of an inhomogeneous magnetic deflecting field. While the $Ar^* + N_2(X) \rightarrow Ar + N_2^*(C)$ cross section shows a strong, line-of-centers energy dependence, the Ar^*, Kr^* + O_2 quenching cross sections are at most weakly energy dependent. This suggests that the N_2 system is repulsive in the incoming channel, the O_2 attractive. An anticipated correlation is evident then between these systems and the corresponding He^* cases.

III.D.2.c. Product Angular Distributions

As introduced in Section III.D.2.a, angular distribution measurements in noble gas excitation transfer (non-Penning) systems have been shown to contain an unexpected bonus: angular distributions for formation of electronically excited products by direct electronic-to-electronic energy transfer. Although the new states freshly formed at the collision center are generally not metastable, the metastable states can be reached by one or a sequence of radiative transitions and will eventually (after $\sim 10^{-7}$ sec or less) be populated according to the relative overall emission rates for going to the ground and metastable states. Estimation of this branching ratio is difficult for states high in the newly excited atom's spectrum, but for $Ar^*(^3P_{2,0})$ + Kr the ratio has been measured by observation of Kr^* emission.[158] The metastables are the only atomic remains of the inelastic collision surviving long enough to reach the detector surface. Far-uv photons produced by transitions to the ground state, also detectable by secondary emission, only contribute appreciably to the observed intensity when the total inelastic cross section becomes quite large or when the transitions are highly energetic, as for Ne. This contribution is isotropic.

Two methods have been used for isolating the transfer angular distribution in He^* + Ne. By installing a quench lamp operated with Ne in the detector, Haberland <u>et al</u>.[76,77,152] have used a double-subtraction method to derive the total Ne^* angular distributions; data for $He^*(2^1S)$ + Ne are shown in Fig. 52. State assignments were made by comparing the observed peak positions with a Newton diagram drawn for the most probable beam velocities and the known states of Ne; an example is shown in Fig. 53. Although the assignments can be ambiguous, the distributions as a function of energy as in Fig. 52 often help to relieve the ambiguity. For $He^*(2^1S)$ + Ne, strong forward scattering of the various product states enables the $3s_2$, $3s_4$ and $3s_5$ states of Ne to be identified from the Newton diagram. As mentioned earlier, the Ne quenching is not 100% efficient, and hence is velocity dependent; Ne^* atoms with higher lab velocities are less effectively quenched, and subtraction yields lower intensity for these atoms.

The second method, introduced by Martin et al.,[75] employs TOF measurements in regions of the angular distribution where excited atom products appear to be present. Both the Pittsburgh and Freiburg groups are now using the TOF method on the He^* + Ne system. Rather than the usual pulsing of the scattered products with a mechanical chopper in front of the detector, the technique employs an electrostatically pulsed electron beam to excite the metastable beam. The mode (TOF or angular distribution) and TOF resolution are then selectable without modification of the experimental hardware. While obtaining a complete product angular distribution entails many TOF spectra (each requiring 10^2-10^4 sec to collect), one can make unambiguous state assignments and recover the elastic and photon components of the intensity at each angle. It has been found that the elastic scattering is reasonably smooth at wide angles for He^* + Ne, and thus the various product angular distributions can be recovered with the original high datum point density by interpolating the underlying elastic distribution extracted from the TOF spectra. Fig. 54 shows assigned TOF spectra for $He^*(2^1S)$ + Ne at 64 meV, and Fig. 55 presents the corresponding Ne^* angular distribution obtained by the TOF method at the same energy (cf. Fig. 52, 66 meV). In unpublished work at Freiburg and Pittsburgh, the prominent peaks near the center-of-mass for $He^*(2^1S)$ + Ne at E = 89 and 113 meV in Fig. 52 are shown to originate from a $2p^5 4d$ state, and the wide-angle bump in the TOF angular distribution of Fig. 55 from the $2p^5 3d$, $3s_1$ manifold.

The singlet angular distributions are dominated by strong forward scattering with some backward intensity as well. It is therefore easy to assign the states of Ne by reference to an appropriate Newton diagram. The width of the forward scattering peak for the endoergic states ($3s_2$, $2p^5 4d$) grows smaller with increasing collision energy, in accord with the increasing number of orbital angular momenta which can contribute to each inelastic channel. For the exoergic states ($3s_4$,$3s_5$,$3s_1$) the widths are nearly invariant with energy. No triplet angular distributions have so far been measured. The triplet beam intensity is roughly a factor of seven lower and the cross section a factor of 20 lower than in the singlet case. The distributions published[152] as a conference abstract are therefore heavily contaminated by singlets.

A two-state close-coupling analysis has been reported[145] at 64 meV for He*(2^1S) + Ne using $3s_2$ as the product channel and assuming the (diabatic) product potential curve crosses the incoming curve on its repulsive wall. The elastic scattering was fitted to yield a state-to-state cross section of 2.1 Å^2. The Ne* angular distribution calculated from the resulting potential matrix agreed fairly well with that part of the total Ne* scattering assigned to $3s_2$. Including a third, exoergic state does not substantially perturb the two-state results for cross sections into the exoergic channel as large as 0.5 Å^2. The opening of the highly probable $2p^5 4d$ channel at higher energies will complicate the analysis further.

Martin et al.[75] have also reported Kr^* and Xe^* peaks in Ar^* + Kr, Xe scattering deduced from TOF spectra; the transfer angular distributions are shown in Fig. 56. These two systems are of contrasting degrees of complexity, in that the spectrum of states is limited to two for $Ar^*(^3P_2)$ + Kr: $5p[\frac{3}{2}]_2$ and $5p[\frac{3}{2}]_1$,[158] but at least 28 states of Xe^* are known to be populated from flowing afterglow measurements.[159] The angular and TOF data again demonstrate sharp forward scattering for both exoergic and endoergic states, and good agreement with major states found in the emission spectroscopy work. The energy dependence of the Xe^* angular distribution is expected to be spectacular because of the myriad new channels opening up at higher energies. Measurements are in progress at Pittsburgh.

IV. Future Directions

The new levels of experimental resolution, data quantity and quality, and sophistication of interpretation of the differential scattering results presented here, combined with concomitant blossoming of the ab intitio theory, have produced an exciting situation with few precedents in the field of molecular collision dynamics. Continued mutual feedback between theoretical and experimental efforts should rapidly increase and deepen our knowledge of excited state collision dynamics. This interaction will become even more important when we move from atom-atom systems to atom-molecule systems in the future, and enable the tackling of even more challenging systems in which the alkali-like chemical nature of the noble gas metastables competes in luminescent chemical reactions with the excitation transfer and ionization channels. Experimental studies of elastic and inelastic scattering of metastables by halogen containing molecules are already underway, as well as measurements of optical emission in reactions under beam conditions. With recently improved potential curves for both ground state and excited states of the diatomic noble gas halides, chemiluminescence in metastable atom-halogen reactions can now provide information on energy partitioning in the initial products which is largely unavailable for the corresponding alkali reactions. In these investigations we can draw on our extensive knowledge of alkali-halogen collision dynamics derived from beam studies of the past two decades to elucidate subtle differences between noble gas halide excimer formation and the corresponding alkali reaction, as well as to clarify the role of competing processes.

Differential scattering experiments with Ne*, etc., beams state selected with a tuneable dye laser are near realization. Differences in the potential energy curves and reaction probabilities for the $^3P_2$ and $^3P_0$

states will provide valuable insight into the role of the core ion on the collison dynamics and electronic structure as well as clarify the relative importance of the two states in macroscopic processes. Experiments using a metal-atom crossed beam, also now underway at Freiburg, promise a revealing contrast to the weak van der Waals interactions thus far studied.

Our hope is that, through continued experimental scattering work and theoretical studies on these and other systems, excited state interactions will become as well characterized as those for the ground state are now. With important laser applications already discovered for systems containing metastable noble gas atoms, unusually fast "transfer" of knowledge gained on microscopic collision dynamics in these studies to applied areas may be expected. However, because of the complexity of many of these highly energetic systems, future progress will likely entail careful investigations of all the competing processes by the combination of various experimental and theoretical methods.

Table I. Characteristics of Some Metastable Species

Atoms	State	Excitation[a] Energy (in eV)	Ionization[a] Potential (in eV)	Lifetime (Sec.)		Polarizability ($Å^3$)[b]
He	$2\,^3S_1$	19.820	4.768	4.2×10^{3} [c]		46.86[e]
				6.2×10^{5} [d]		(24.3[f])
	$2\,^1S_0$	20.616	3.972	3.8×10^{-2} [g]		118.9[e]
				2.0×10^{-2} [h]		
				1.95×10^{-2} [i]		
Ne	$^3P_2$	16.619	4.946	>.8[i]	24.4[k]	27.8[f]
	$^3P_0$	16.716	4.849		430[k]	(23.6[f])
Ar	$^3P_2$	11.548	4.211	>1.3[i]	55.9[k]	47.9[f]
	$^3P_0$	11.723	4.036		44.9[k]	(43.4[f])
Kr	$^3P_2$	9.915	4.084	>1[i]	85.1[k]	50.7[f]
	$^3P_0$	10.563	3.437		.488[k]	(47.3[f])
Xe	$^3P_2$	8.315	3.815		149.5[k]	63.6[f]
	$^3P_0$	9.447	2.683		.078[k]	(59.6[f])
H	$2\,^2S_{1/2}$	10.199	3.400	1/7[l]		

a) C.E. Moore, "Atomic Energy Levels" Vol. I, II and III (U.S. Government Printing Office, Washington, D.C., 1949).

b) The values in parenthesis are those for the corresponding alkali atoms.

c) H. W. Moss and R. J. Woodworth, Phys. Rev. Lett. 30, 775 (1973).

d) H. R. Grim, Astrophys. J. 156, L103 (1969).

e) G. A. Victor, A. Dalgarno, and A. J. Taylor, J. Phys. B1, 13 (1968).

f) R. A. Molof, H. L. Schwartz, T. M. Miller, B. Bederson, Phys. Rev. A10, 1131 (1974).

Table I. Continued

g) A. S. Pearl. Phys. Rev. Lett. 24, 703 (1970).

h) R. S. Van Dyck, Jr., C. E. Johnson, and H. A. Shugart, Phys. Rev. Lett. 25, 1403 (1970).

i) G. W. F. Drake, G. A. Victor, and A. Dalgarno, Phys. Rev. 180, 25 (1969).

j) Lifetimes measured for the mixture of $^3P_0$ and $^3P_2$ states, R. S. Van Dyck, Jr., C. E. Johnson, and H. W. Shugart, Phys. Rev. A5, 991 (1972).

k) N. E. Small-Warren and L. Y. Chin, Phys. Rev. A11, 1777 (1975).

l) G. Breit and E. Teller, Astrophys. J. 91, 215 (1940).

Table II. Helium Quench Lamp Characteristics

Operating current	50-75 mA
Operating voltage	2.5-3.0 kV DC
Startup voltage	4.5 kV
Helium pressure	1-5 torr (flowing)

Table II. Helium Quench Lamp Characteristics

Operating current	50-75 mA
Operating voltage	2.5-3.0 kV DC
Startup voltage	4.5 kV
Helium pressure	1-5 torr (flowing)

R[Å]	V_g[meV]	V_u[meV]
0.5		9867.
0.75		- 501.
1.00		-2472.
Min. (1.05)		-2492.
1.25		-2122.
1.50		-1359.
1.75		- 704.
2.00		- 303.
2.25		- 101.
2.50	163.	- 82.0
2.80	109.	32.6
3.00	90.1	44.9
Max. (3.15)	77.2	47.4
3.20	73.4	47.2
3.40	59.8	44.1
3.60	48.0	38.4
3.80	37.5	31.5
4.00	28.2	24.7
4.20	20.3	18.5
4.40	14.2	13.3
4.60	9.6	9.2
4.80	6.4	6.3
5.00	4.1	4.2
5.25	2.4	2.6

Table III: Numerical values for the singlet potentials $V_g = C^1 \Sigma_g^+$ and $V_u = A^1 \Sigma_u^+$

R [Å]	V_g [meV]	V_u [meV]
0.5		10990.
0.75		98.
1.00		-1920.
Min. (1.05)		-1947.
1.25		-1615.
1.50		- 842.
1.75		- 232.
2.00		- 36.1
2.25		37.6
2.40		52.0
2.60	144.7	56.8
Max. (2.75)	127.6	57.0
3.00	97.9	53.5
3.20	74.8	46.5
3.40	53.8	37.3
3.60	36.3	27.6
3.80	23.6	18.9
4.00	15.1	12.6
4.20	9.6	8.3
4.40	6.1	5.4
4.60	3.8	3.5
4.80	2.4	2.2
5.00	1.5	1.4
5.25	0.82	0.78

Table IV: Numerical values for triplet potentials $V_g = c^3\Sigma_g^+$ and $V_u = a^3\Sigma_u^+$

Table V. Van der Waals Parameters for $\mathrm{He}^*(2^1S, 2^3S)$ and Li Interactions

	$\mathrm{He}^*(2^1S)$		$\mathrm{He}^*(2^3S)$		Li	
Partner	ε,meV	r_m,Å	ε,meV	r_m,Å	ε,meV	r_m,Å
Ne	$0.4^{a,b}$	$7.14^{a,b}$	$0.4^{a,b}$	$7.1^{a,b}$	$0.1^{d,b}$	$6.20^{d,b}$
	$0.6^{c,b}$	$6.2^{c,b}$				
Ar	$3.8^{e,b}$	$5.55^{e,b}$	$3.6^{g,b}$	$5.66^{g,b}$	5.6^{h}	4.86^{h}
	$4.2^{f,b}$	$5.67^{f,b}$	$5.1^{f,b}$	$5.17^{f,b}$		
Kr	6.5^{i}	5.6^{i}	5.5^{i}	5.4^{i}	8.4^{d}	4.95^{d}
	6.8^{f}	5.69^{f}				
Xe	11.0^{f}	5.69^{f}			12.8^{d}	4.95^{d}

a) Ref. 77.

b) These parameters may not be reliable owing to the insensitivity of the scattering data to very weak van der Waals attraction.

c) Ref. 145.

d) Ref. 119

e) Ref. 102

f) Ref. 108, 109, and unpublished work.

g) Ref. 100

h) Ref. 118

i) Ref. 103, 104

REFERENCES

1. F. M. Penning, Naturwissenschaften, 15, 818 (1927); Z. Phys., 46, 335 (1928); Z. Phys., 57, 723 (1929); Proc. Roy. Acad. Sci. Amsterdam, 32, 341 (1929); Z. Phys., 72, 338 (1931)
2. F. Mohler, P. Foote, and R. Chenault, Phys. Rev., 27, 37 (1926).
3. E. O. Lawrence and N. Edlefsen, Phys. Rev., 34, 233 (1929).
4. F. Mohler and C. Boeckner, Nat. Bur. Stand. J. Res., 5, 51 (1930).
5. K. Freudenberg, Zeit. f. Physik, 67, 417 (1931).
6. B. Gudden, Lichtelektrische Erscheinungen, Springer-Verlag, Berlin (1928) p. 226.
7. F. Mohler and C. Boeckner, Nat. Bur. Stand. J. Res., 5, 399 (1930).
8. J. A. Hornbeck and J. P. Molnar, Phys. Rev., 84, 62 (1951).
9. W. P. Sholette and E. E. Muschlitz, Jr., J. Chem. Phys., 36, 3368 (1962).
10. E. W. Rothe, R. H. Neynaber and S. M. Trujillo, J. Chem. Phys., 42, 3310 (1965).
11. V. Cermak, J. Chem. Phys., 44, 3781 (1966).
12. D. L. King and D. W. Setser, Ann. Rev. Phys. Chem., 27, 407 (1976).
13. R. J. Pressley, Handbook of Lasers with Selected Data on Optical Technology (Chemical Rubber Co., Cleveland, Ohio, 1971).
14. W. H. Hughes, J. Shannon, A. Kolb, E. Ault, and E. Bhaumik, Appl. Phys. Lett., 23, 385 (1973).
15. P. W. Hott, J. C. Swingle, and C. K. Rhodes, Appl. Phys. Lett., 23, 245 (1973).
16. W. M. Hughes, J. Shannon, and R. Hunter, Appl. Phys. Lett., 24, 488 (1974).
17. A. Niehaus, Ber. Bunsenges. Phys. Chem., 74, 632 (1973).
18. H. Hotop, Radiat. Res., 59, 379 (1974).

19. D. R. Herschbach, Advan. Chem. Phys., 10, 319 (1966).

20. C. A. Brau and J. J. Ewing, J. Chem. Phys., 63, 4640 (1975).

21. J. E. Velazco and D. W. Setser, J. Chem. Phys., 62, 1990 (1975); L. A. Gundel, D. W. Setser, M. A. A. Clyne, J. A. Coxon, and W. Nip, J. Chem. Phys., 64, 4390 (1976) and references therein.

22. M. L. Bhaumik, R. S. Bradford, Jr., and E. R. Ault, Appl. Phys. Lett., 28, 23 (1976).

23. C. A. Brau and J. J. Ewing, J. Chem. Phys., 63, 4640 (1975).

24. W. H. Miller, J. Chem. Phys., 52, 3563 (1970)

25. H. Nakamura, J. Chem. Soc. Japan, 26, 1973 (1969); 31, 574 (1971).

26. A. P. Hickman, A. D. Isaacson, and W. H. Miller, J. Chem. Phys., 66, 1483 (1977).

27. W. H. Miller, C. A. Slocomb, and H. F. Schaefer, III, J. Chem. Phys., 56, 1347 (1972).

28. A. P. Hickman, A. D. Issaacson, and W. H. Miller, J. Chem. Phys., 66, 1492 (1977).

29. J. C. Bellum and D. A. Micha, Chem. Phys., 20, 121 (1977).

30. A. P. Hickman and H. Morgner, J. Phys., B 9, 1765 (1976).

31. D. A. Micha, in Modern Theoretical Chemistry ed. W. H. Miller (Plenum, New York, 1976), Vol. II, p. 81.

32. T. Ebding and A. Niehaus, Z. Physik., 270, 43 (1974).

33. Z. F. Wang, A. P. Hickman, K. Shobatake, and Y. T. Lee, J. Chem. Phys., 65, 1250 (1976).

34. See for example U. Buck, Adv. Chem. Phys., 30, 313 (1975); Rev. Mod. Phys., 46, 369 (1974).

35. E. F. Greene, A. L. Moursund, and J. Ross, Adv. Chem. Phys., 10, 135 (1966).

36. (a) H. D. Hagstrum, Phys. Rev., 104, 1516 (1956); (b) D. A. MacLeanner, Phys. Rev., 148, 218 (1966); (c) P. J. MacVicar-Whelan and W. L. Borst, Phys. Rev. A, A1, 3141 (1970).

37. (a) J. B. Anderson, R. P. Andres, and J. B. Fenn, Adv. Chem. Phys., 10, 275 (1966); (b) J. B. Anderson, in Molecular Beams and Low Density Gas Dynamics, ed. P. P. Wegener, Dekker, New York, 1974, Chapter 1.

38. G. Brunsdeylins, H.-D. Meyer, J. P. Toennies, and K. Winkelmann, in Rarefied Gas Dynamics, Prog. Astron. Aeron., 51, 1047 (1976).

39. C. H. Chen, H. Haberland, and Y. T. Lee, J. Chem. Phys., 61, 3095 (1974).

40. D. H. Winicur and J. L. Fraites, J. Chem. Phys., 62, 63 (1975).

41. N. F. Mott and H. S. W. Massey, The Theory of Atomic Gollisions, Third Ed., Oxford University Press, 1965.

42. R. B. Bernstein, Advan. Chem. Phys., 10, 75 (1966).

43. E. E. Nikitin, Theory of Elementary Atomic and Molecular Processes in Gases, Oxford University Press, 1974.

44. M. S. Child, Molecular Collision Theory, Academic Press, 1974.

45. W. H. Miller, ed., Dynamics of Molecular Collisions, Parts A and B, Vols. 1 and 2 of Modern Theoretical Chemistry, Plenum Press, 1976.

46. D. Beck, E. F. Greene, and J. Ross, J. Chem. Phys., 37, 2895 (1962).

47. E. F. Greene and J. Ross, in Molecular Beams and Reaction Kinetics, Ch. Schlier, ed., Academic Press, 1970, pp. 86-106.

48. R. M. Harris and J. F. Wilson, J. Chem. Phys., 54, 2088 (1971).

49. W. H. Miller, Chem. Phys. Letters, 4, 627 (1970)

50. L. D. Landau, Z. Phys. Sow Un., 2 46 (1932).

51. C. Zener, Proc. Roy. Soc. A, 137, 696 (1932).

52. E. C. G. Stückelberg, Helv. Phys. Acta, 5, 370 (1932).

53. J. S. Cohen, Phys. Rev. A, 13, 99 (1976).

54. See for example, Methods of Computational Physics, Vol. 10 (1971).

55. R. E. Olson, F. T. Smith, and E. Bauer, Appl. Opt., 10, 1848 (1971).

56. R. D. Rundel, F. B. Dunning, J. P. Howard, J. P. Riola, and R. F. Stebbings, Rev. Sci. Instr., 44, 60 (1973).

57. W. L. Borst, Rev. Sci. Instr., 42, 1543 (1971).

58. B. Brutschy, Ph.D. thesis, Freiburg, 1977; B. Brutschy and H. Haberland, Phys. Rev. A, submitted for publication.

59. G. Watel, private communication.

60. R. J. Champeau and J. C. Keller, J. de Physique, 36, L161 (1975); A. Zastrow, Diplomarbeit, Freiburg, 1977; H. Hotop and A. Zastrow, to be published.

61. R. F. Stebbings, F. B. Dunning, and R. D. Rundel, Proc. Fourth Int. Conf. on Atomic Physics, Heidelberg, 1974.

62. RTV 630, General Electric Co.

63. R. Campargue, A. Lebehot, Ninth Int. Symp. on Rarefied Gas Dynamics p. C11, Göttingen 1974 (eds. M. Becker, M. Fiebig).

64. B. Brutschy and H. Haberland, J. Phys. E, 10, 90 (1977).

65. H. S. W. Massey, Electronic and Ionic Impact Phenomena, vol. 3, Slow Collisions of Heavy Particles, Oxford: Clarendon, 1973.

66. G. A. Victor and K. Sando, J. Chem. Phys., 55, 5421 (1971).

67. R. E. Olson and F. T. Smith, Phys. Rev., A7, 1529 (1973).

68. J. Q. Searcy, Rev. Sci. Instrum., 45, 589 (1974).

69. E. L. Leasure and C. R. Mueller, J. Applied Physics, 47, 1062 (1976).

70. K. Schmidt, Ph.D. thesis, Freiburg, 1976; K. Schmidt and H. Haberland, to be published.

71. H. Maecker and S. Steinberger, Z. angew. Physik, 23, 456 (1967)

72. W. S. Young, W. E. Rodgers, and E. L. Knuth, Rev. Sci. Inst., 40, 1346 (1969).

73. W. J. Hays, W. E. Rodgers, and E. L. Knuth, J. Chem. Phys., 56, 1652 (1972).

74. H. Haberland, B. Brutschy and K. Schmidt. Ninth Int. Conf. Physics on Electronic and Atomic Collisions, Abstracts of Papers (eds. J. S. Risley, R. Geballe), University of Washington Press, Seattle, 1975, p. 443.

75. D. W. Martin, T. Fukuyama, R. W. Gregor, R. M. Jordan, and P. E. Siska, J. Chem. Phys., 65, 3720 (1976).

76. H. Haberland, P. Oesterlin and K. Schmidt, J. Chem. Phys., 65, 3374 (1976).

77. H. Haberland, P. Oesterlin and K. Schmidt, Sixth Int. Symposium on Molecular Beams, Amsterdam, 1977.

78. A. V. Phelps and J. P. Molnar, Phys. Rev., 89, 1202 (1953).

79. A. H. Futch and F. A. Grant, Phys. Rev., 104, 356 (1956).

80. A. V. Phelps, Phys. Rev., 114, 1011 (1959).

81. D. W. Marquardt, J. Soc. Ind. Appl. Math., 11, 431 (1963).

82. T. Fukuyama and P. E. Siska, Chem. Phys. Letters, 39, 418 (1976).

83. W. v. Oertzen and H. G. Bohlen, Physics Reports C, 19, 1 (1975).

84. S. L. Guberman and W. A. Goddard, Phys. Rev. A, 12, 1203 (1975). and references cited therein.

85. G. Peach, J. Phys. B, 11, 2107 (1978).

86. K. M. Sando, Mol. Phys. 21, 439; 23, 413 (1971).

87. B. Schneider and J. Cohen, J. Chem. Phys. 61, 3240 (1974).

88. R. P. Saxon and B. Liu, J. Chem. Phys. 64, 3291 (1976).

89. D. C. Lorents, Physica 82, 19 (1975).

90. D. C. Lorents, Invited Lecture at the Tenth Int. Conference, on the Physics of Electronic and Atomic Collisions, Paris, 1977, G. Watel, ed.

91. B. Brutschy and H. Haberland, Phys. Rev. Let. 38, 686 (1977)

92. R. A. Buckingham and A. Dalgarno, Proc. Roy. Soc. London, Ser. A, 213, 506 (1952).

93. K. Gillen, Progress Report at the Tenth Int. Conf. on the Physics of Electronic and Atomic Collisions, Paris, 1977, G. Watel, ed.

94. R. Morgenstern, D. C. Lorents, J. R. Peterson, and R. E. Olson, Phys. Rev. A 8, 2372 (1973).

95. S. M. Trujillo, Ninth Int. Conf. on the Physics of Electronic and Atomic Collisions, ed, J. S. Risley, Abstracts of Papers, Seattle, 1975, 437.

96. F. D. Colegrove, L. K. Schearer, G. K. Walters, Phys. Rev. 135, A, 353 (1964).

97. S. K. Rosner, F. M. Pipkin, Phys. Rev. A5, 1909 (1972).

98. J. Dupont-Roc, M. Leduc, F. Laloe, Phys. Rev. Let. 27, 467 (1971).

99. N. K. Glendenning, Rev. Mod. PHys. 47, 659 (1975).

100. B. Brutschy, H. Haberland, and K. Schmidt, J. Phys. B, 9, 2693 (1976).

101. B. Brutschy, H. Haberland, H. Morgner, and K. Schmidt, Phys. Rev. Letter, 36, 1299 (1976).

102. H. Haberland and K. Schmidt, J. Phys. B, 10, 695 (1977).

103. P. Altpeter, H. Haberland, W. Konz, P. Oesterlin, and K. Schmidt, J. Chem. Phys. 67, 836 (1977).

104. H. Haberland *et al.*, unpublished work.

105. J. Grosser and H. Haberland, Phys. Letters, 27A, 634 (1968).

106. H. Haberland, C. H. Chen, and Y. T. Lee, in *Atomic Physics 3*, edited by S. J. Smith and G. K. Walters (Plenum Press, 1973), p. 339.

107. J. Bentley, J. L. Fraites, and D. H. Winicur, J. Chem. Phys., 64, 1757 (1976).

108. R. M. Jordan, D. W. Martin, and P. E. Siska, J. Chem. Phys., 67, 3392 (1977).

109. D. W. Martin, R. W. Gregor, R. M. Jordan, and P. E. Siska, J. Chem. Phys., 69, 2833 (1978); R. M. Jordan and P. E. Siska, J. Chem. Phys., 69, 4634 (1978).

110. C. H. Chen and Y. T. Lee, unpublished work.

111. M. T. Leu and P. E. Siska, J. Chem. Phys., 60, 2179 (1974).

112. M. T. Leu and P. E. Siska, J. Chem. Phys., 60, 4082 (1974).

113. F. T. Smith, R. P. Marchi, W. Aberth, D. C. Lorents and O. Heinz, Phys. Rev., 161, 31 (1967).

114. F. T. Smith, H. H. Fleischmann, and R. A. Young, Phys. Rev. A, 2, 379 (1970).

115. Due to a typographical error, the stated value of the C-coefficient of the width function of Ref. 102 is a factor of ten too large. It should read C = 0.0326 eV. The entire width function of Refs. 100 and 102 is too large by exactly a factor or two; the fits to the data and the resulting real part of the potential are not affected.

116. U. Buck and H. Pauly, Z. Phys., 208, 390 (1968).

117. R. Düren, C. P. Raabe, and Ch. Schlier, Z. Phys., 214, 410 (1968).

118. G. B. Ury and L. Wharton, J. Chem. Phys., 56, 5832 (1972).

119. P. M. Dehmer and L. Wharton, J. Chem. Phys., 57, 4821 (1972).

120. J. S. Cohen and N. F. Lane, J. Chem. Phys., 66, 586 (1977).

121. A. D. Isaacson, A. P. Hickman, and W. H. Miller, J. Chem. Phys., 67, 370 (1977).

122. R. K. Preston and J. S. Cohen, J. Chem. Phys., 65, 1589 (1976).

123. Y. T. Lee, J. D. McDonald, P. R. LeBreton, and D. R. Herschbach, Rev. Sci. Instr., 40, 1402 (1969).

124. E. A. Entemann, Ph.D. Thesis, Harvard University, Cambridge, Massachusetts, 1967.

125. R. H. Neynaber, G. K. Magnuson, and J. K. Layton, J. Chem. Phys. 57, 5128 (1972).

126. W. C. Richardson and D. W. Setser, J. Chem. Phys., 58, 1809 (1973).

127. D. O. Ham and J. L. Kinsey, J. Chem. Phys., 53, 285 (1970)

128. M. G. Golde and B. A. Thrush, Chem. Phys. Letters, 29, 486 (1974).

129. R. W. Gregor, M. T. Leu, and P. E. Siska, to be published.

130. See for example the review by A. L. Wahrhaftig in Mass Spectrometry, edited by A. Maccoll, Physical Chemistry, Series 1, V.5 of MTP International Review of Science (Butterworths, London, 1972) pp. 1-24.

131. G. D. Magnuson and R. H. Neynaber, J. Chem. Phys., 60, 3385 (1974).

132. R. H. Neynaber and G. D. Magnuson, J. Chem. Phys., 61, 749 (1974).

133. R. H. Neynaber and G. D. Magnuson, Phys. Rev. A, 11, 865 (1975).

134. R. H. Neynaber and G. D. Magnuson, J. Chem. Phys., 62, 4953 (1975).

135. R. H. Neynaber and G. D. Magnuson, Phys. Rev. A, 14, 961 (1976).

136. S. M. Trujillo, Proc. Ninth Int. Conf. on Physics of Electronic and Atomic Collisions, ed. J. S. Risley and R. Geballe (Seattle: University of Washington Press, 1975) p. 437.

137. K. L. Bell, A. Dalgarno and A. E. Kingston, J. Phys. B, 1, 18 (1968).

138. A. C. H. Smith, London (1977), private communication.

139. E. Illenberger and A. Niehaus, Z. Phys. B, 20, 33 (1975).

140. A. Pesnelle, G. Watel and C. Manus, J. Chem. Phys., 62, 3590 (1975).

141. W. Lindinger, A. L. Schmeltekopf and F. C. Fehsenfeld, J. Chem. Phys., 61, 2890 (1974).

142. J. P. Riola, J. S. Howard, R. D. Rundel and R. F. Stebbings, J. Phys. B, 7, 376 (1974).

143. T. F. O'Malley and H. S. Taylor, Phys. Rev., 176, 207 (1968).

144. H.-P. Weise and H.-U. Mittmann, Z. Naturforsch. Teil A, 28, 714 (1973).

145. P. E. Siska and T. Fukuyama, Tenth International Conference on the Physics of Electronic and Atomic Collisions, Abstracts of Papers (Paris, France, 1977), p. 552.

146. D. H. Winicur, J. L. Fraites, and J. Bentley, J. Chem. Phys., 64, 1724 (1976).

147. L. G. Piper, D. W. Setser, and M. A. A. Clyne, J. Chem. Phys., 63, 5018 (1975).

148. D. H. Winicur, J. L. Fraites and F. A. Stackhouse, Chem. Phys. Lett., 23, 123 (1973).

149. D. H. Winicur and J. L. Fraites, J. Chem. Phys., 61, 1548 (1974).

150. D. H. Winicur and J. L. Fraites, J. Chem. Phys., 64, 89 (1976).

151. A. L. Schmeltekopf and F. C. Fehsenfeld, J. Chem. Phys., 53, 3173 (1970).

152. P. Oesterlin, H. Haberland, and K. Schmidt, Tenth International Conference on the Physics of Electronic and Atomic Collisions, Abstracts of Papers (Paris, France, 1977), p. 558. Data presented are contaminated by contributions from $He^*(2^1S)$. Further work is in progress.

153. W. Lee and R. M. Martin, J. Chem. Phys., 63, 962 (1975).

154. A. N. Schweid, M. A. D. Fluendy, and E. E. Muschlitz, Jr., Chem. Phys. Lett., 42, 103 (1976).

155. R. A. Sanders, A. N. Schweid, M. Weiss, and E. E. Muschlitz, Jr., J. Chem. Phys., 65, 2700 (1976).

156. J. Krenos and J. Bel Bruno, J. Chem. Phys., 65, 5019 (1976); erratum ibid, 66, 5832 (1977).

157. M. E. Gersh and E. E. Muschlitz, Jr., J. Chem. Phys., 59, 3538 (1973).

158. L. G. Piper, D. W. Setser, and M. A. A. Clyne, J. Chem. Phys., 63, 5018 (1975).

159. D. L. King, L. G. Piper, and D. W. Setser, J. Chem. Soc. Faraday Trans. II, 73, 177 (1977).

160. M. L. Ginter, J. Chem. Phys., 42, 561 (1965); M. L. Ginter, C. M. Brown, ibid., 56, 672 (1972).

161. G. Das, Phys. Rev. A, 11, 732 (1975).

162. A. P. Hickman and N. F. Lane, Phys. Rev. A, 10, 444 (1974).

163. I. Ya. Fugol', Soviet Physics Uspekhi, 12, 182 (1969).

FIGURE CAPTIONS

Fig. 1. Graphic display of atomic properties of the metastable noble gases. The solid lines correspond to the metastables, dashed to the analogous alkali atom (e.g., He* corresponds to Li, etc.). -o-, excitation energies; -□-, ionization potentials; -Δ-, polarizabilities, with the angular momentum substates of the metastables shown separately (see Table I for values).

Fig. 2. Schematic of the experimental setup.

Fig. 3. Newton diagrams for the two sets of measurements shown in Figs. 4 and 5. On the left, the He* beam source is cooled to liquid nitrogen temperature and the ground-state He beam is at room temperature, while on the right the beam temperatures are interchanged. This gives the same c.m. kinetic energy but different LAB energies for the scattered atoms.

Fig. 4. He$^*(2^3S)$ + He laboratory angular distributions at the same c.m. energy for (A) cold excited beam and (B) cold ground state beam. The relative intensities differ because of the velocity dependence of the intensity transformation Jacobian.

Fig. 5. Center-of-mass angular distributions derived from the data of Fig. 4. The results are identical within experimental error, showing the velocity independence of detection efficiency in the 17 to 86 meV energy range.

Fig. 6. Central part of the Freiburg apparatus.

Fig. 7. Time-of-flight distributions of metastable He beams. The singlet distributions are generally narrower than the triplet ones. The 540 meV distribution was obtained with the plasma jet source (see Section III.A.6).

Fig. 8. Angular distribution for He$^*(2^3S)$ + He showing a sharp 90° peak partially caused by photoexcitation of the crossed beam.

Fig. 9. Laboratory angular distributions for Ne* and Ar* + He. Solid points are experimental; solid and dashed curves are calculated from potentials of Fig. 10.

Fig. 10. Interatomic potentials for (a) Ne* + He and (b) Ar* + He derived from fitting the data of Fig. 8. Vertical lines show the range of internuclear distance probed at each energy E_i, with $E_1 < E_2$ as given in Fig. 9.

Fig. 11. Potentials for He$_2$. Figs. 14 and 17 show the long range parts of the excited-state curves in greater detail.

Fig. 12. Classical picture of direct and exchange scattering.

Fig. 13. Laboratory differential cross sections for He$^*(2^1S)$ + He at six kinetic energies.

Fig. 15. Difference between calculated and experimental potentials for the first excited $^1\Sigma$ states of the He$_2$ molecule. Within experimental error the two curves are identical for $r > 3$ Å.

Fig. 14. Potentials for $He^{*}(2^{1}S)$ + He derived from the data of Fig. 13. The apparent discontinuity at 50 meV results from the change of ordinate scale. The dashed lines are the GVB _ab initio_ results of Ref. 84. Collision energies are given at the right. The potentials are tabulated in Table III.

Fig. 16. Laboratory differential cross sections for $He^{*}(2^{3}S)$ + He at six kinetic energies.

Fig. 17. Potentials for $He^{*}(2^{3}S)$ + He derived from the data of Fig. 16. The dashed lines are derived from analysis of spin-exchange experiments, while the points are taken from an _ab initio_ calculation. The potentials are tabulated in Table IV .

Fig. 18. Hyperthermal energy differential cross sections for $He^{*}(2^{3}S)$ + He, obtained with a plasma He^{*} source.

Fig. 19. Reduced-variable plot of $He^{*}(2^{3}S)$ + He differential cross sections, obtained with a charge-exchange He^{*} source.

Fig. 20. Energy dependence of the total cross section for $He^{*}(2^{1}S)$ + He calculated from the potentials of Fig. 14 and Table III.

Oscillations at low energies due to the nuclear-symmetry glory effect are amplified in curve I, in which the difference between cross sections for identical and distinguishable particles is plotted on an expanded scale.

Fig. 21. Energy dependence of the total cross section for $He^{*}(2^{3}S)$ + He calculated from the potentials of Fig. 17 and Table IV. Data points represent the measurements of Trujillo, Ref. 95. Format as in Fig. 20.

Fig. 22. Energy dependence of the excitation transfer cross section for $^{3}He^{*}(2^{3}S) + {}^{3}He$, calculated from the potentials of Fig. 17 and Table IV.

Fig. 23. Temperature dependence of the rate constant for excitation transfer in $^{3}He^{*}(2^{3}S) + {}^{3}He$, calculated from the potentials of Fig. 17 and Table IV. Data are derived from analysis of optical pumping experiments.

Fig. 24. Calculations for $He^{*}(2^{1}S)$ + He assuming distinguishable particles compared to experiment.

Fig. 25. Quantal deflection functions for $He^{*}(2^{1}S)$ + He at 42 meV. The small splitting at large ℓ causes damping of the symmetry oscillations.

Fig. 26. Quantal deflection functions at higher energies for $He^{*}(2^{1}S)$ + He. The orbiting spikes result from trajectories which spiral into the inner minimum of the _ungerade_ potential.

Fig. 27. Calculations for $He^{*}(2^{1}S)$ + He from the ungerade potential only compared to experiment. The classical rainbow angles are indicated by the vertical arrows.

Fig. 28. Typical deflection functions for energies above the ungerade barrier. The dashed lines give the contributions from exchange scattering.

Fig. 29. Laboratory angular distributions for $He^*(2^1S, 2^3S) + Ar$ at 66 meV. The relative intensities of singlet and triplet are as measured.

Fig. 30. Laboratory angular distributions for $He^*(2^1S) + Ar$ at six collision energies from the Freiburg laboratory. Solid curves are calculated from optical potential of Ref. 102 (see Figs. 32 and 35).

Fig. 31. Laboratory angular distributions for $He^*(2^1S) + Ar$ at five collision energies from the Pittsburgh laboratory. Solid curves are calculated from the optical potential of Ref. 109 (see Figs. 32 and 35).

Fig. 32. Comparison of potentials for $He^*(2^1S) + Ar$ (real part) derived by the Freiburg (a) and Pittsburgh (b) groups.

Fig. 33. Laboratory angular distributions for $He^*(2^3S) + Ar$ at eight collision energies. Solid curves are calculated from optical potential of Ref. 100 (see Fig. 34).

Fig. 34. Optical potential for $He^*(2^3S) + Ar$, from Ref. 100; see footnote 115.

Fig. 35. Resonance widths $\Gamma(r)$ for $He^* + Ar$ derived from differential scattering. Γ_S^a, singlet, Ref. 102; Γ_S^b, singlet, Ref. 109; Γ_T, triplet, Ref. 100.

Fig. 36. Potentials for $He^* + D_2$, Ar and Kr from Ref. 104. Dotted and chain curves for $He^* + D_2$ are <u>ab initio</u> results.

Fig. 37. Potentials for $He^*(2^1S) + Ar$, Kr and Xe (real part), from Ref. 109.

Fig. 38. Center-of-mass angular distributions for scattering of $Ne^*(^3P_{2,0})$ by Ar, Kr and Xe.

Fig. 39. Penning ion angular distributions for $He^*(2^1S) + Ar$.

Fig. 40. Approximate center-of-mass Penning ion angular distributions for $He^*(2^1S) + Ar$.

Fig. 41. Penning ion angular distributions for $He^*(2^1S) + H_2$ and O_2.

Fig. 42. Penning ion angular distributions for $He^*(2^1S) + CH_4$ and CO_2.

Fig. 43. CH_3^+ fragment ion angular distribution from $He^*(2^1S) + CH_4$ compared with quasiequilibrium theory (QET).

Fig. 44. Penning ion angular distribution for $Ne^* + Ar$.

Fig. 45. Velocity dependence of the total cross section for $He^*(2^3S) + Ar$. Solid curve is calculated from the potential of Ref. 100, points are measurements of Trujillo, Ref. 136. Orbiting resonances are indicated by (v,J) quantum numbers.

Fig. 46. Velocity dependence of the total ionization cross section for $He^*(2^3S)$ + Ar. Solid curve is calculated from optical potential of Ref. 100, with energies of the differential experiments shown by dots. Other symbols represent the measurements of Refs. 139, 140 and 142 (see text). The chain curve is a "close collision" cross section, while the spikes result from orbiting resonances labeled by (v,J).

Fig. 47. Velocity dependence of the total ionization cross section for $He^*(2^1S)$ + Ar. Curves are calculated from optical potentials of Ref. 102 and 108, while symbols represent the measurements of Ref. 139, 140 and 142.

Fig. 48. Temperature dependence of the total quenching rate constant for He^* + Ar. Solid curves are measurements of Ref. 141, while dashed curves are calculated from optical potentials of Ref. 100 and 102.

Fig. 49. Low energy laboratory angular distribution for $He^*(2^1S)$ + Ne. Solid curve is a fit for an assumed single-channel real potential.

Fig. 50. Laboratory angular distribution for $He^*(2^1S)$ + Ne. Circles are total angular distribution, diamonds are time-of-flight corrected for Ne^* contribution. Solid curve is calculated by fitting a single-channel potential to small angles.

Fig. 51. Laboratory angular distribution for Ar^* + Kr. Diamonds are time-of-flight corrected for Kr^* contributions. Solid curve is calculated from a K + Kr potential.

Fig. 52. Ne^* laboratory angular distributions from $He^*(2^1S)$ + Ne at five collision energies.

Fig. 53. Newton diagram for $He^*(2^1S)$ + Ne at 66 meV. The largest partial circle is the locus of He^* velocities from elastic collisions, the smaller numbered ones for inelastic production of Ne^* in various final states. Numbers n correspond to subscripts $3s_n$ for the states of Ne (Paschen notation). Angular rays correspond to positions of maxima or shoulders in the angular distribution of Fig. 50.

Fig. 54. Sampling of time-of-flight spectra for He^* + Ne. $\underline{t_0}$ is the flight time from beam excitation region to collision center, $\underline{e}$ the expected elastic flight time derived from the Newton diagram of Fig. 53, and the numbered times those for Ne^* in various final states, notation as in Fig. 53. Number zero corresponds to beam neon photoexcited by far-uv photons produced as a result of energy transfer (see Section III.A.7).

Fig. 55. Ne^* angular distribution from $He^*(2^1S)$ + Ne, derived from the data of Fig. 50.

Fig. 56. Angular distributions of Kr^* and Xe^* for excitation transfer from Ar^*. State assignments are derived from time-of-flight measurements.

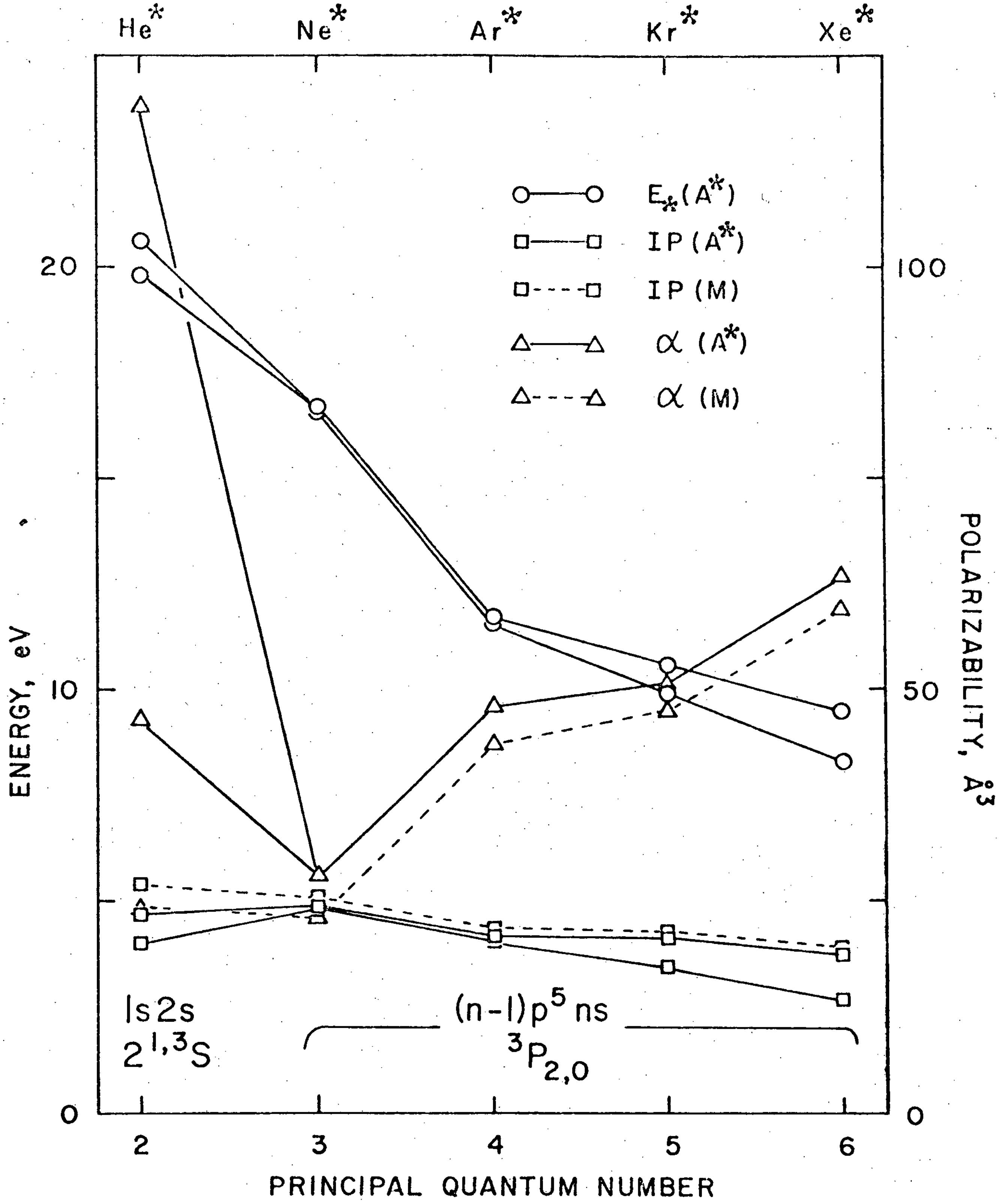
He*
Ne*
Ar*
Kr*
Xe*
$E_*(A^*)$
IP (A^*)
IP (M)
α (A^*)
α (M)
20
10
0
100
50
0
ENERGY, eV
POLARIZABILITY, Å^3
1s2s
$2^{1,3}S$
$(n-1)p^5 ns$
$^3P_{2,0}$
2
3
4
5
6
PRINCIPAL QUANTUM NUMBER

Fig. 1

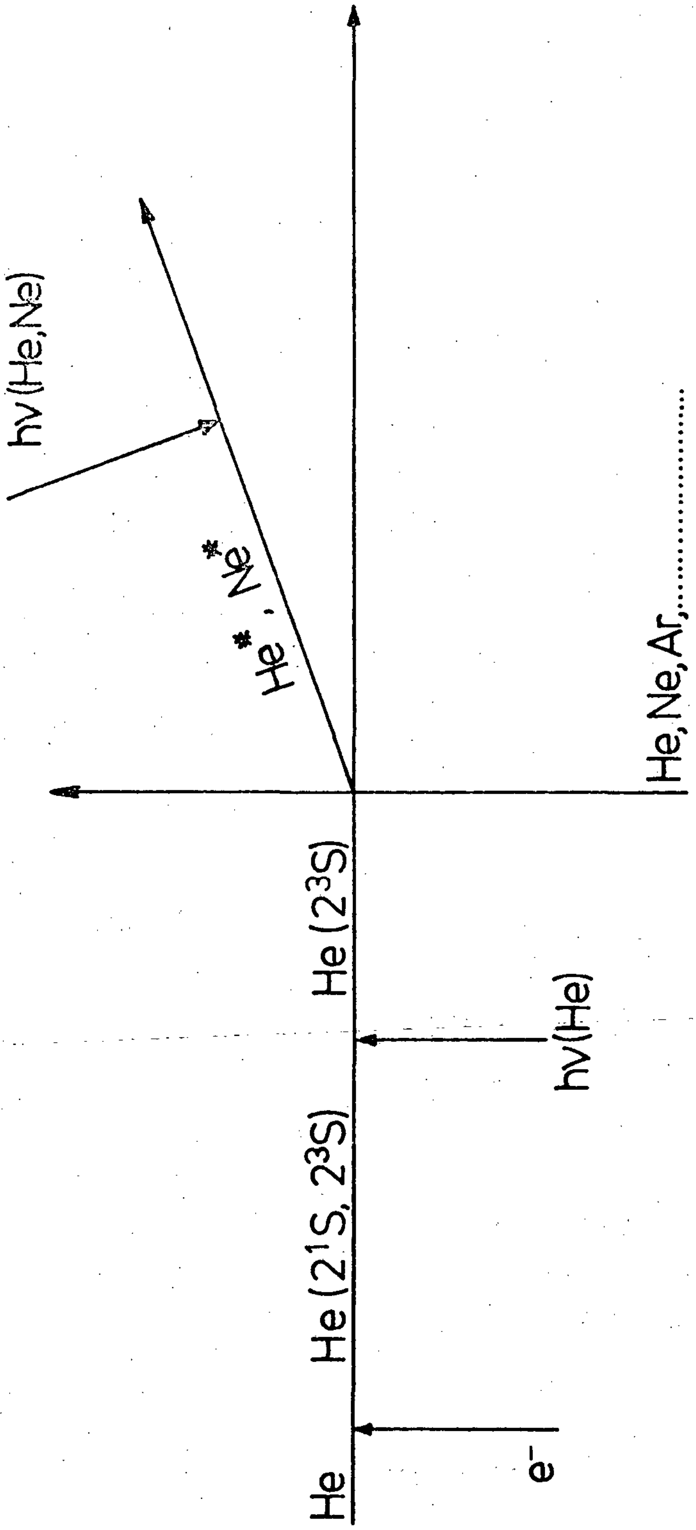

XBL 793-8778

Fig. 2

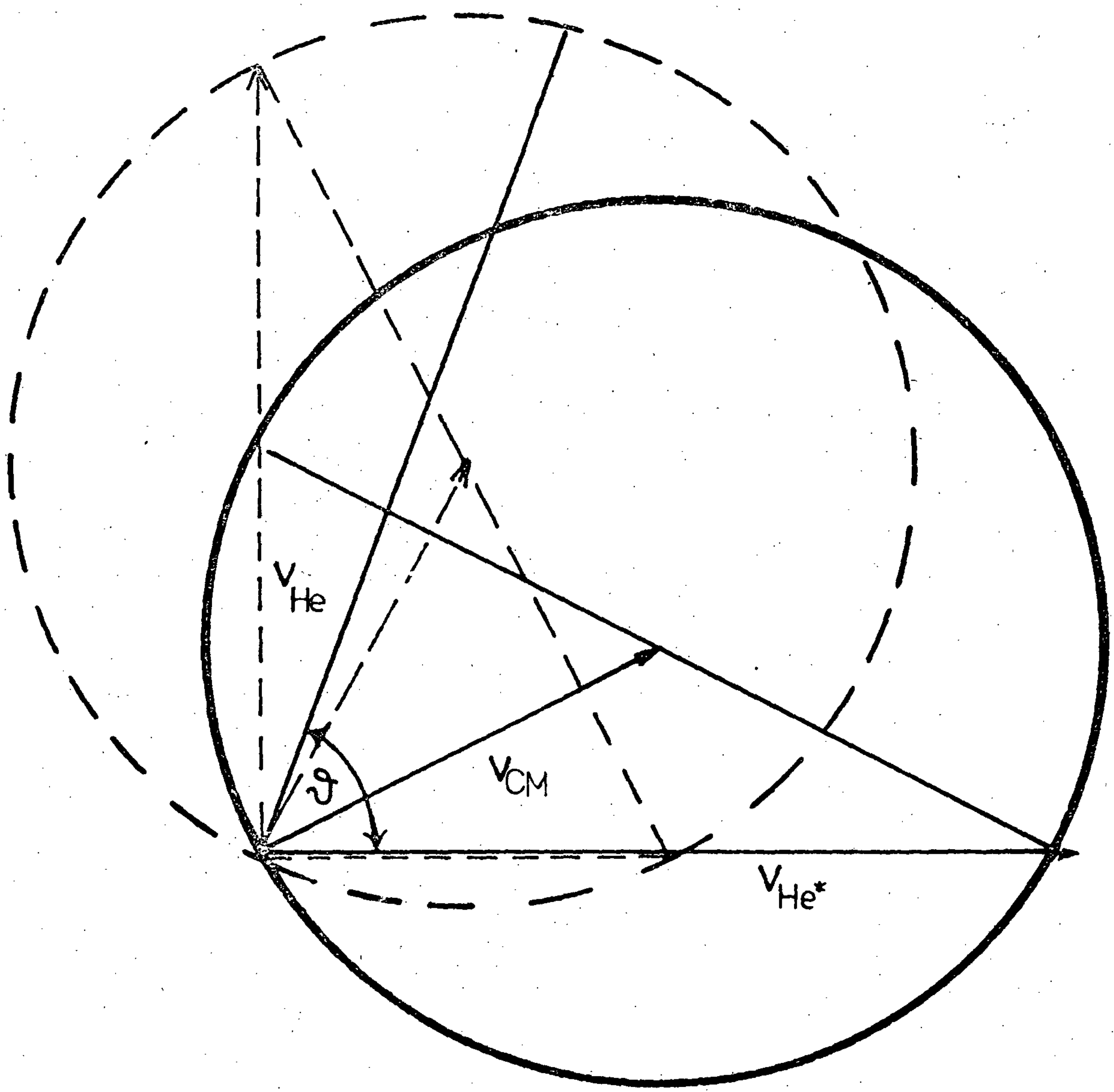

Fig. 3

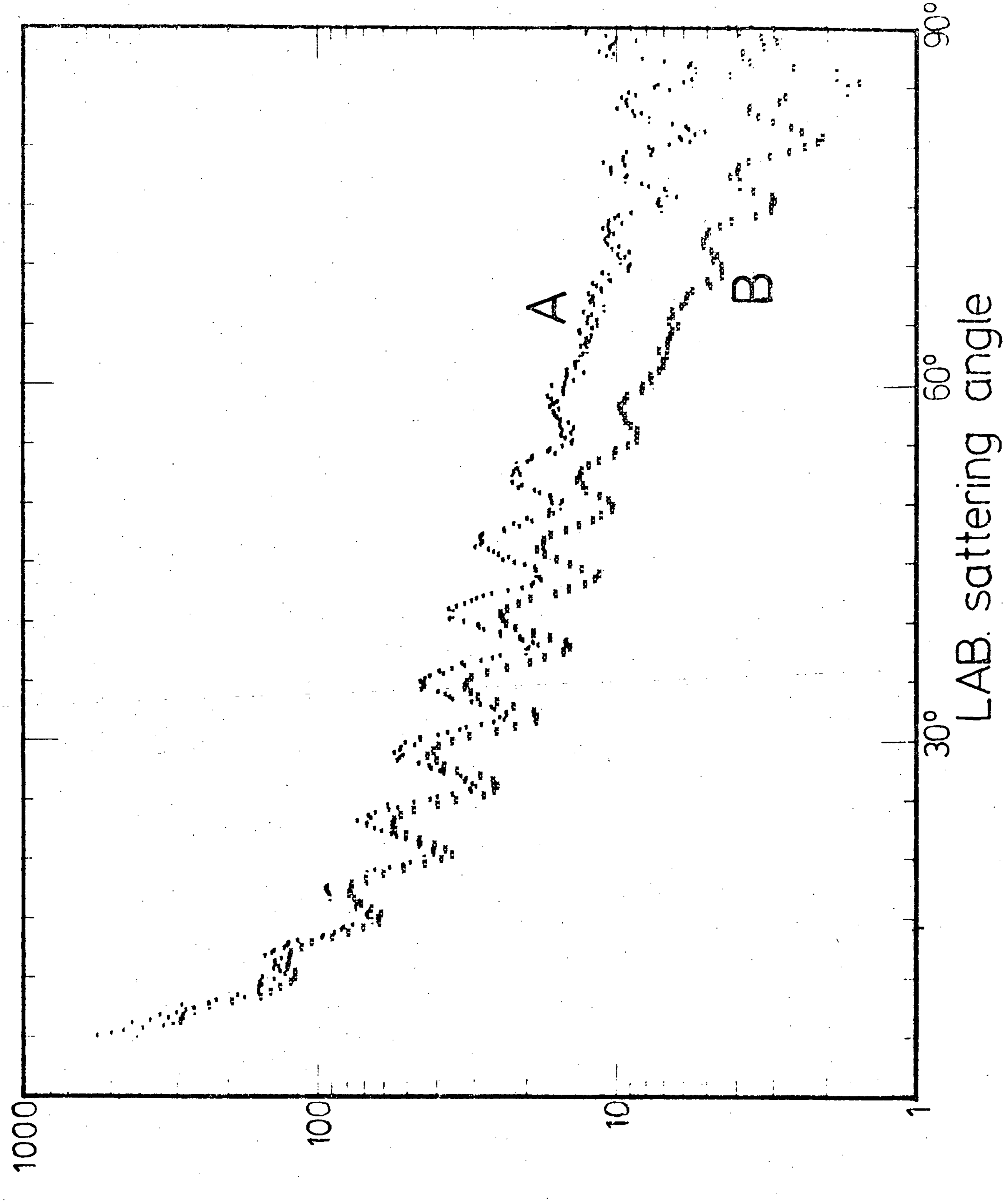

Fig. 4.

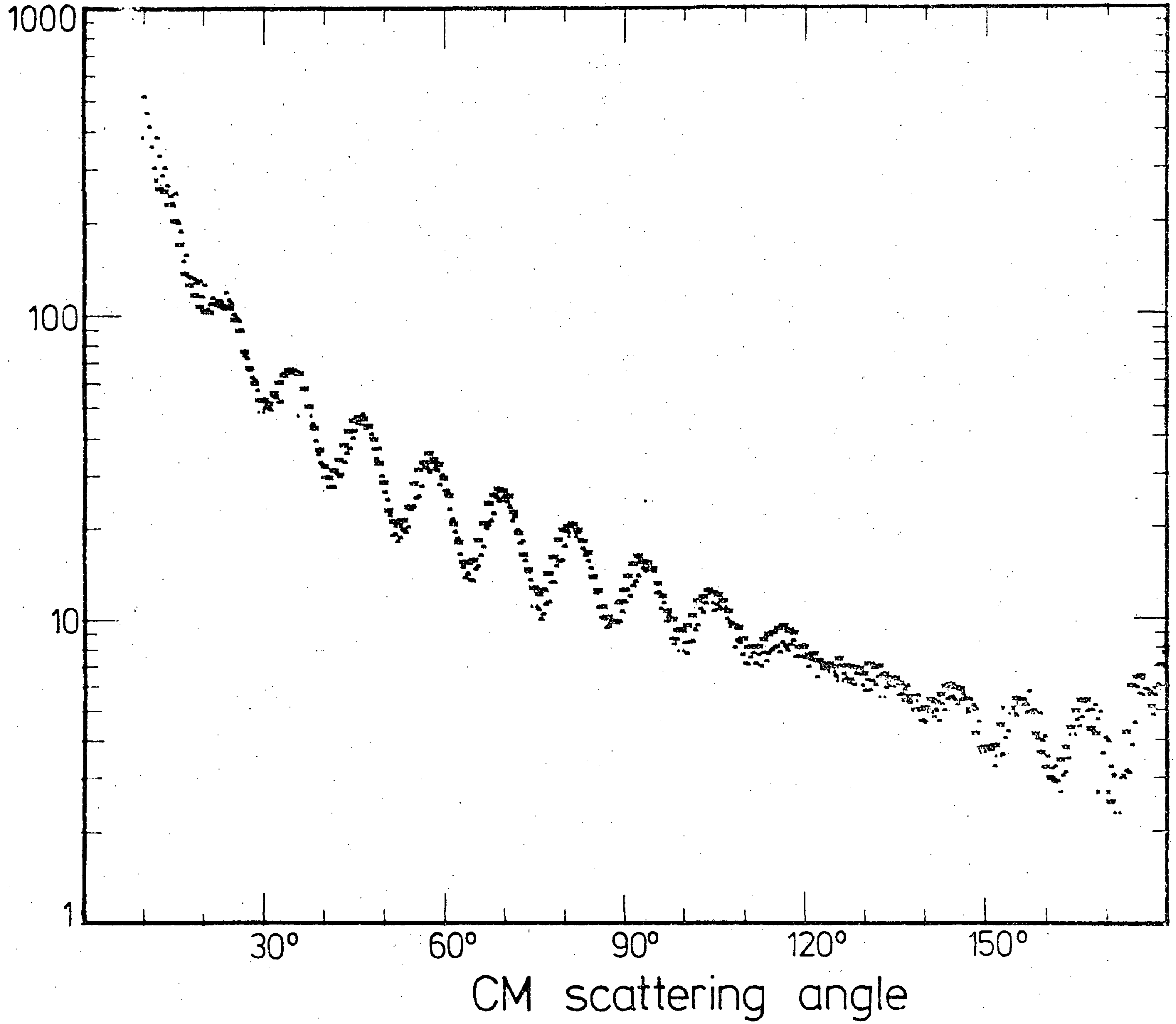

Fig. 5

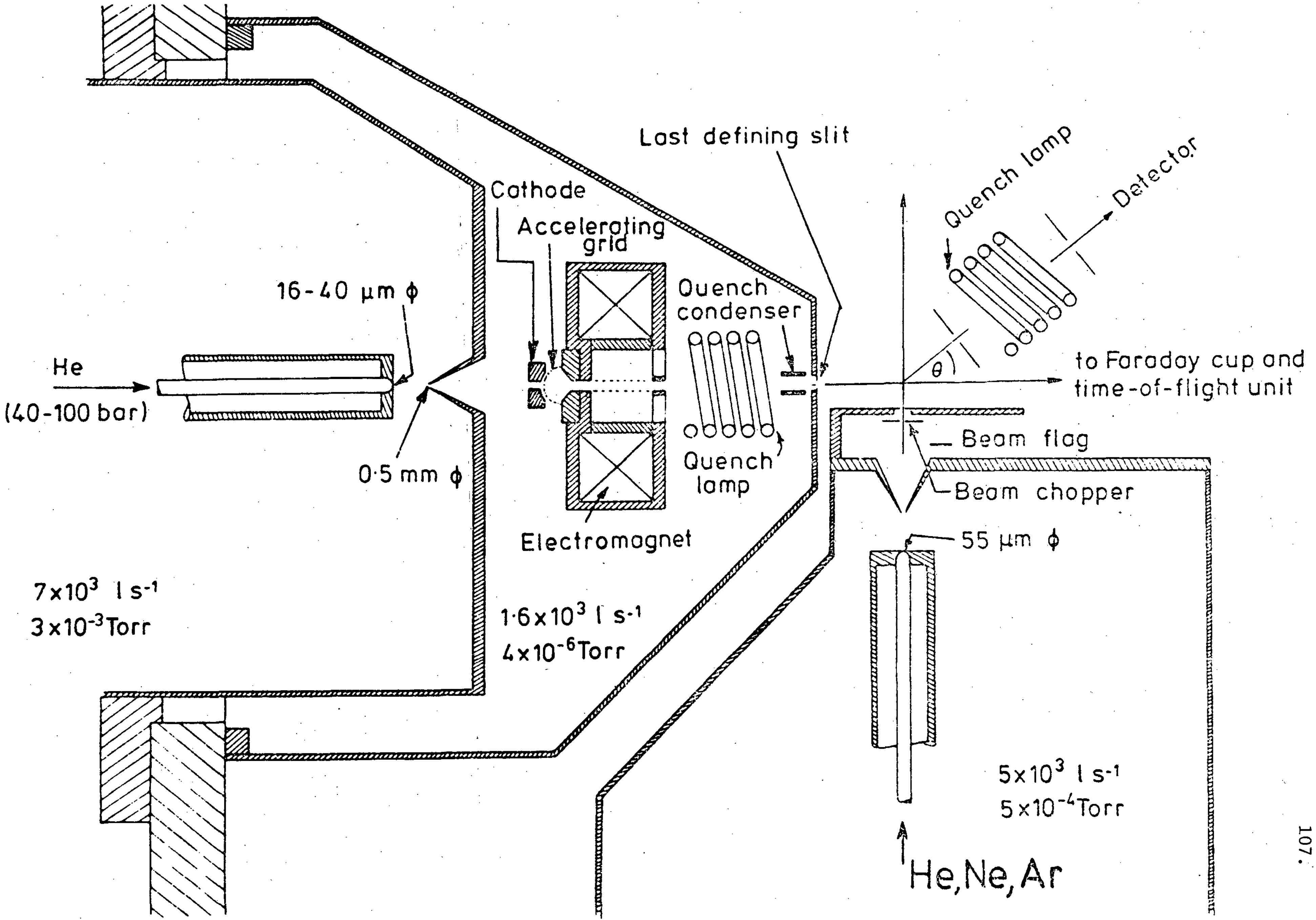

Last defining slit
Quench lamp
Detector
Cathode
Accelerating grid
Quench condenser
16-40 µm ϕ
He
(40-100 bar)
0·5 mm ϕ
Quench lamp
Electromagnet
θ
to Faraday cup and time-of-flight unit
Beam flag
Beam chopper
55 µm ϕ
7×10³ l s⁻¹
3×10⁻³Torr
1·6×10³ l s⁻¹
4×10⁻⁶Torr
5×10³ l s⁻¹
5×10⁻⁴Torr
He,Ne,Ar

Fig. 6

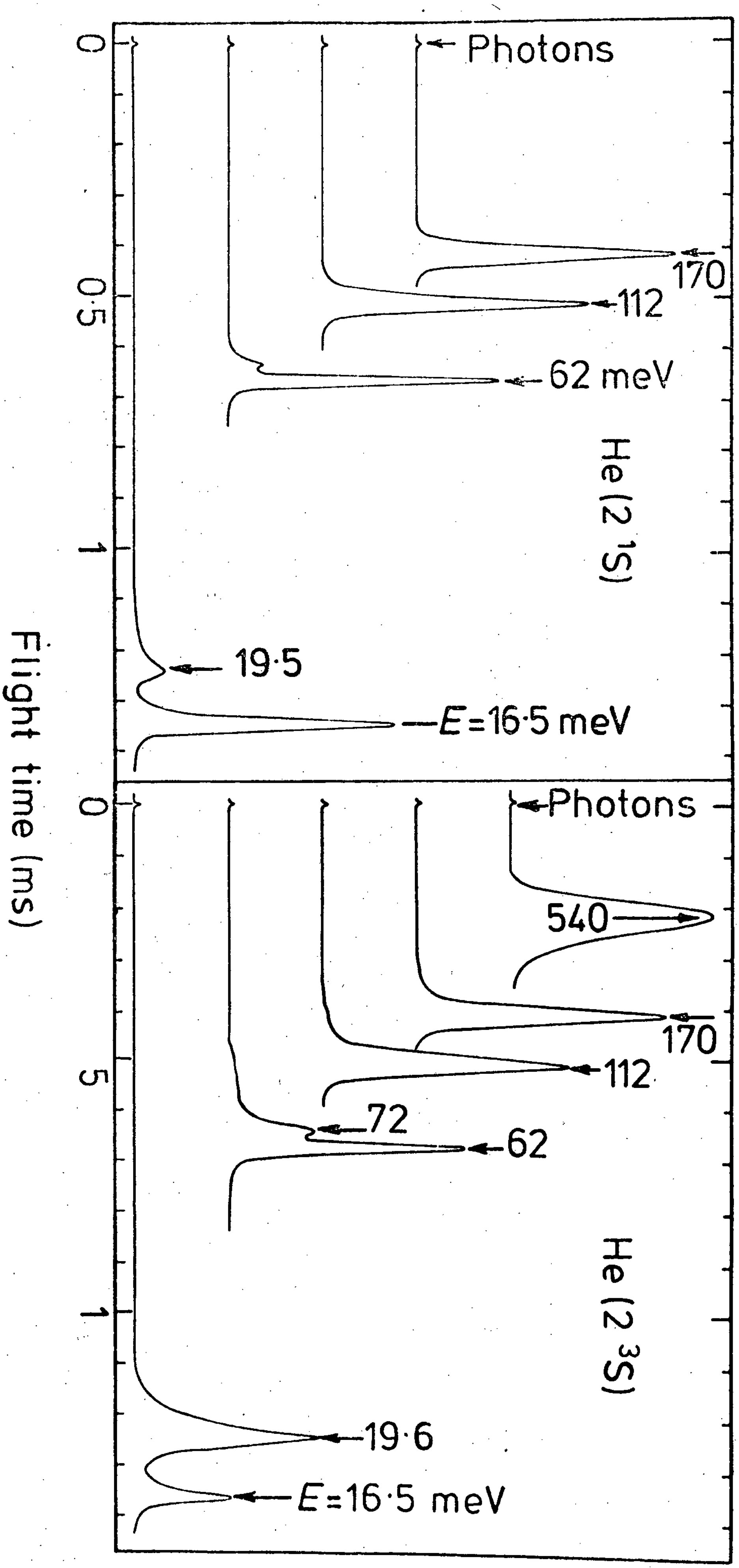
Photons
170
112
62 meV
He (2 ¹S)
19·5
E=16·5 meV
Photons
540
170
112
72
62
He (2 ³S)
19·6
E=16·5 meV
Flight time (ms)
0
0·5
1
0
·5
1

Fig. 7

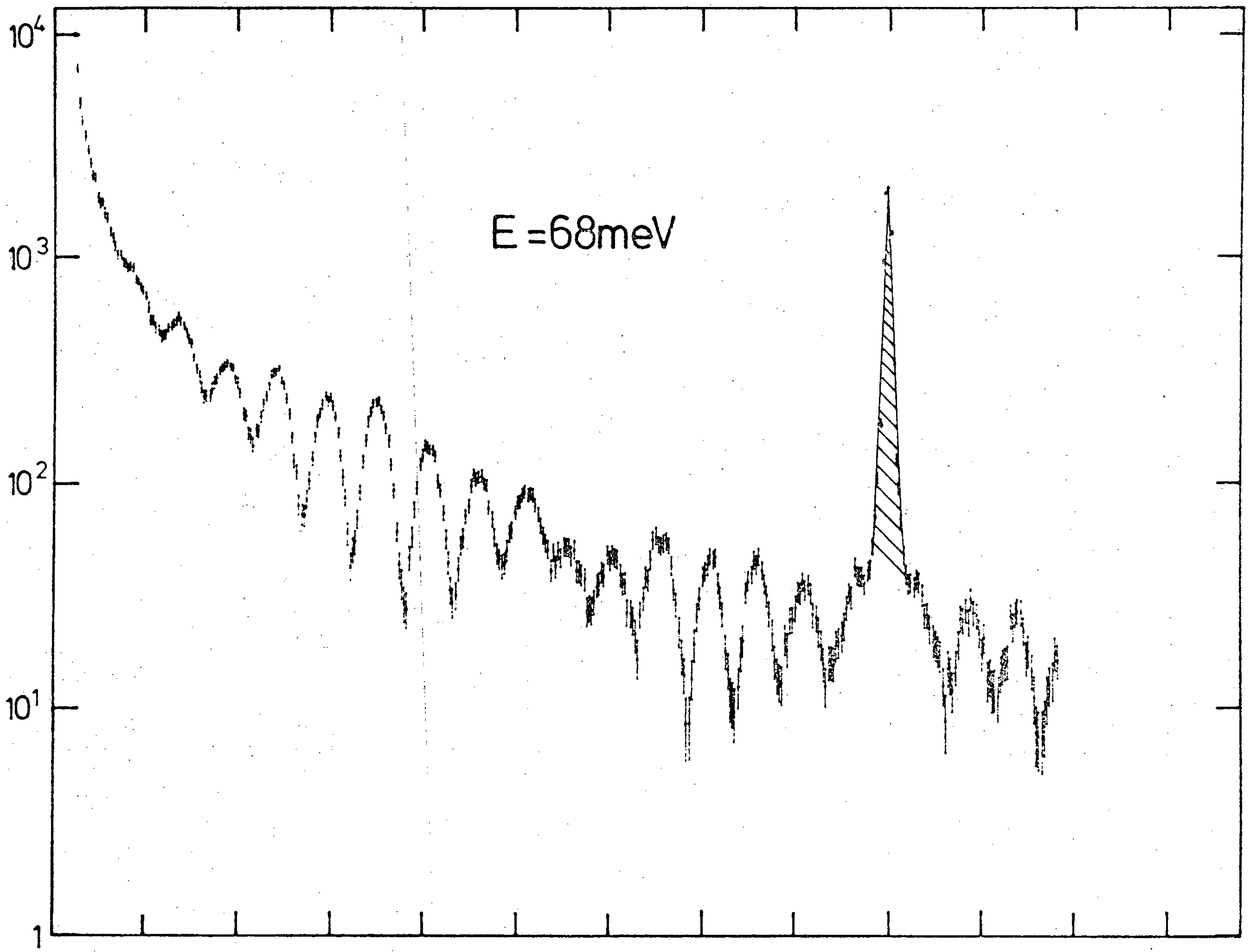

Fig. 8

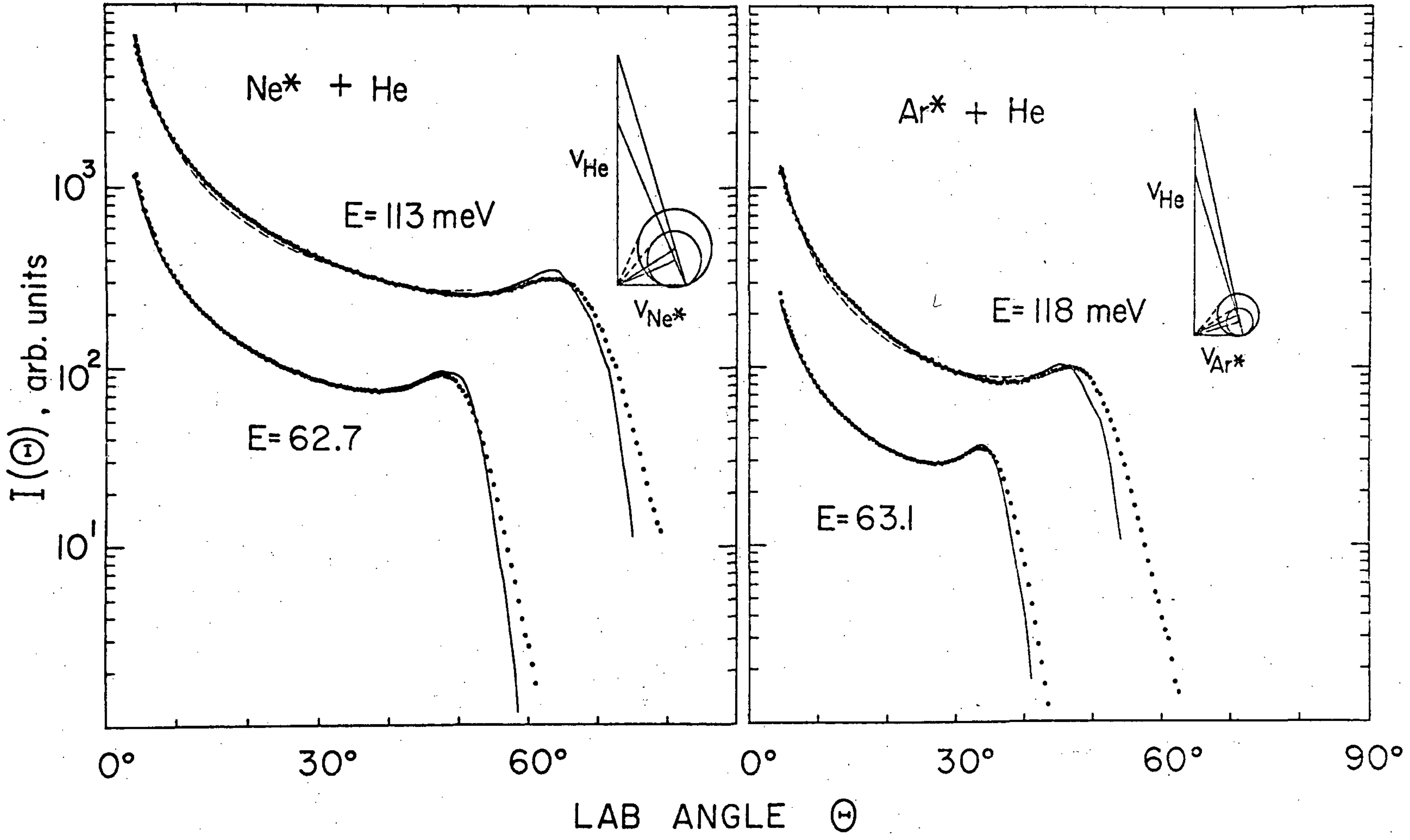
Ne* + He
E= 113 meV
E= 62.7
V_{He}
V_{Ne^*}
Ar* + He
E= 118 meV
E= 63.1
V_{He}
V_{Ar^*}
10^3
10^2
10^1
I(Θ), arb. units
0°
30°
60°
0°
30°
60°
90°
LAB ANGLE Θ

Fig. 9

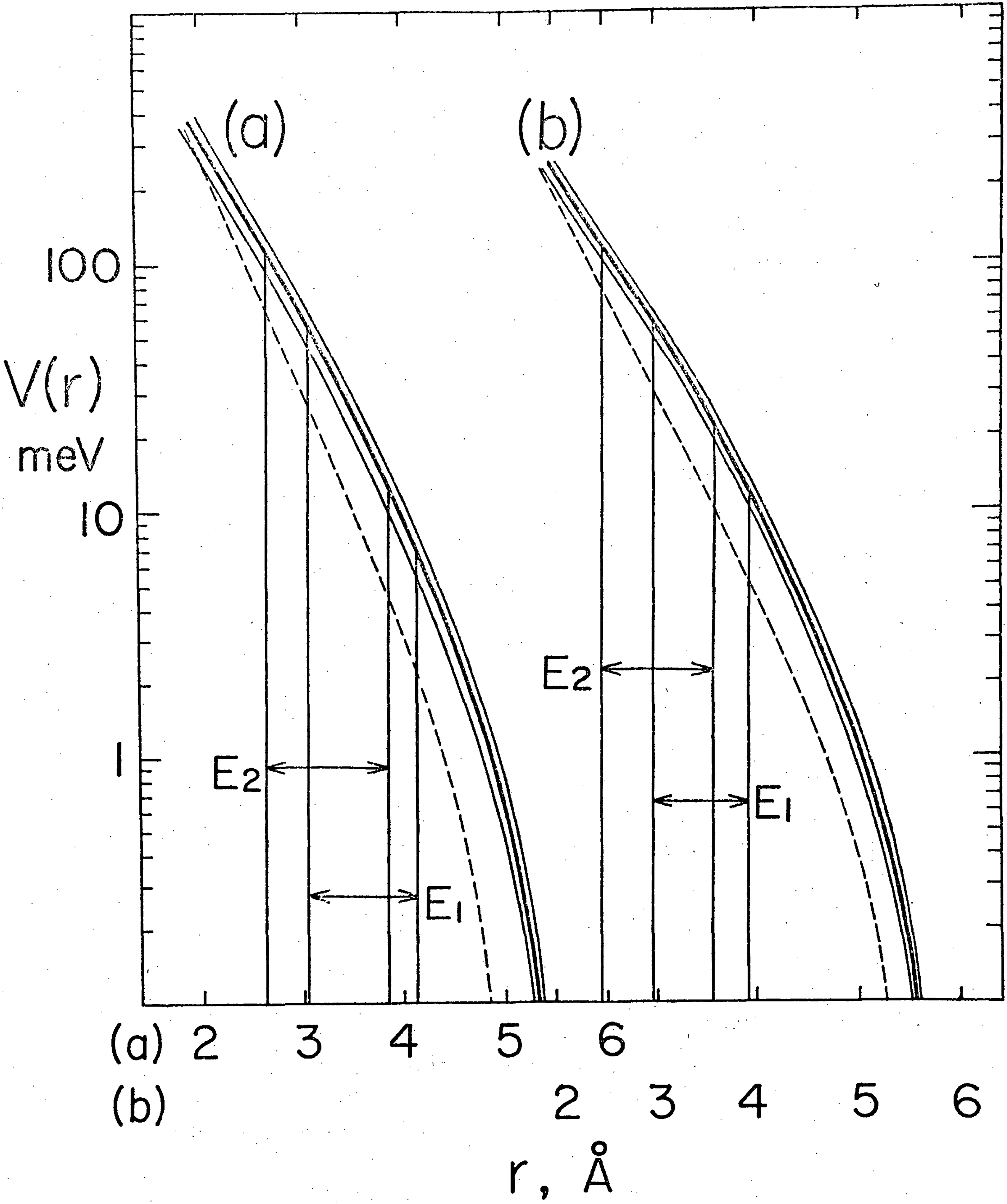

Fig. 10

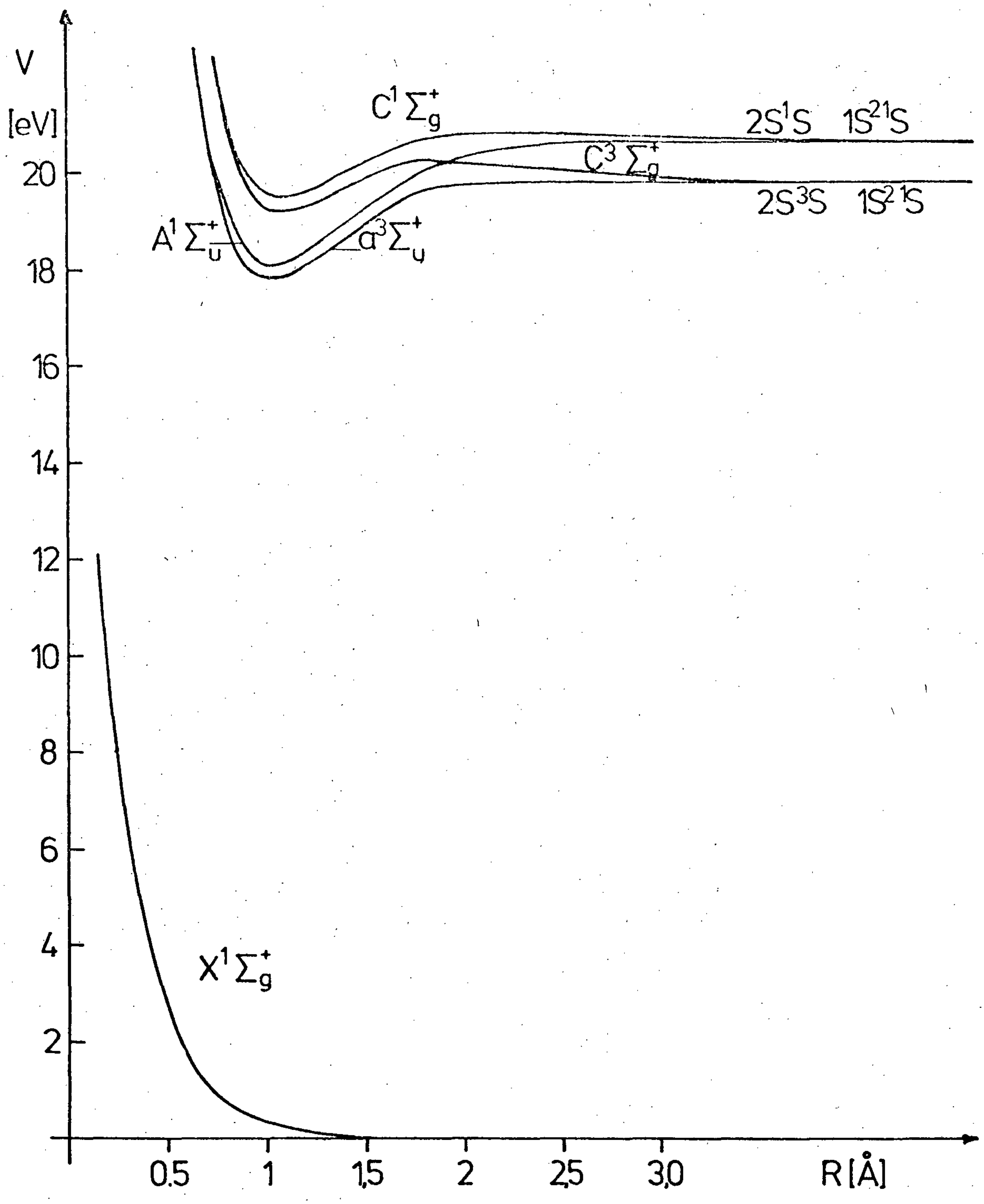

XBL 793-8780

Fig. 11

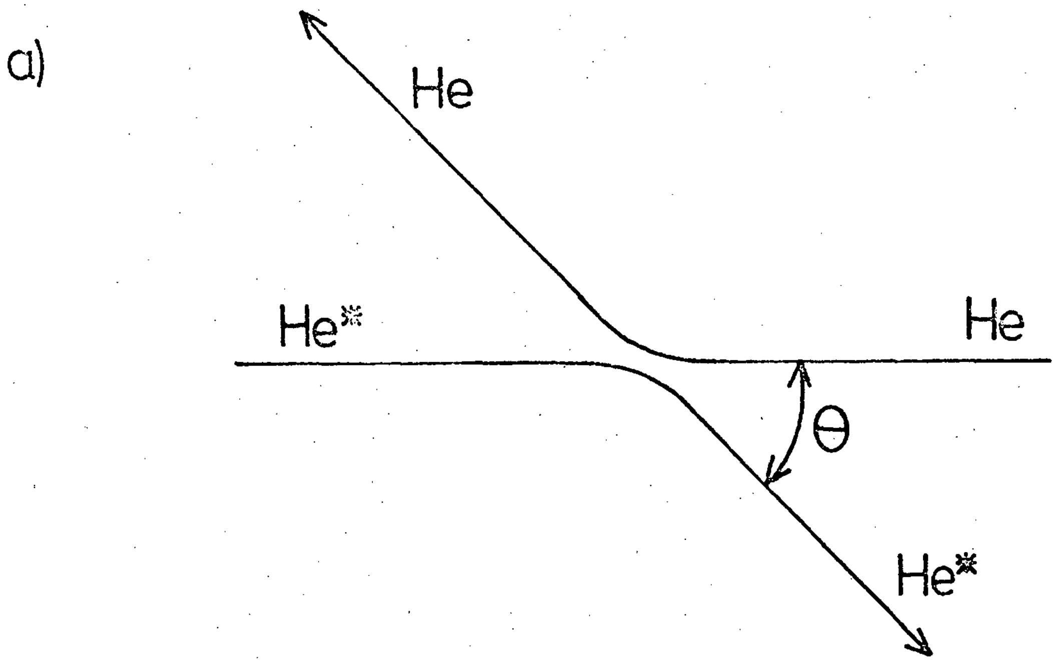

$$f(\text{direkt}) = \frac{1}{2}\left\{f_g(\Theta) + f_u(\Theta)\right\}$$

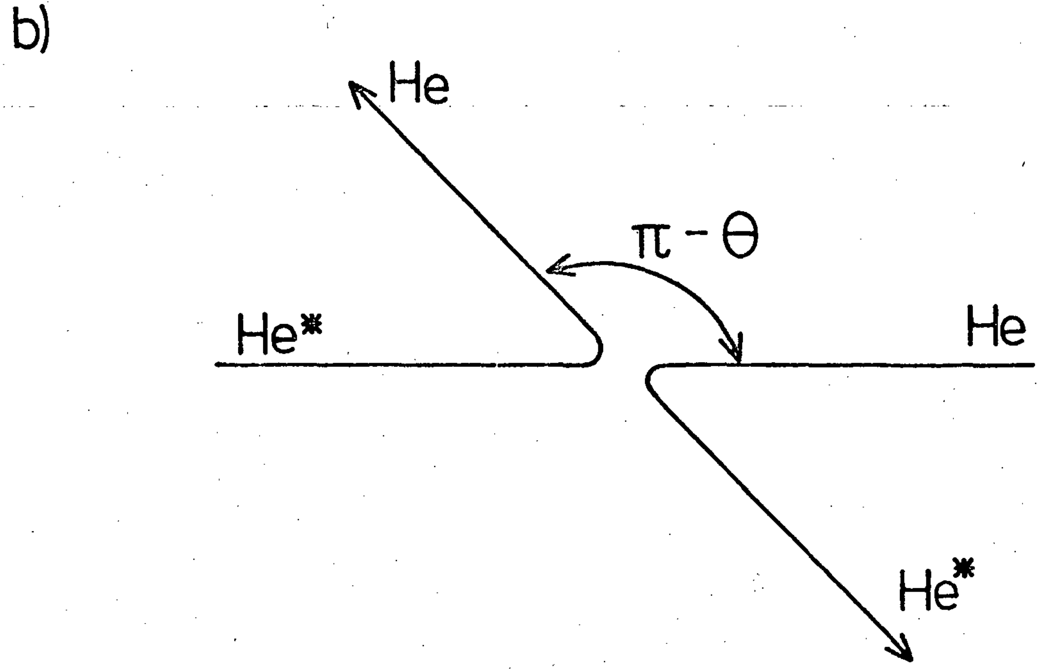

$$f(\text{exchange}) = \frac{1}{2}\left\{f_g(\pi-\Theta) - f_u(\pi-\Theta)\right\}$$

Fig. 12

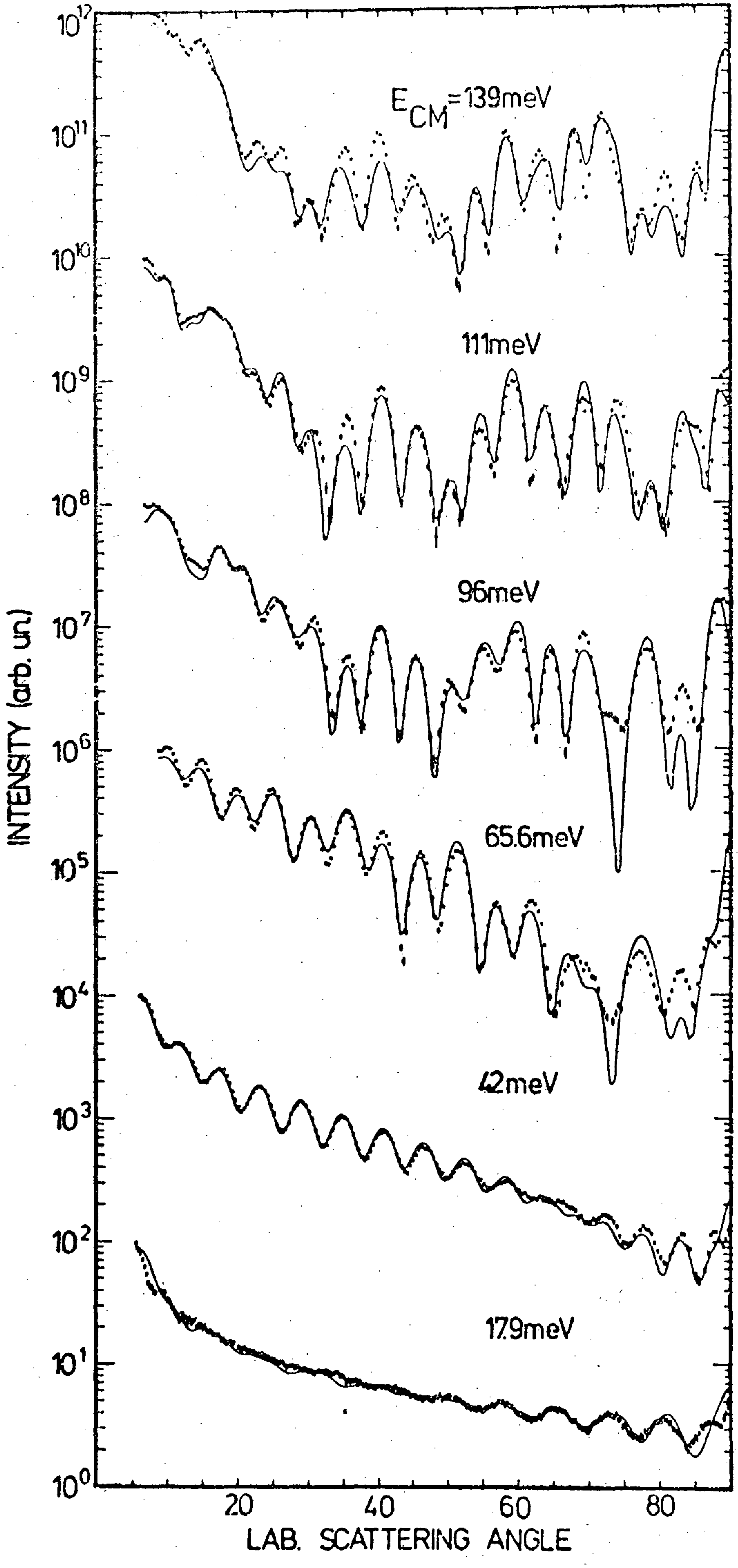
INTENSITY (arb. un.)
LAB. SCATTERING ANGLE
E_{CM}=139meV
111meV
96meV
65.6meV
42meV
17.9meV
10^{0}
10^{1}
10^{2}
10^{3}
10^{4}
10^{5}
10^{6}
10^{7}
10^{8}
10^{9}
10^{10}
10^{11}
10^{12}
20
40
60
80

Fig. 13

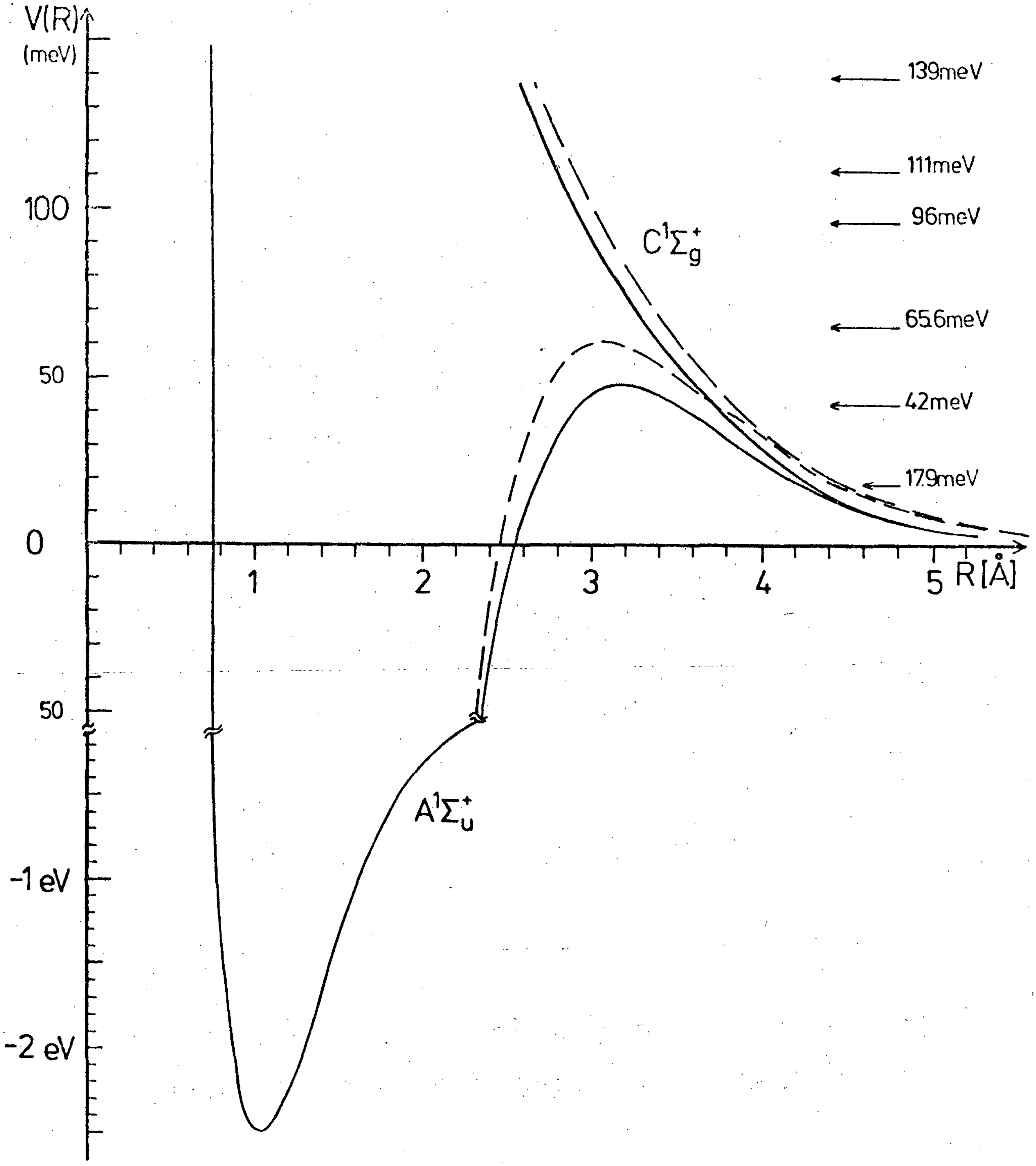
V(R)
(meV)
100
50
0
50
-1 eV
-2 eV
1
2
3
4
5
R [Å]
139meV
111meV
96meV
65.6meV
42meV
17.9meV
$C^1\Sigma_g^+$
$A^1\Sigma_u^+$

Fig. 14

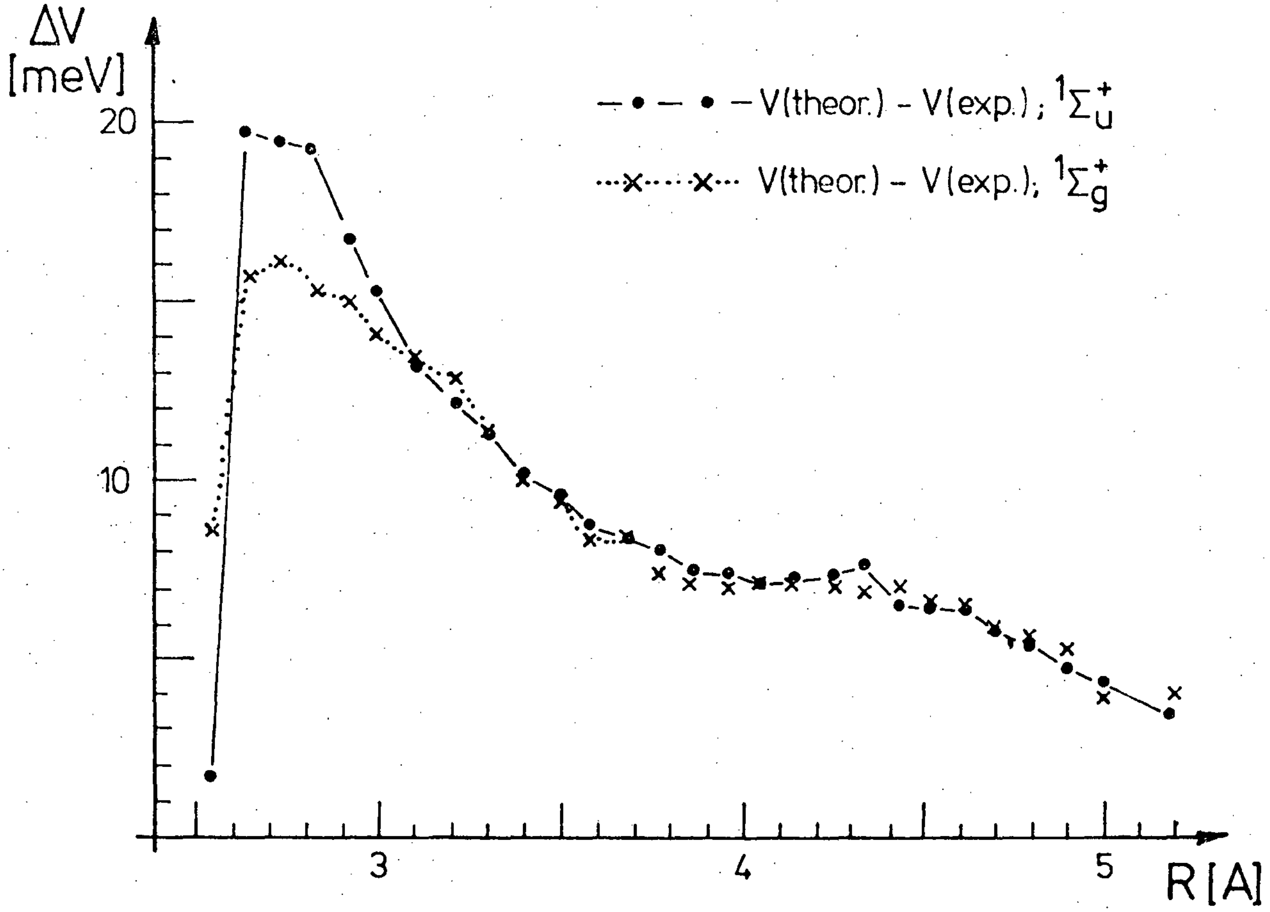

Difference of the calculated and experjmental results for the first excited state of the helium molecule.

Fig. 15

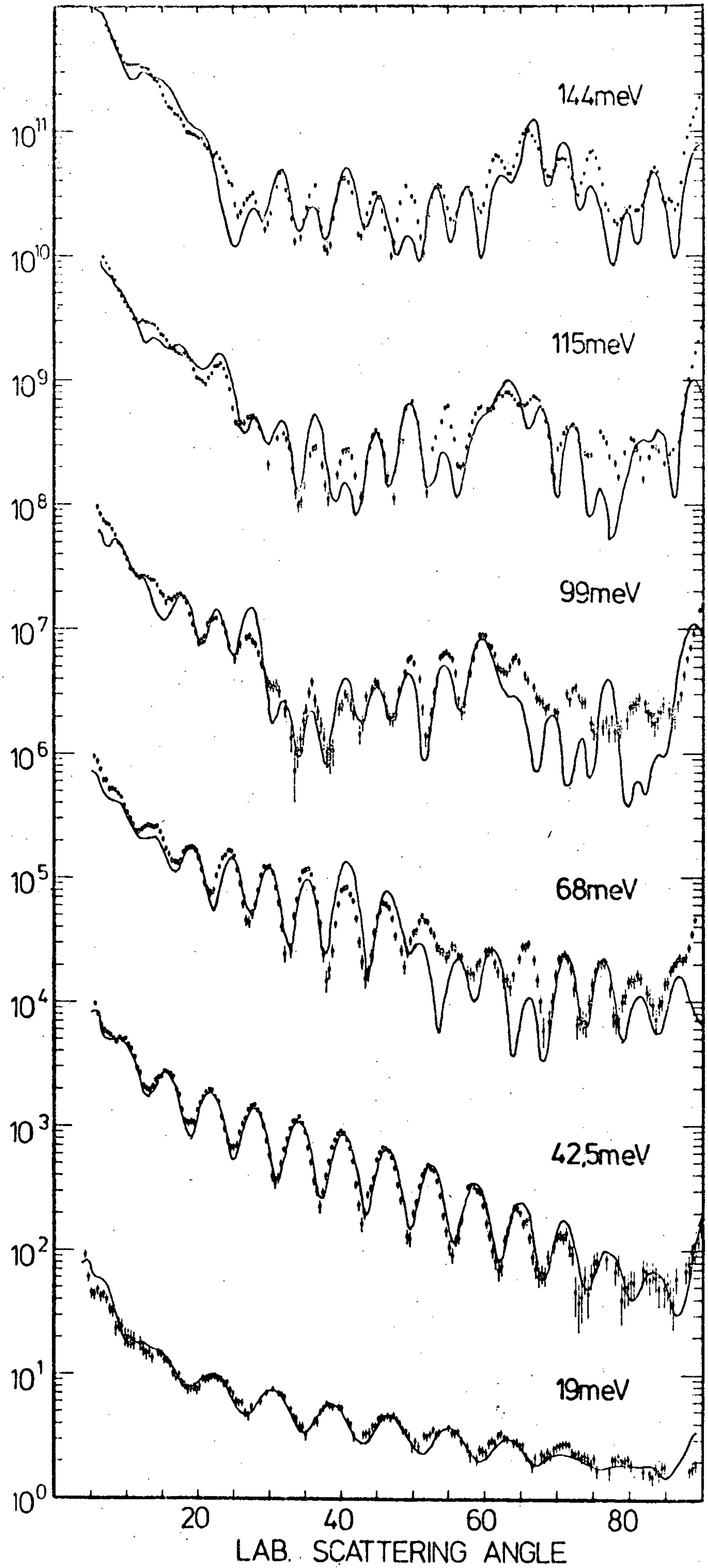
144meV
115meV
99meV
68meV
42,5meV
19meV
10^{11}
10^{10}
10^9
10^8
10^7
10^6
10^5
10^4
10^3
10^2
10^1
10^0
20
40
60
80
LAB. SCATTERING ANGLE

Fig. 16

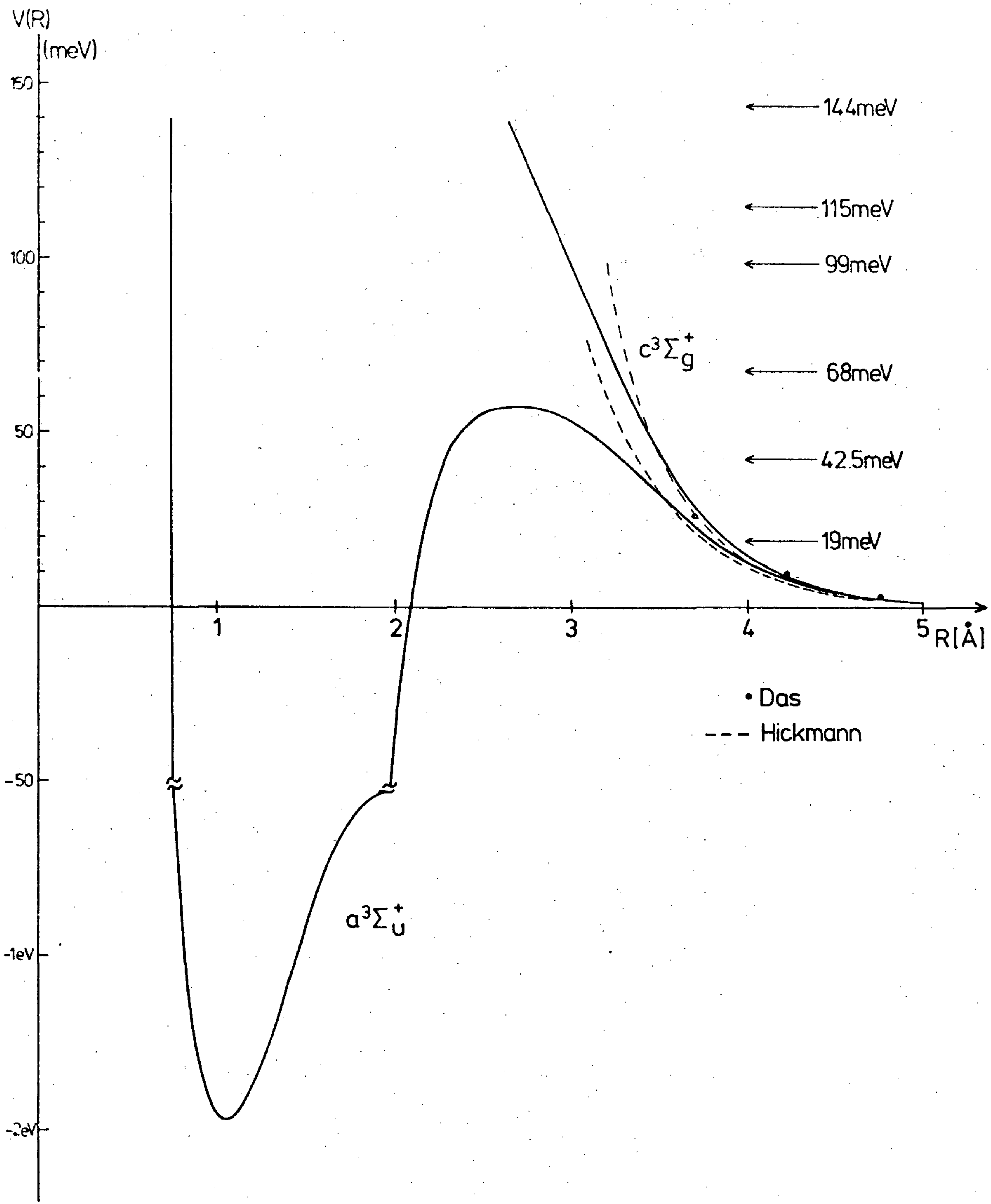
V(R)
(meV)
150
100
50
-50
-1eV
-2eV
1
2
3
4
5
R[Å]
144meV
115meV
99meV
68meV
42.5meV
19meV
$c^3\Sigma_g^+$
$a^3\Sigma_u^+$
• Das
--- Hickmann

Fig. 17

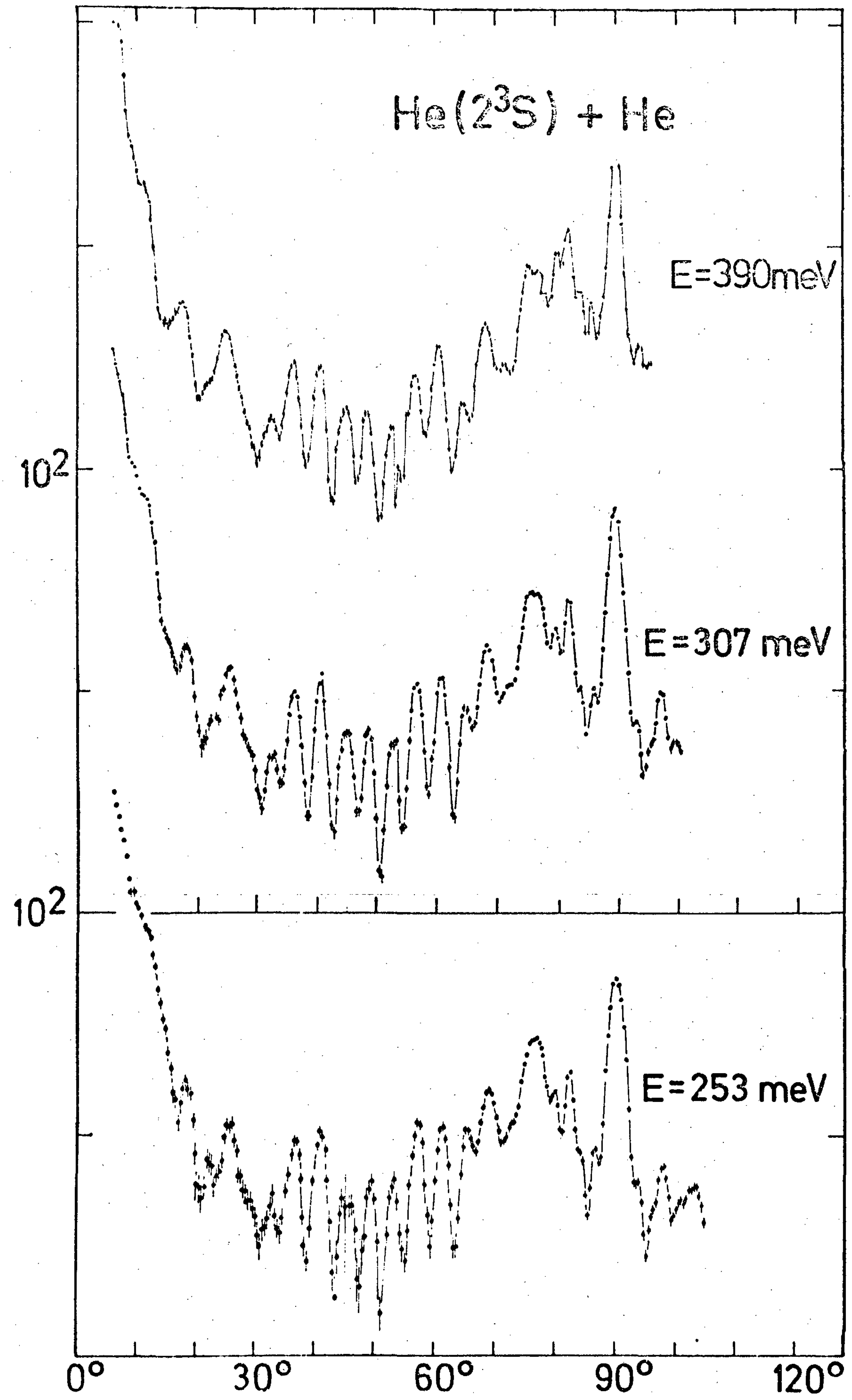
He(2^{3}S) + He
E=390meV
E=307 meV
E=253 meV
10^2
10^2
0°
30°
60°
90°
120°
Laboratory differential Cross section

Fig. 18

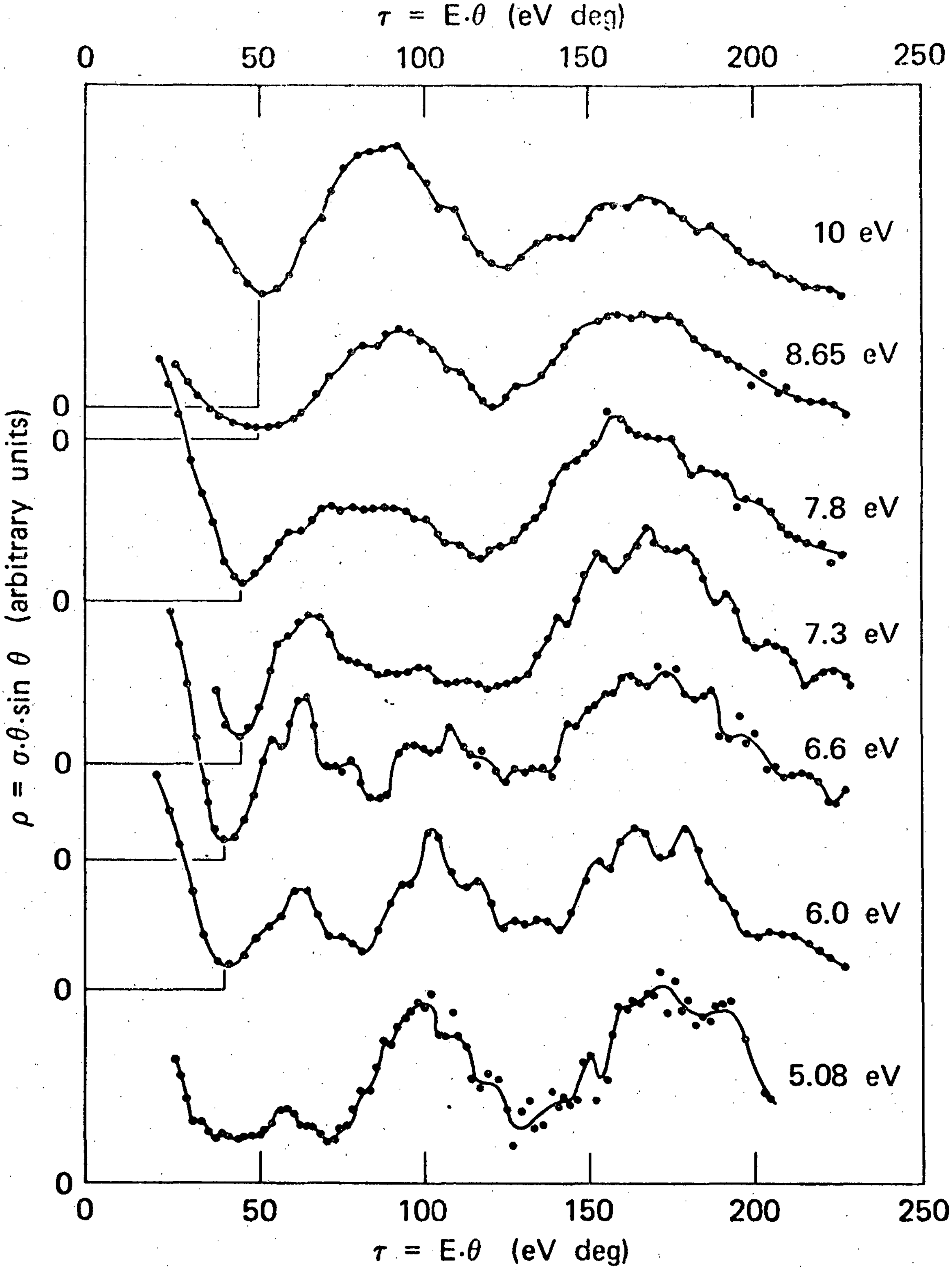

TA-7155-4

Fig. 19

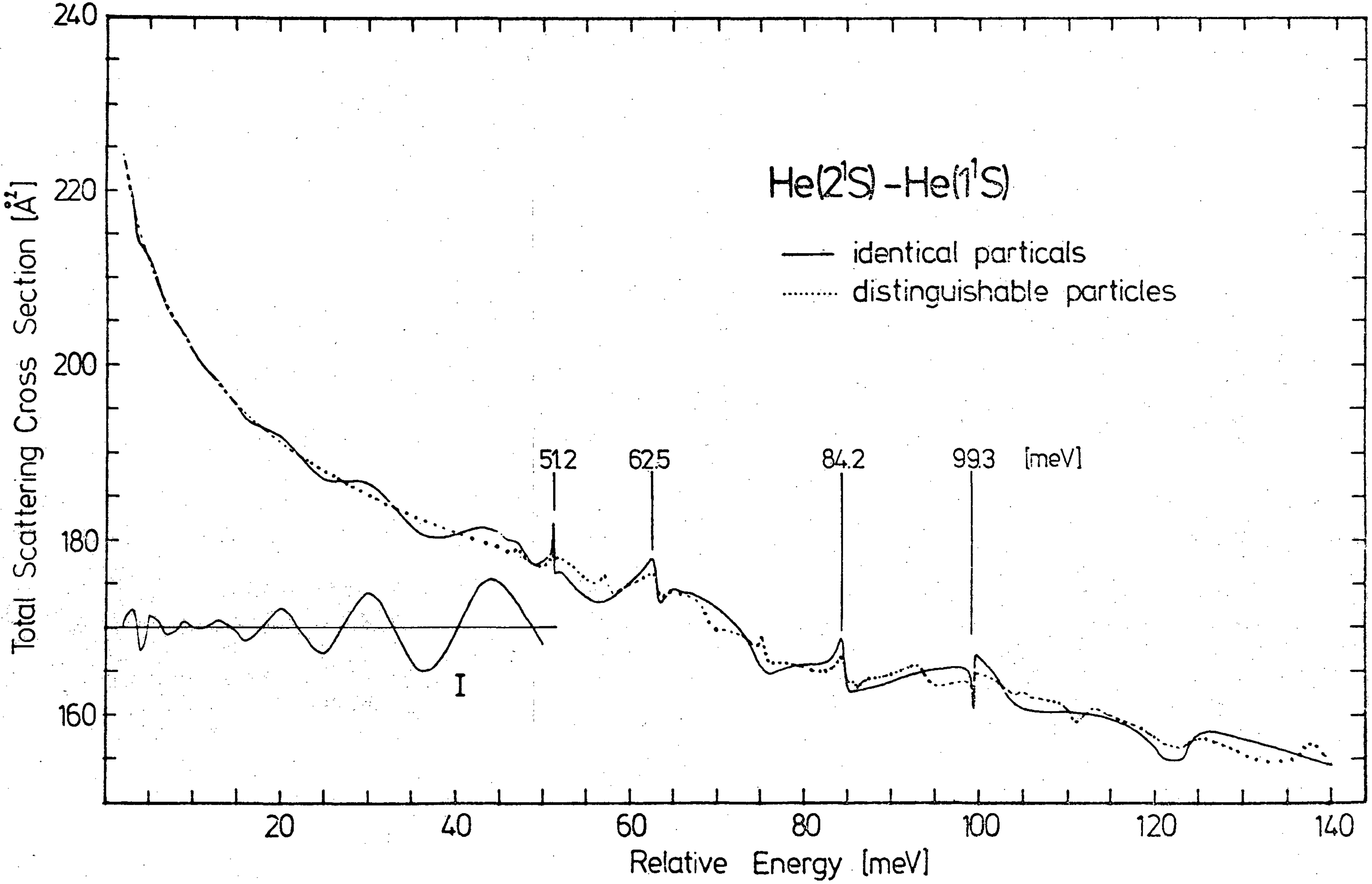
He(2^1S) - He(1^1S)
identical particals
distinguishable particles
51.2
62.5
84.2
99.3
[meV]
I
240
220
200
180
160
Total Scattering Cross Section [Å²]
20
40
60
80
100
120
140
Relative Energy [meV]

Fig. 20

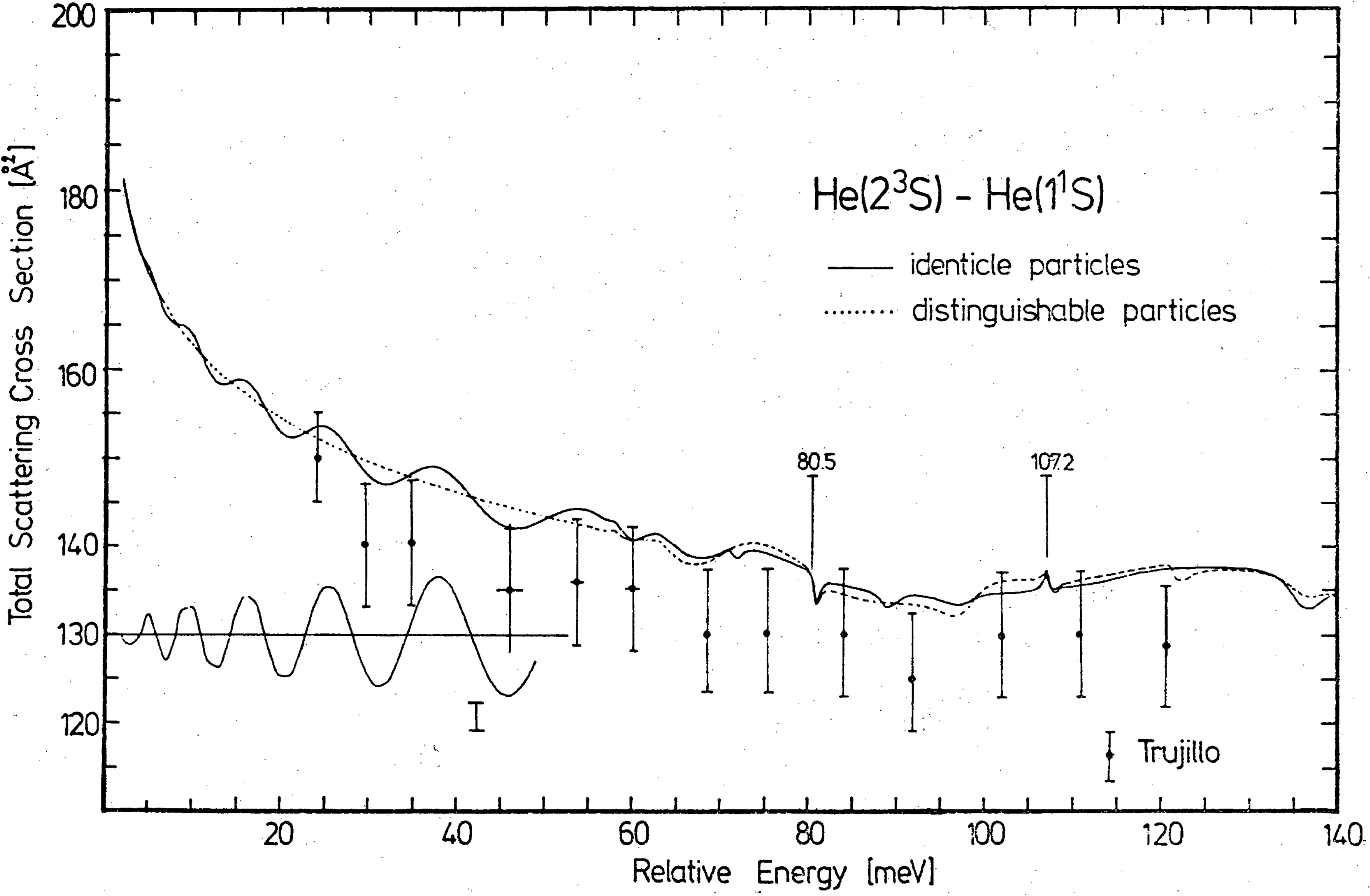
Total Scattering Cross Section [Å²]
200
180
160
140
130
120
20
40
60
80
100
120
140
Relative Energy [meV]
He(2^{3}S) - He(1^{1}S)
identicle particles
distinguishable particles
80.5
107.2
Trujillo

Fig. 21

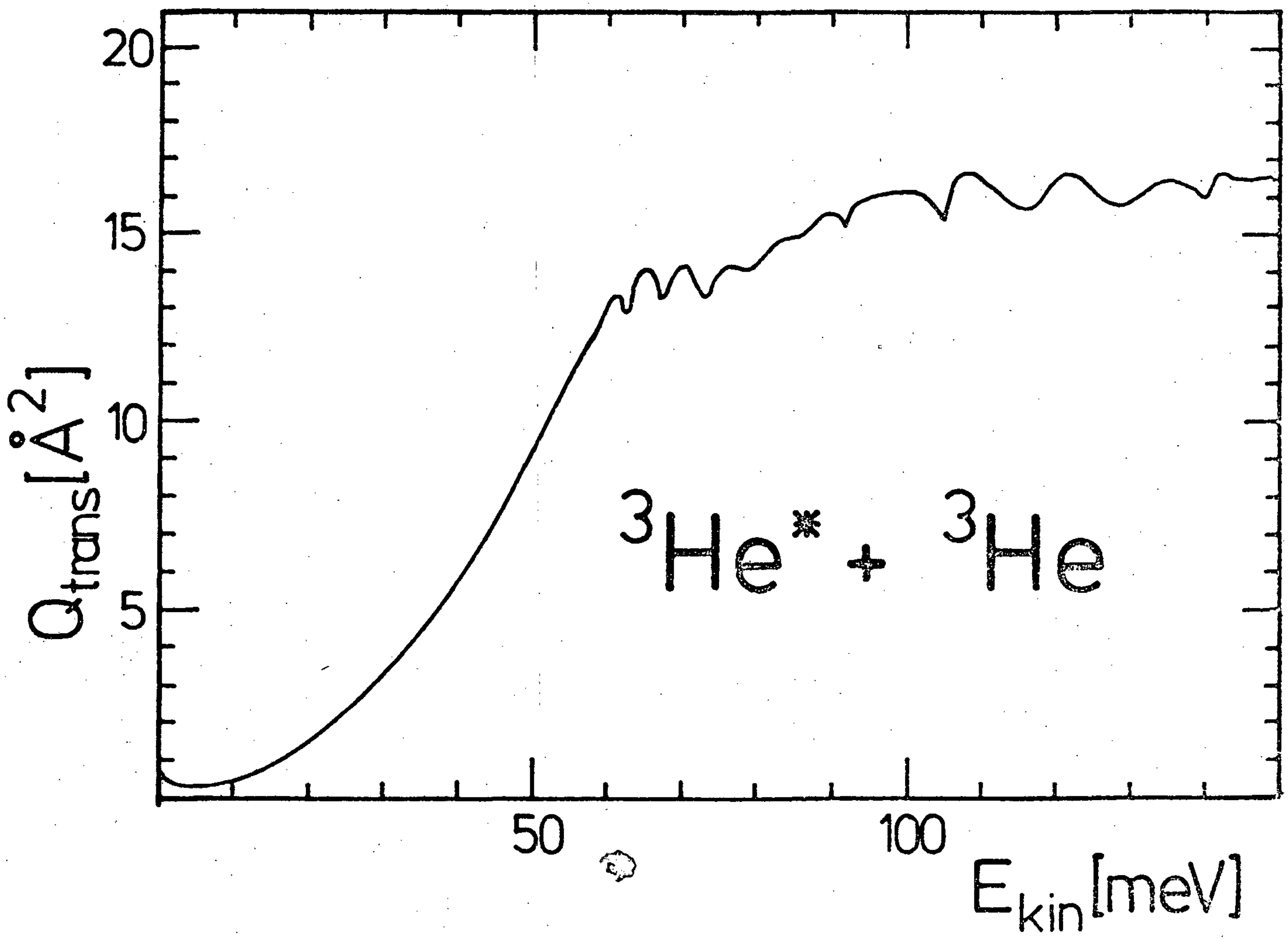

Total Cross Section for Excitation Transfer

Fig. 22

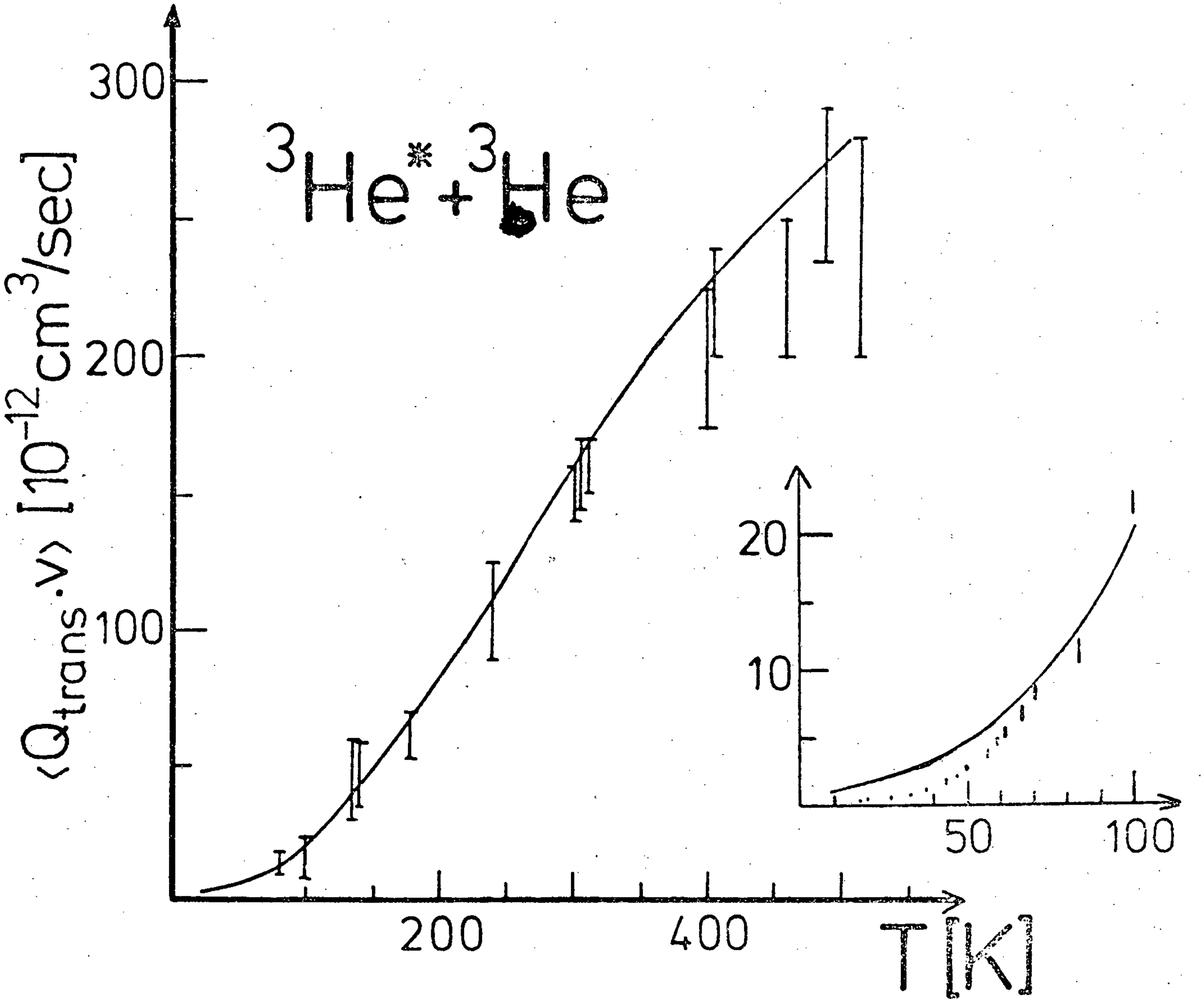

Rate Constant for Excitation Transfer

Fig. 23.

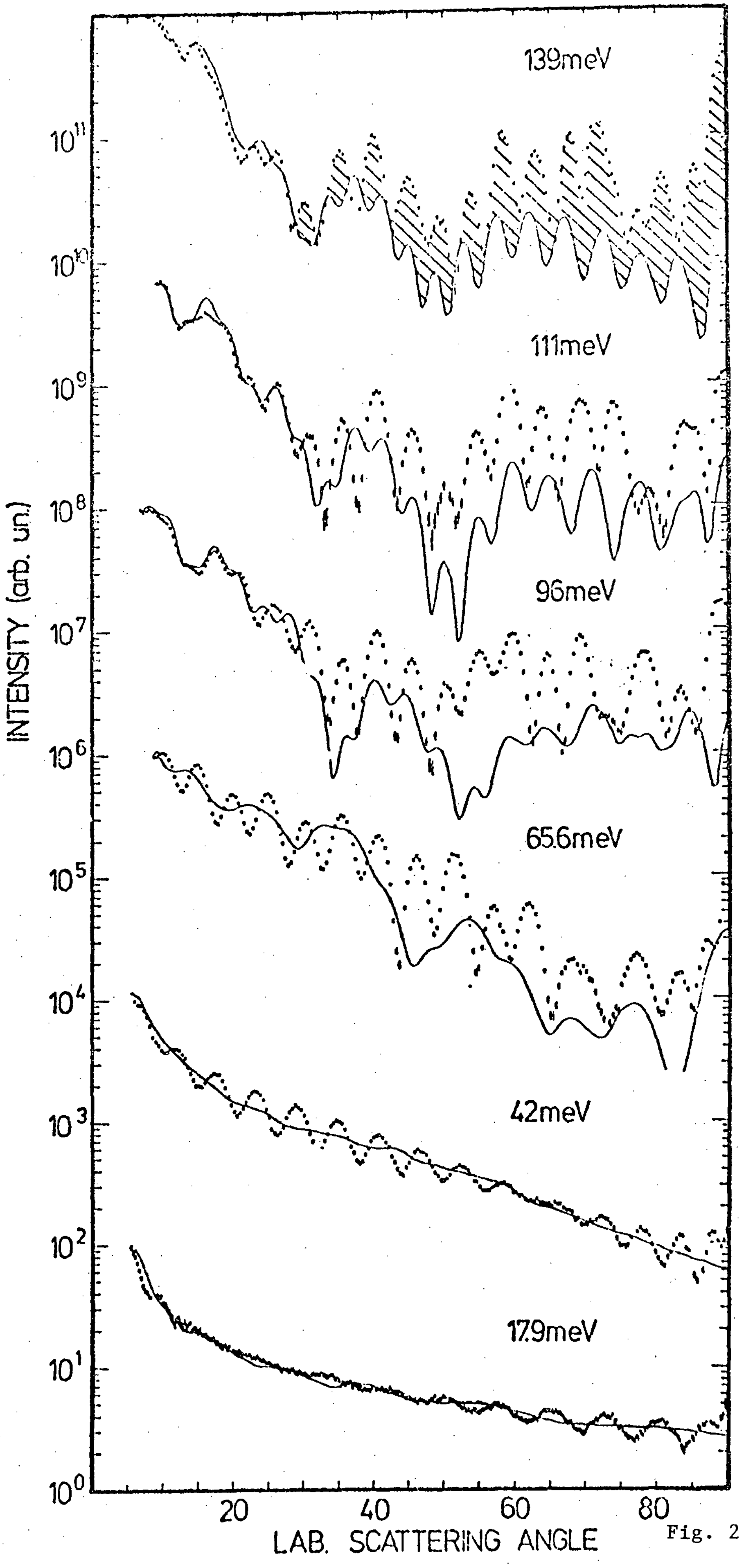
139meV
111meV
96meV
65.6meV
42meV
17.9meV
INTENSITY (arb. un.)
10^{11}
10^{10}
10^{9}
10^{8}
10^{7}
10^{6}
10^{5}
10^{4}
10^{3}
10^{2}
10^{1}
10^{0}
20
40
60
80
LAB. SCATTERING ANGLE

Fig. 24

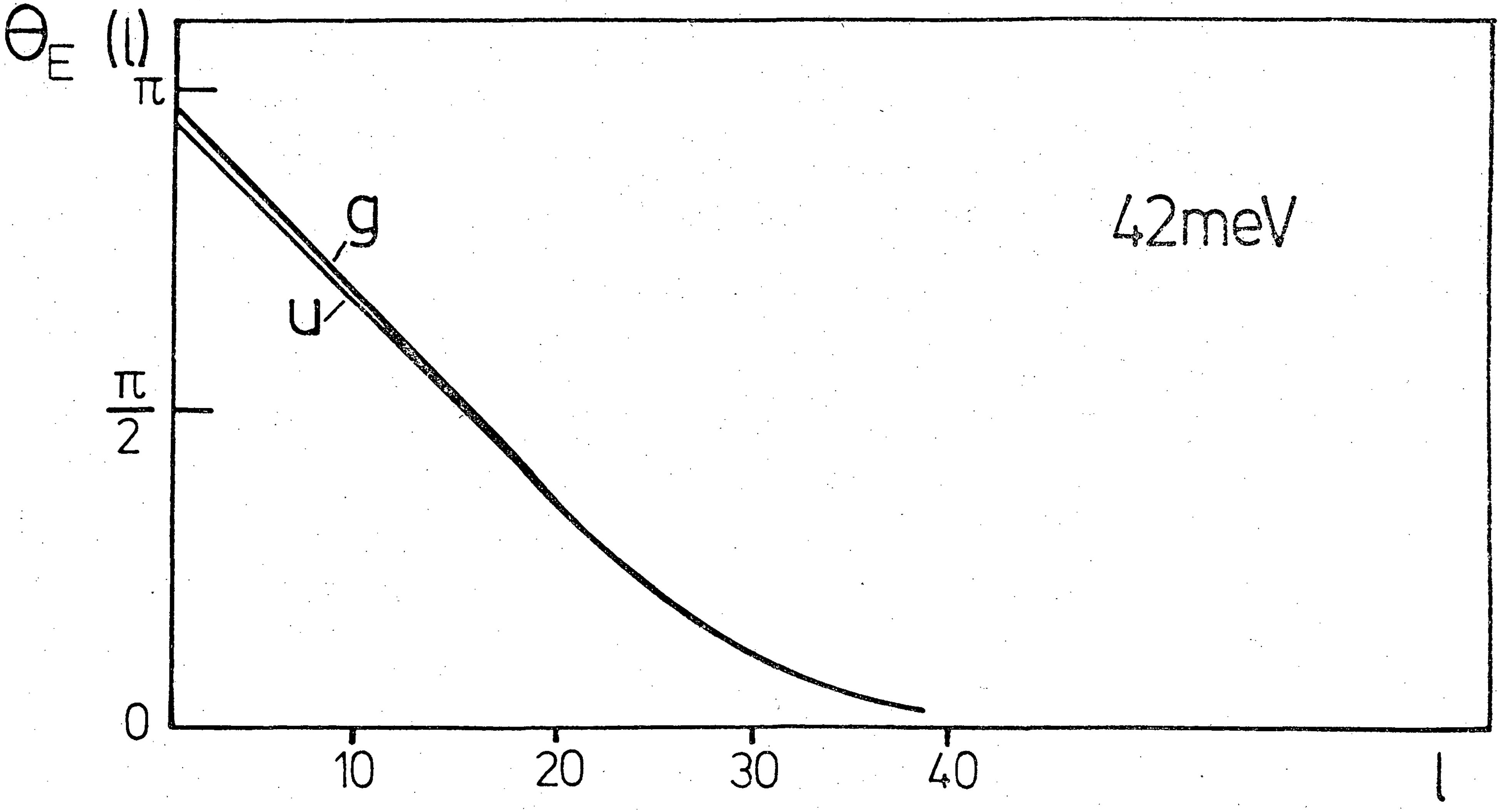

Fig. 25

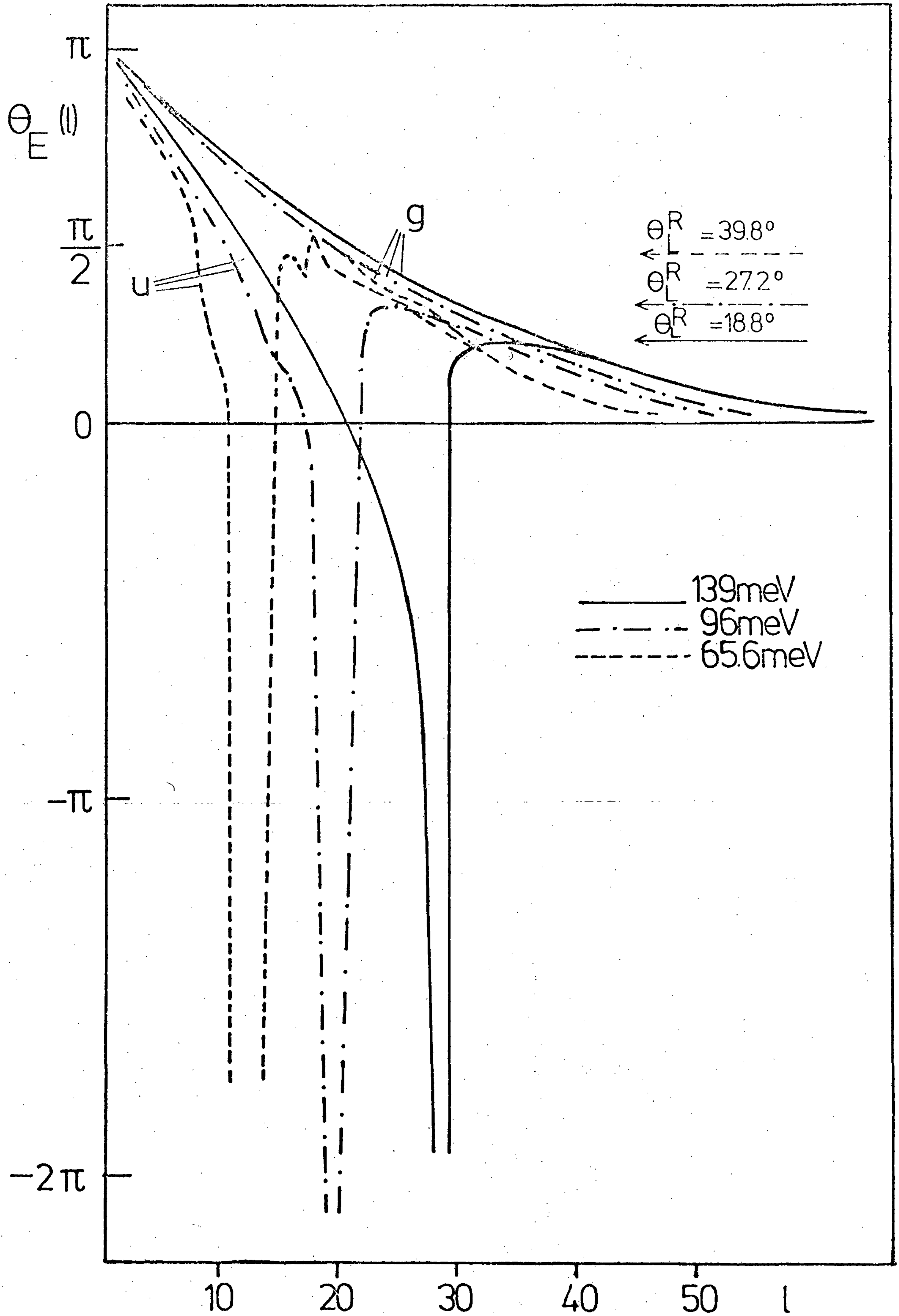
π
$\theta_E(l)$
$\frac{\pi}{2}$
0
−π
−2π
u
g
$\theta_L^R = 39.8°$
$\theta_L^R = 27.2°$
$\theta_L^R = 18.8°$
139meV
96meV
65.6meV
10
20
30
40
50
l

Fig. 26

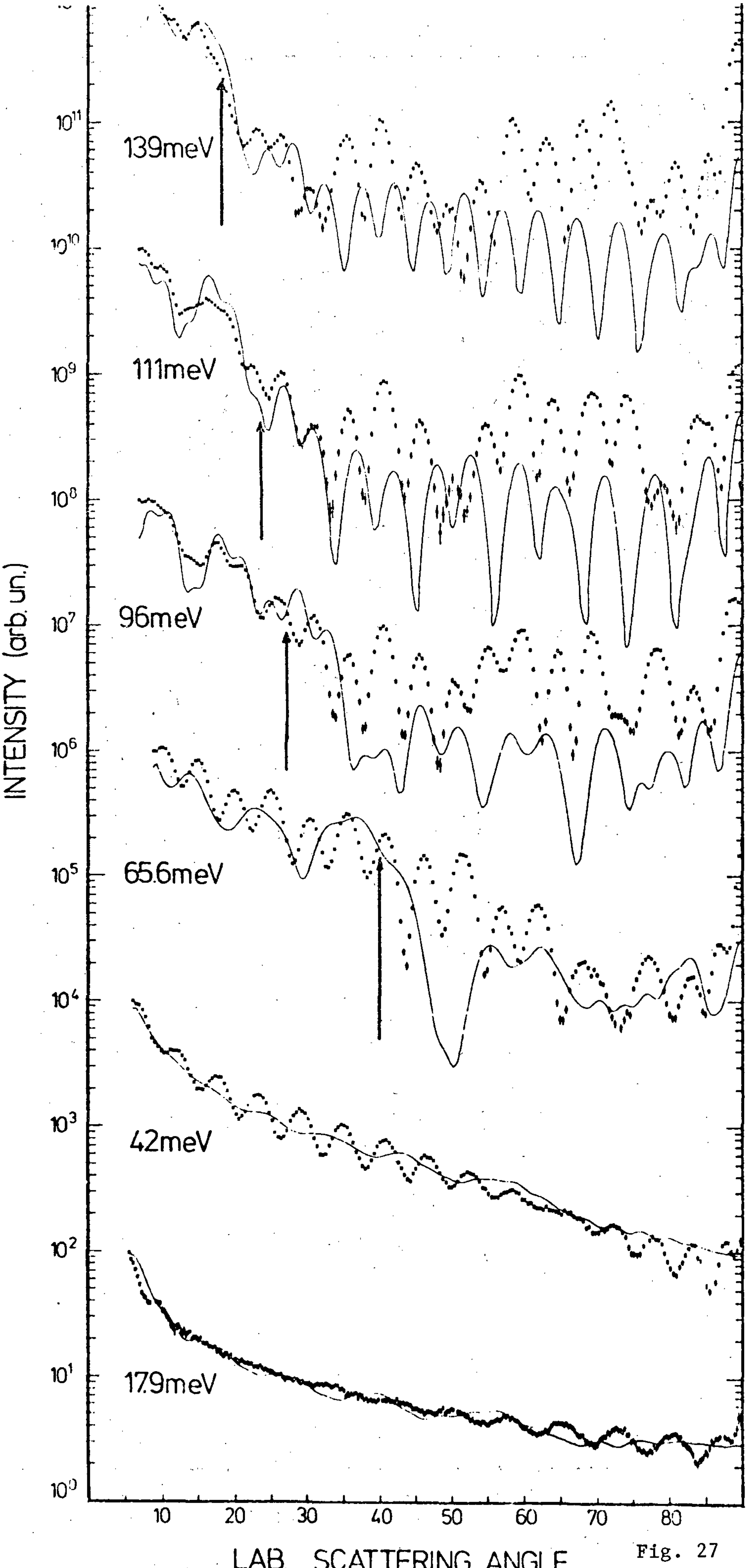
INTENSITY (arb. un.)
LAB SCATTERING ANGLE
139meV
111meV
96meV
65.6meV
42meV
17.9meV
10^{11}
10^{10}
10^{9}
10^{8}
10^{7}
10^{6}
10^{5}
10^{4}
10^{3}
10^{2}
10^{1}
10^{0}
10
20
30
40
50
60
70
80

Fig. 27

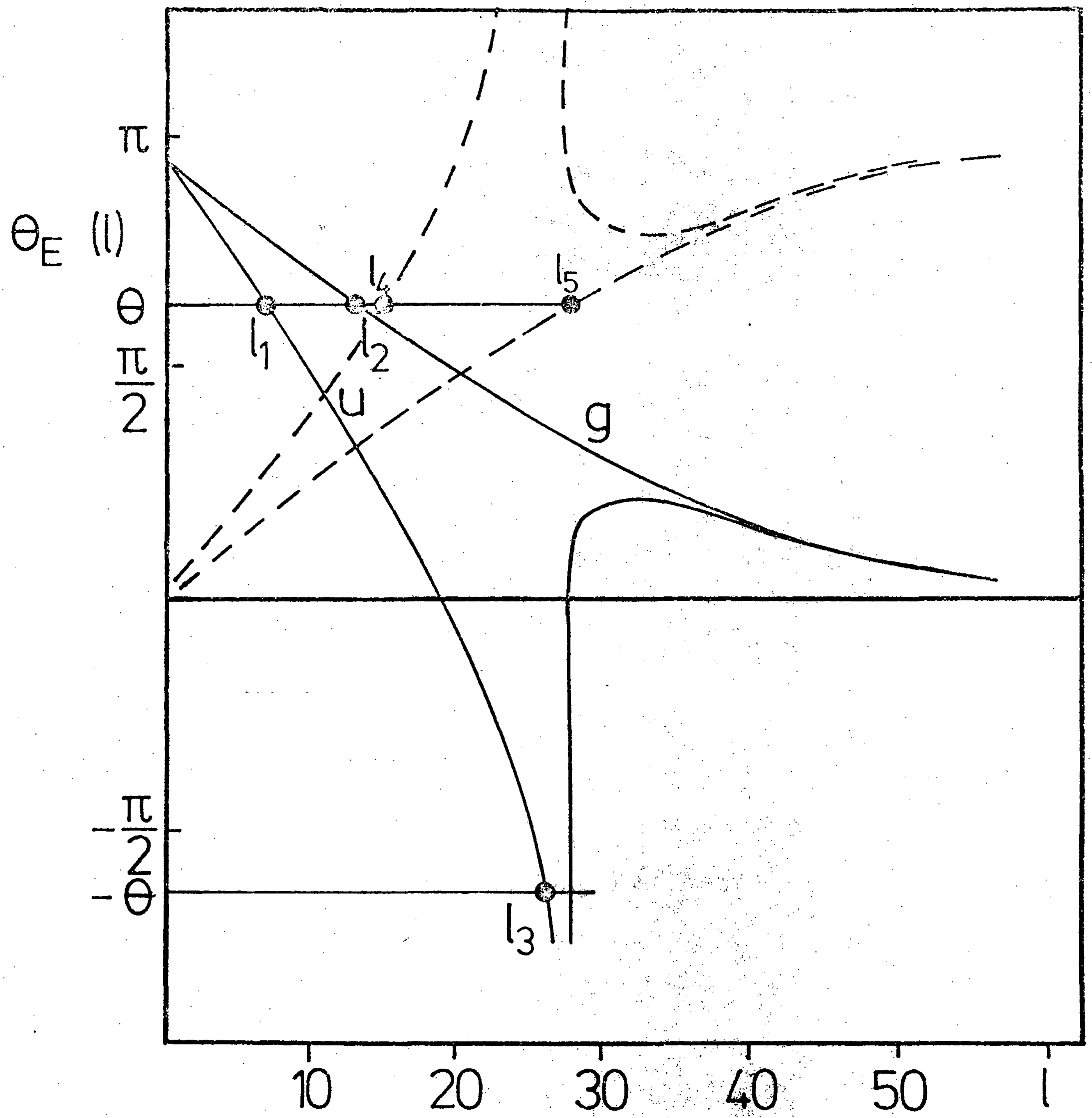
π
Θ_E (l)
Θ
$\frac{\pi}{2}$
$-\frac{\pi}{2}$
$-\Theta$
l_1
l_2
l_3
l_4
l_5
u
g
10
20
30
40
50
l

Fig. 28

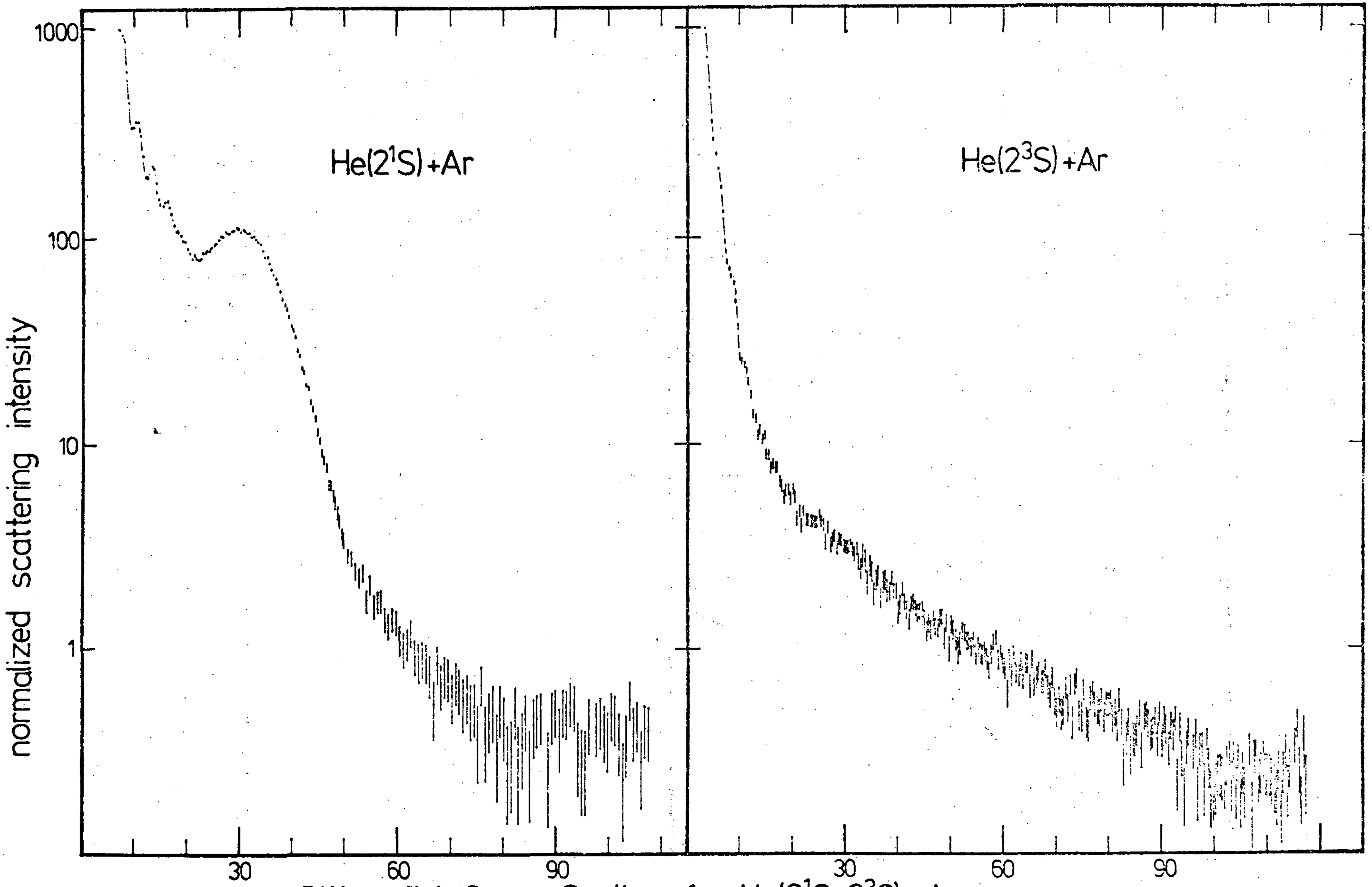

Differential Cross Section for He(2^1S, 2^3S) + Ar,
kinetic energy: E_{CM} = 66meV

Fig. 29

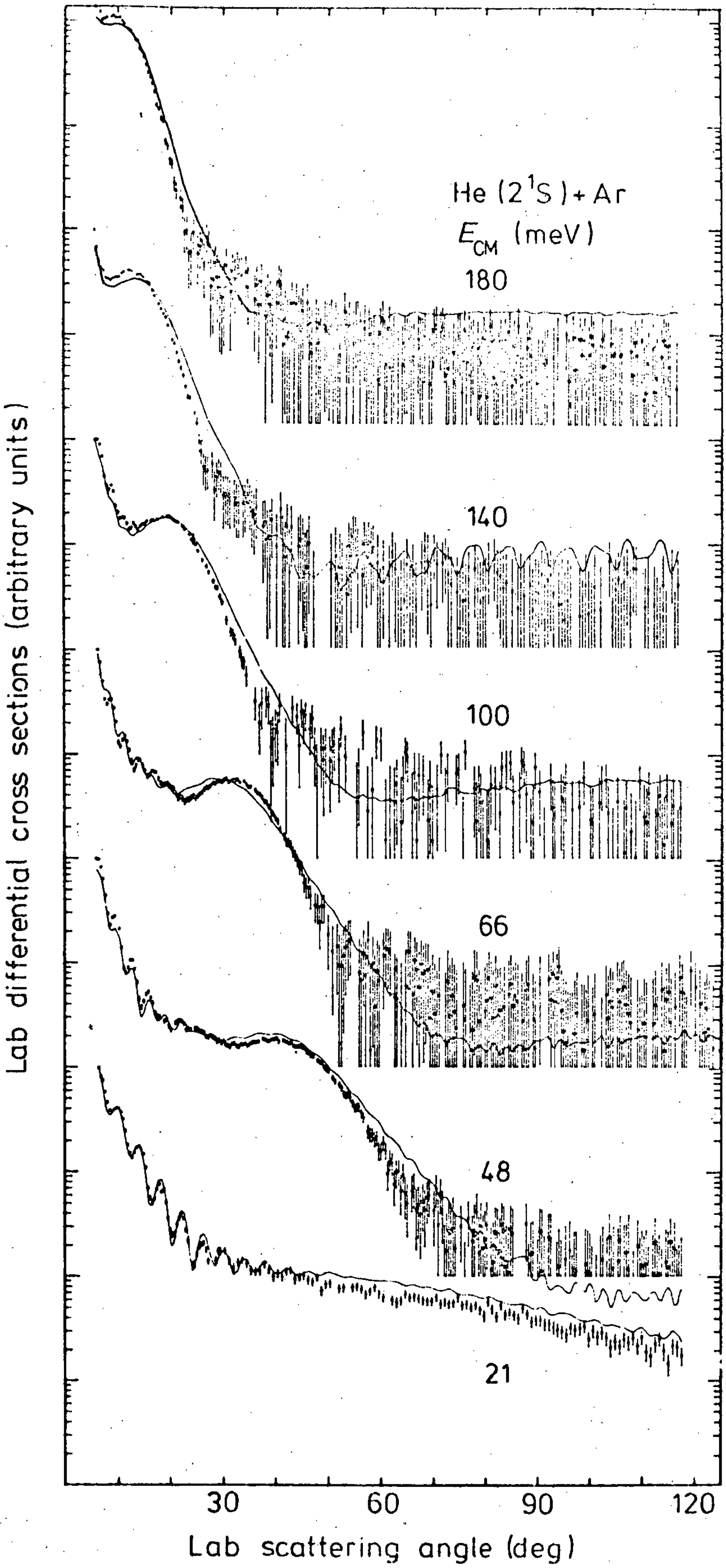
He (2¹S) + Ar
E_CM (meV)
180
140
100
66
48
21
Lab differential cross sections (arbitrary units)
30
60
90
120
Lab scattering angle (deg)

Fig. 30

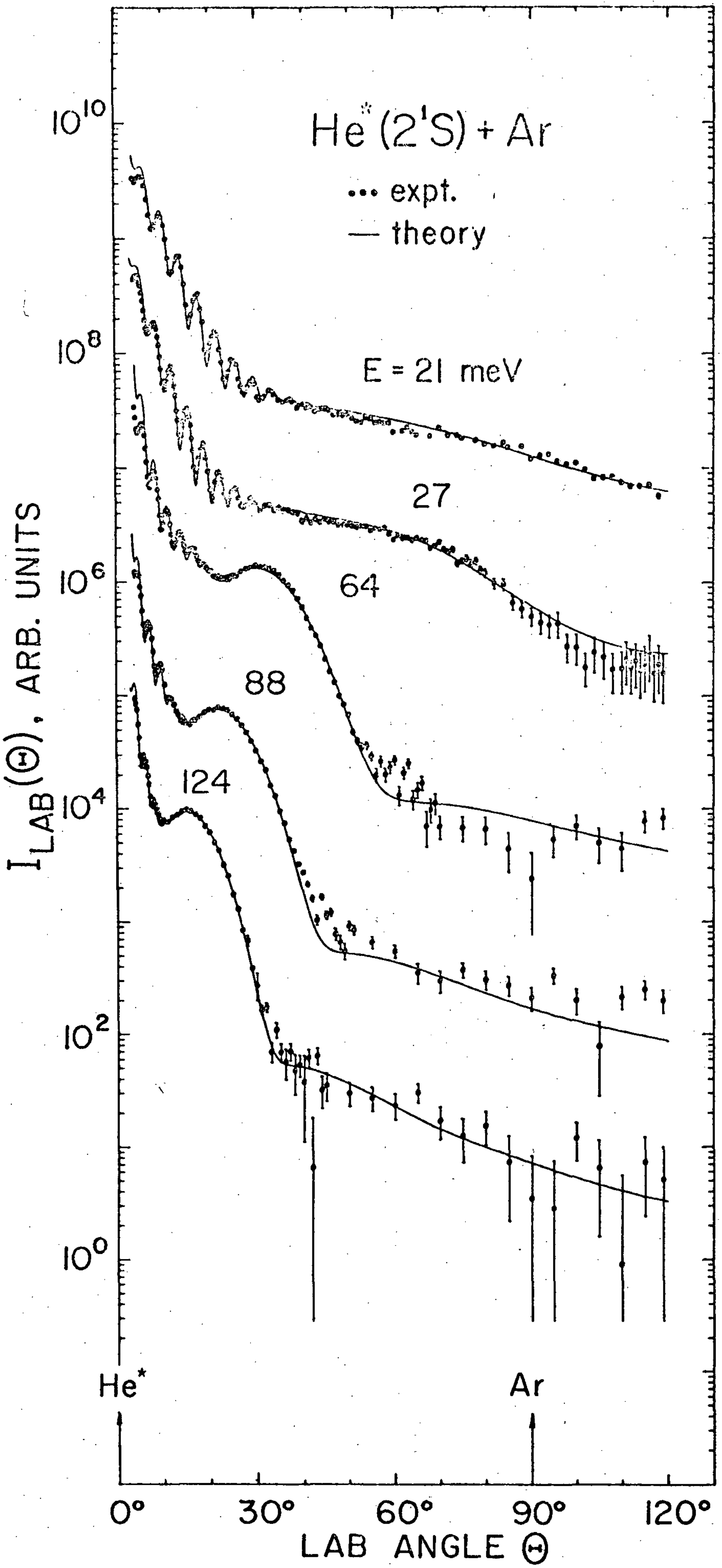
He*(2¹S) + Ar
••• expt.
— theory
E = 21 meV
27
64
88
124
10¹⁰
10⁸
10⁶
10⁴
10²
10⁰
I_LAB(Θ), ARB. UNITS
He*
Ar
0°
30°
60°
90°
120°
LAB ANGLE Θ

Fig. 31

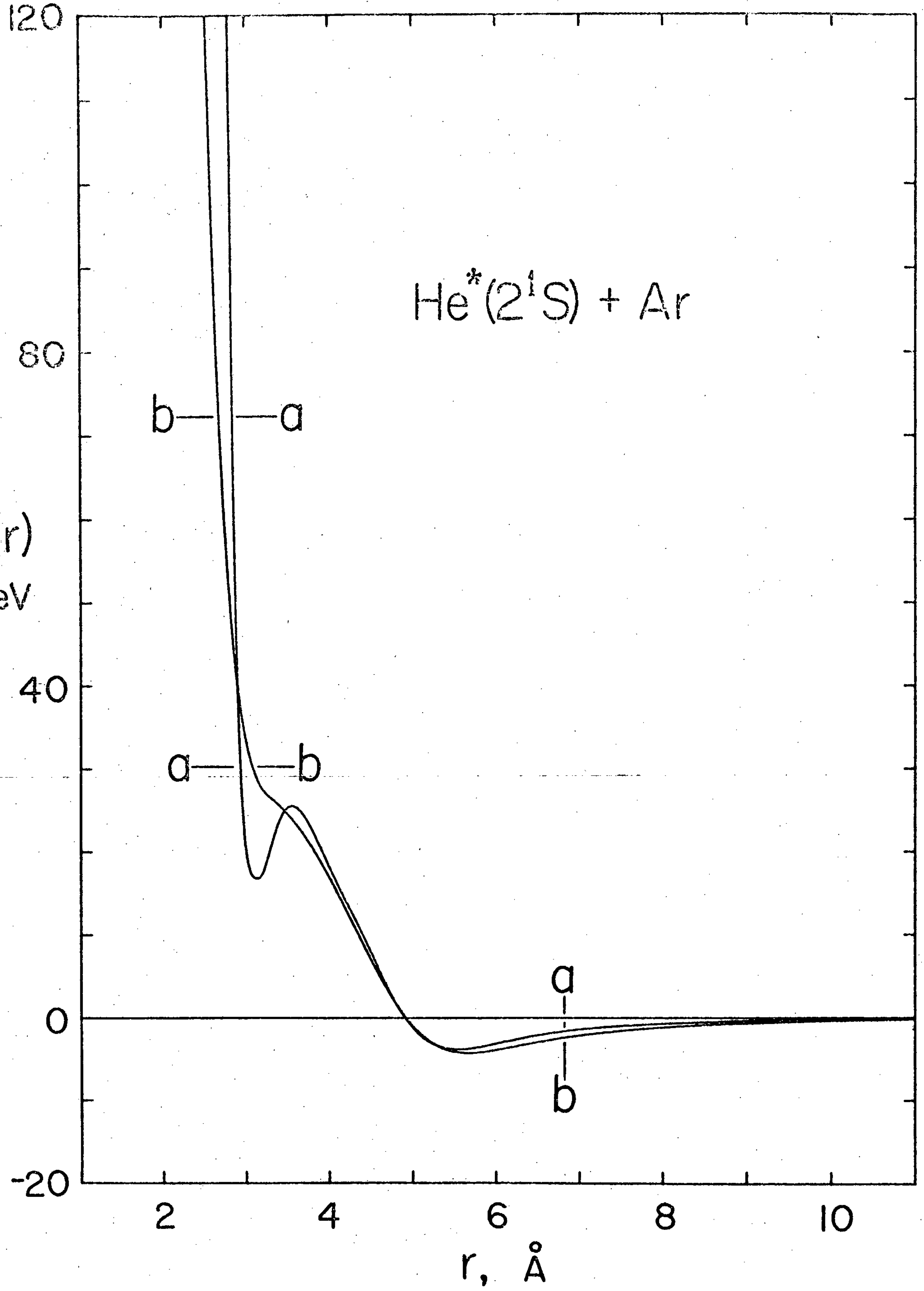

Fig. 32

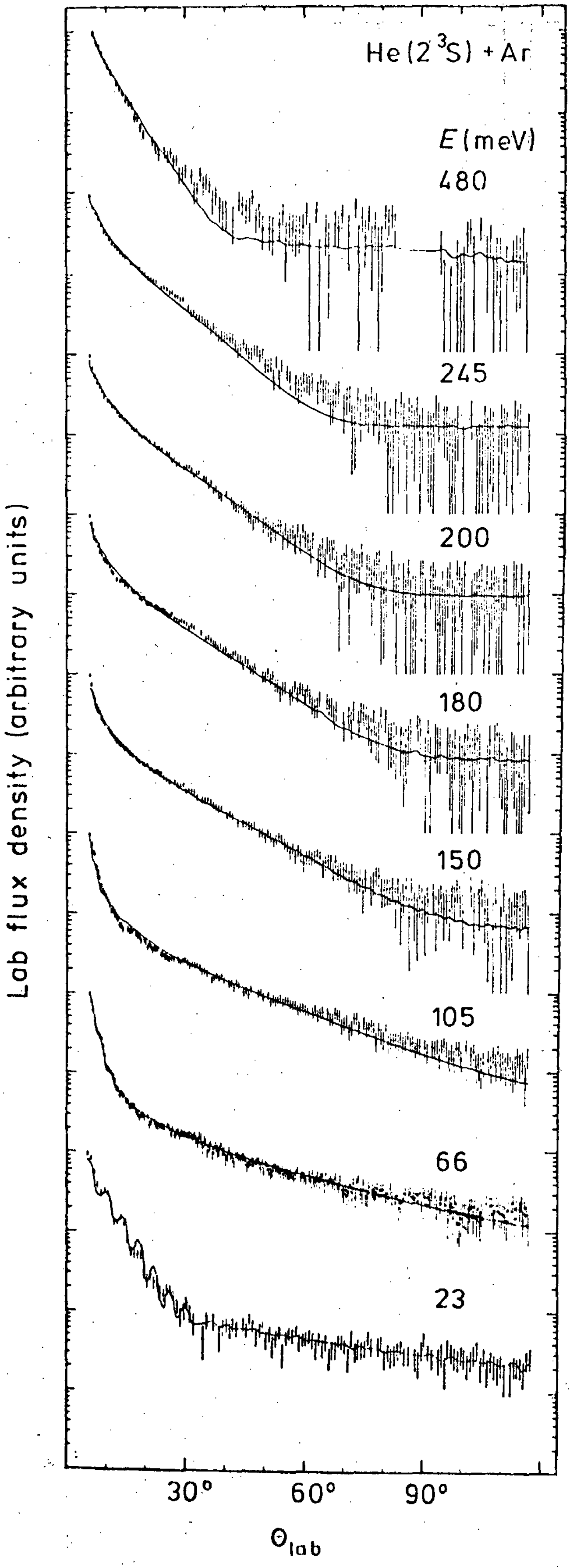
He(2 ³S) + Ar
E (meV)
480
245
200
180
150
105
66
23
Lab flux density (arbitrary units)
30°
60°
90°
Θlab

Fig. 33

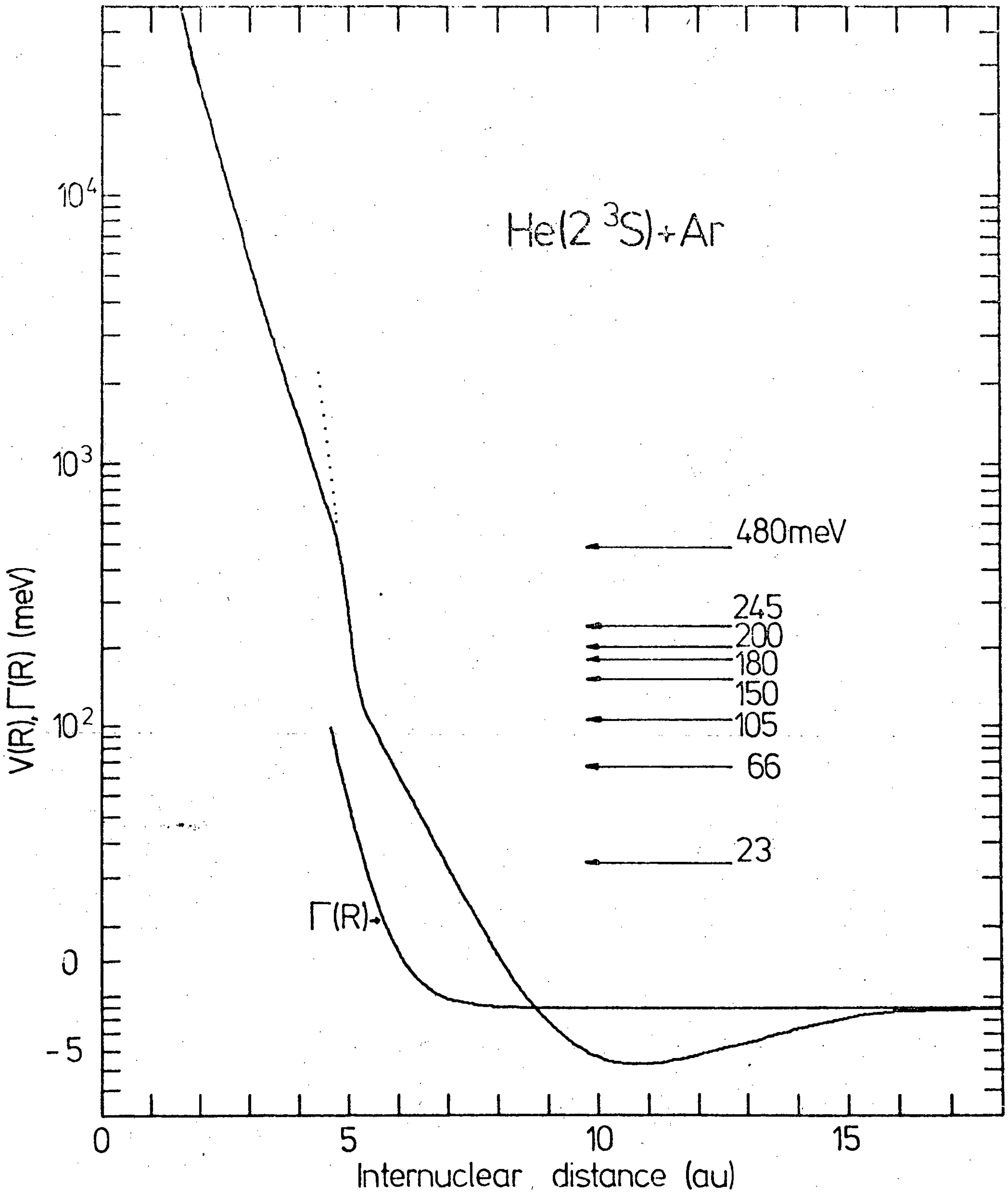
He(2 ^{3}S)+Ar
480meV
245
200
180
150
105
66
23
Γ(R)
10^4
10^3
10^2
0
-5
V(R), Γ(R) (meV)
0
5
10
15
Internuclear distance (au)

Fig. 34

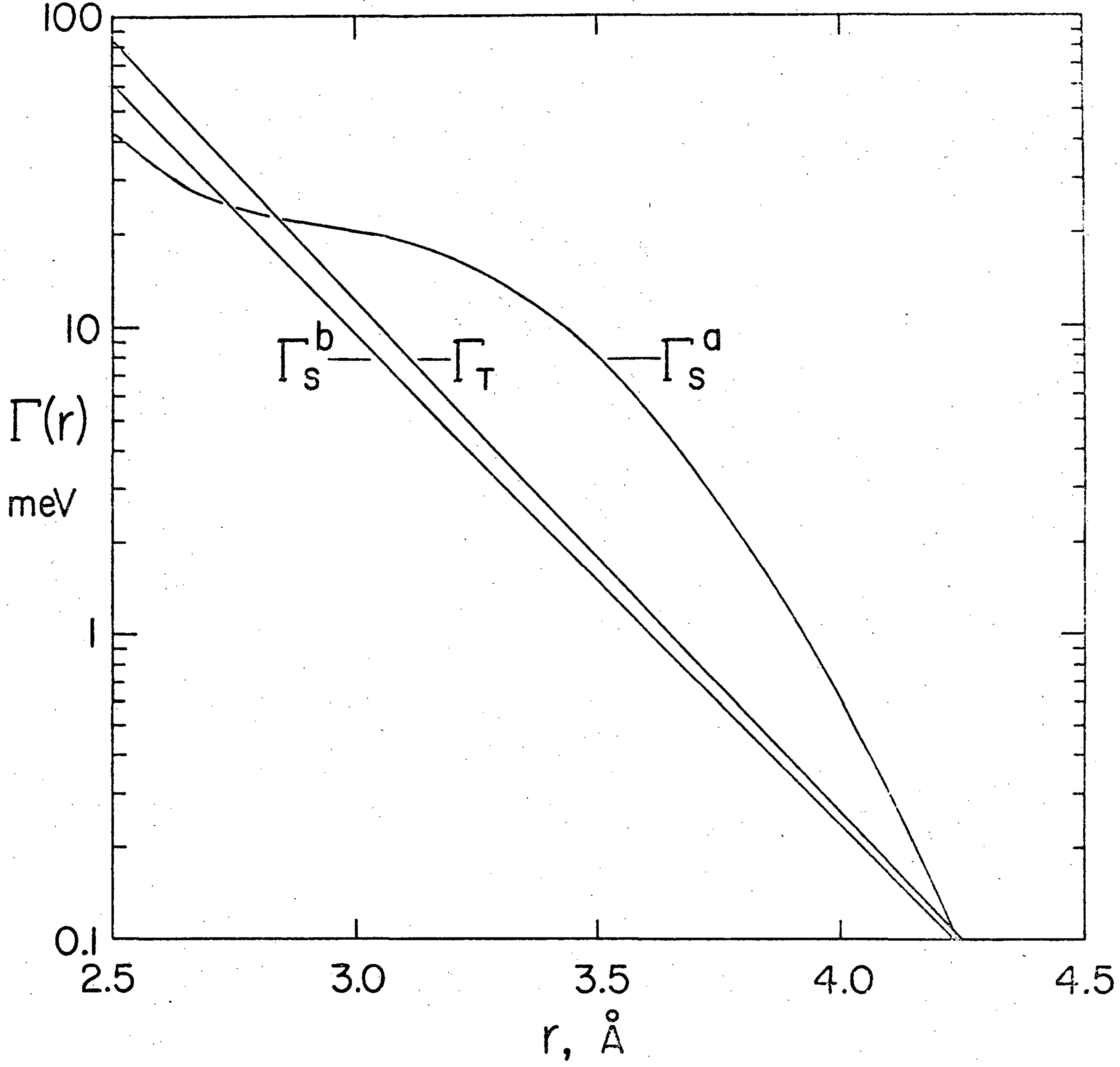

Fig. 35

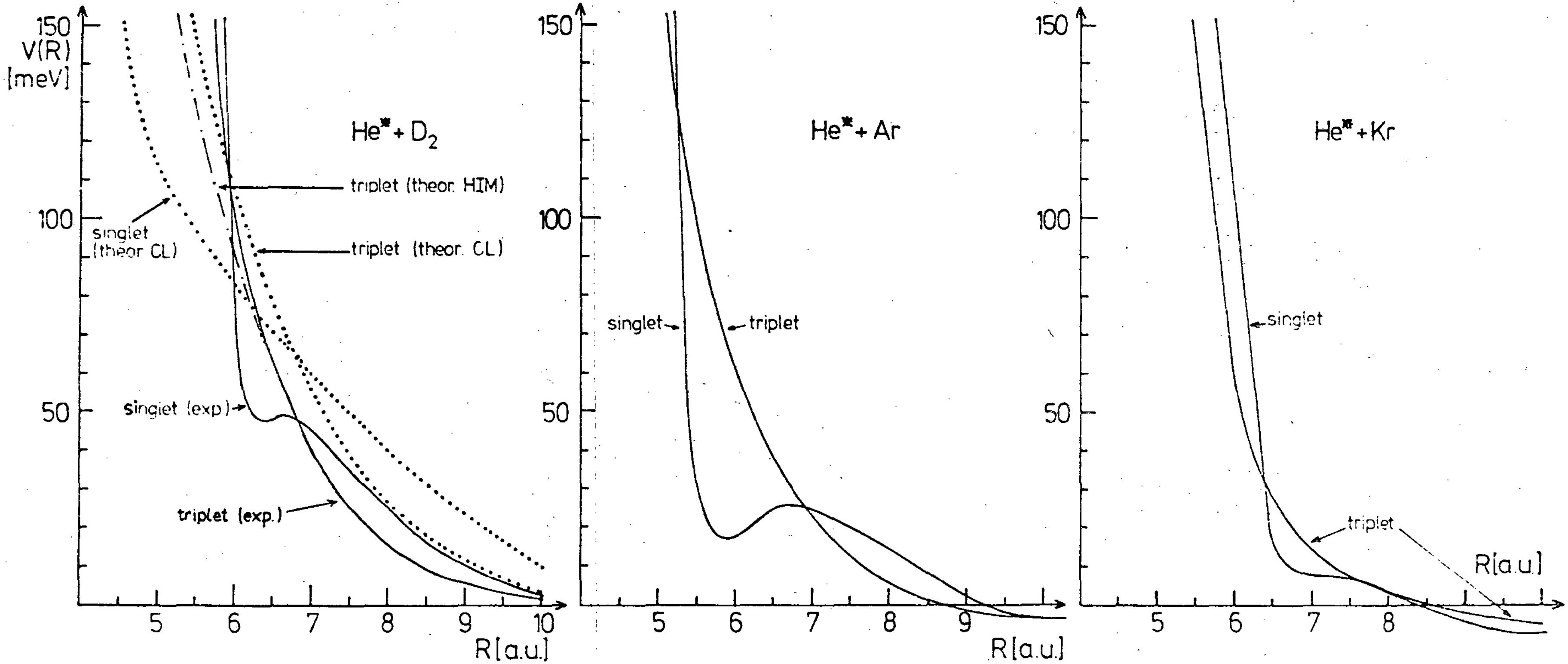

Potentials for He(2^1S), He(2^3S), + D_2, Ar, Kr

Fig. 36

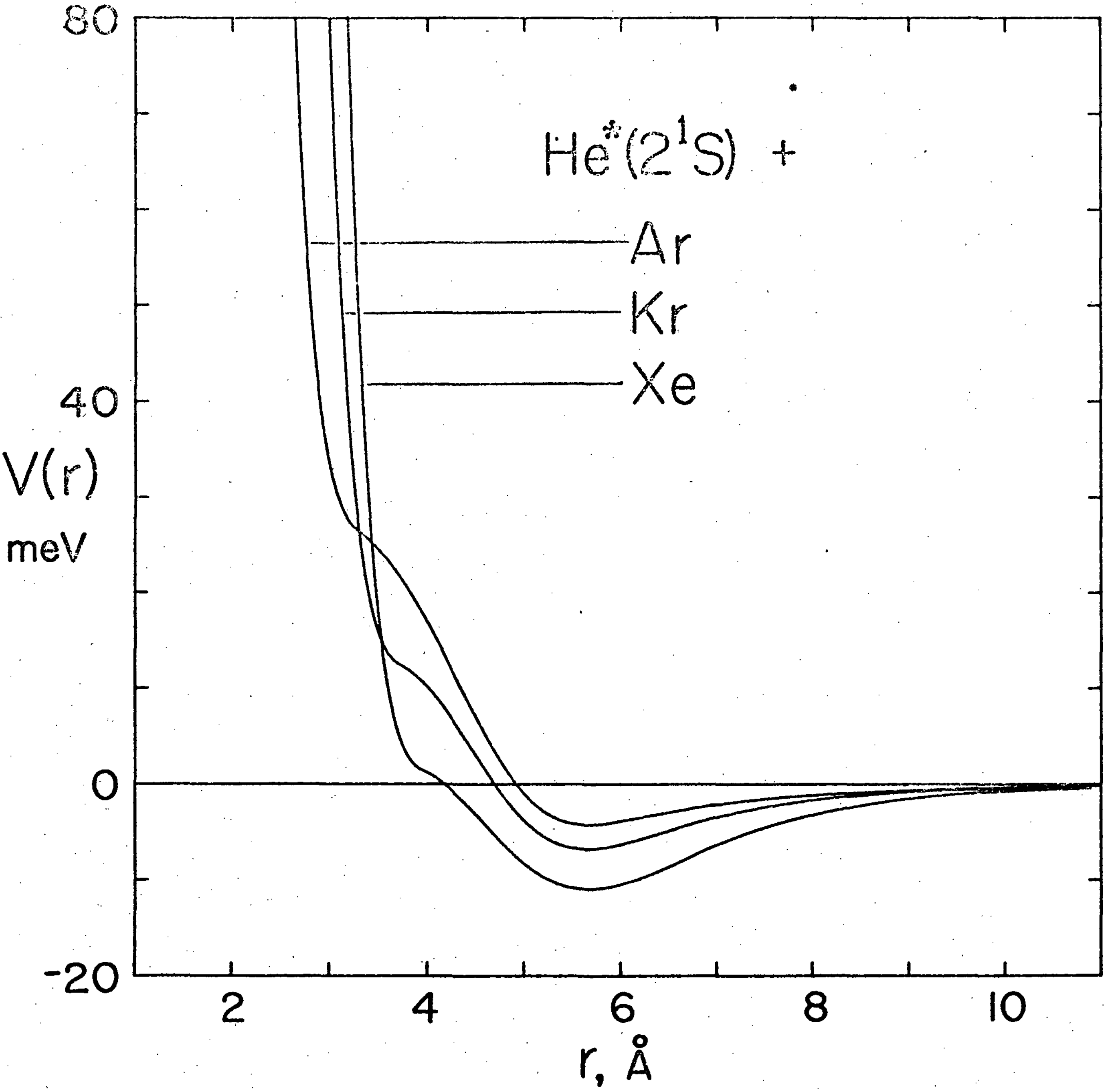

Fig. 37

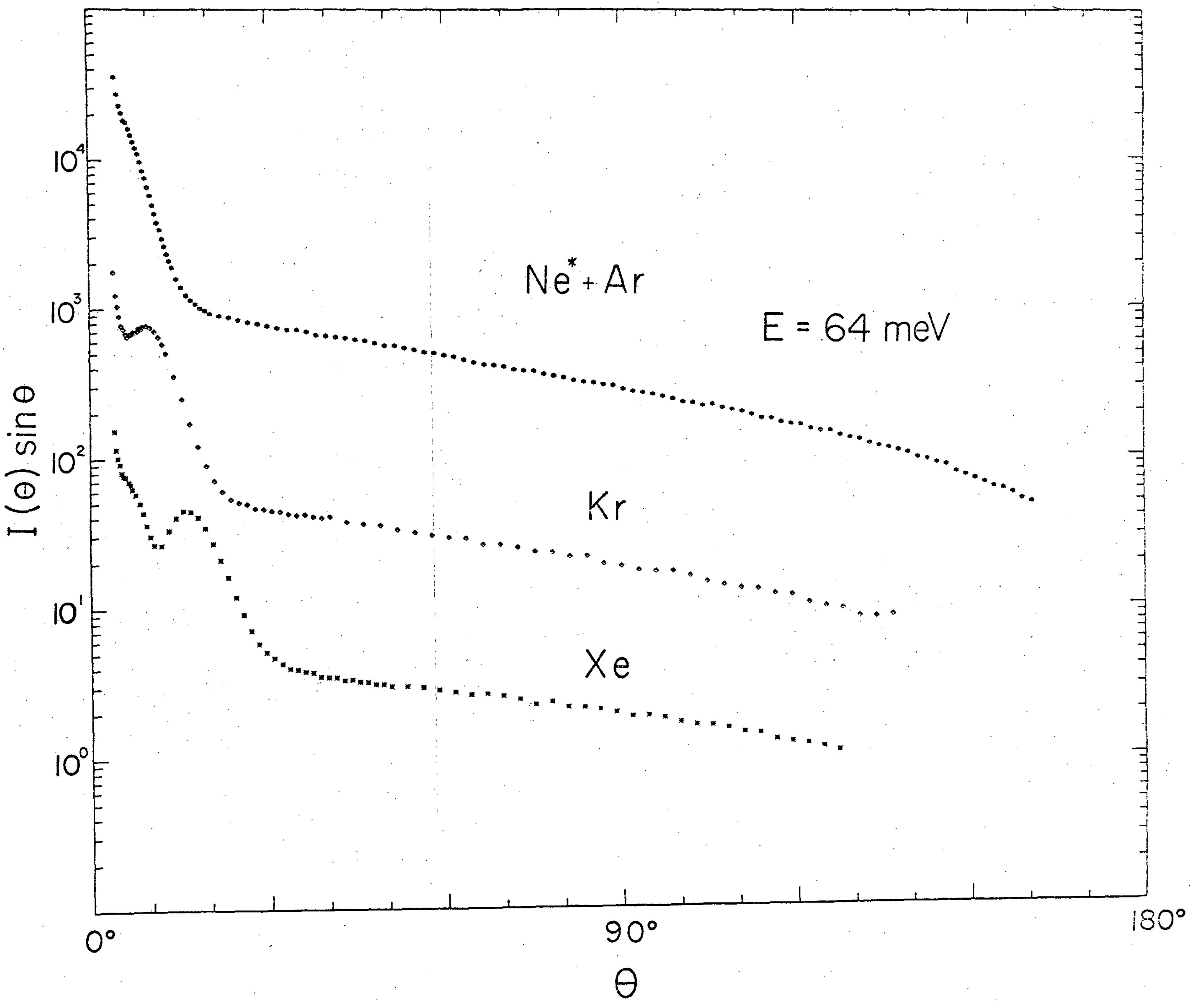

Fig. 38

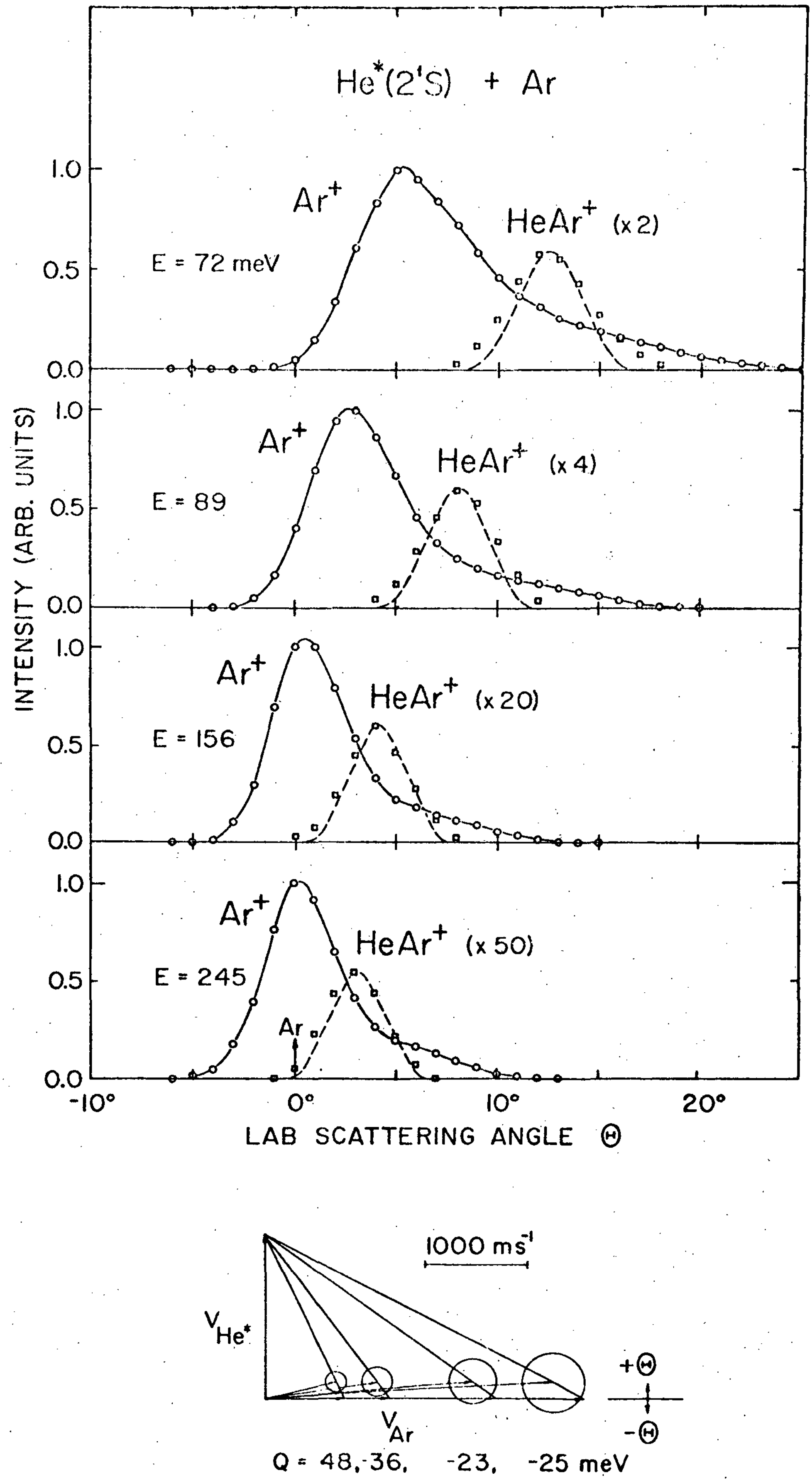
He*(2'S) + Ar
Ar+
HeAr+ (x2)
E = 72 meV
Ar+
HeAr+ (x4)
E = 89
Ar+
HeAr+ (x20)
E = 156
Ar+
HeAr+ (x50)
E = 245
Ar
INTENSITY (ARB. UNITS)
0.0
0.5
1.0
-10°
0°
10°
20°
LAB SCATTERING ANGLE Θ
1000 ms-1
V He*
V Ar
+Θ
-Θ
Q = 48, -36, -23, -25 meV

Fig. 39

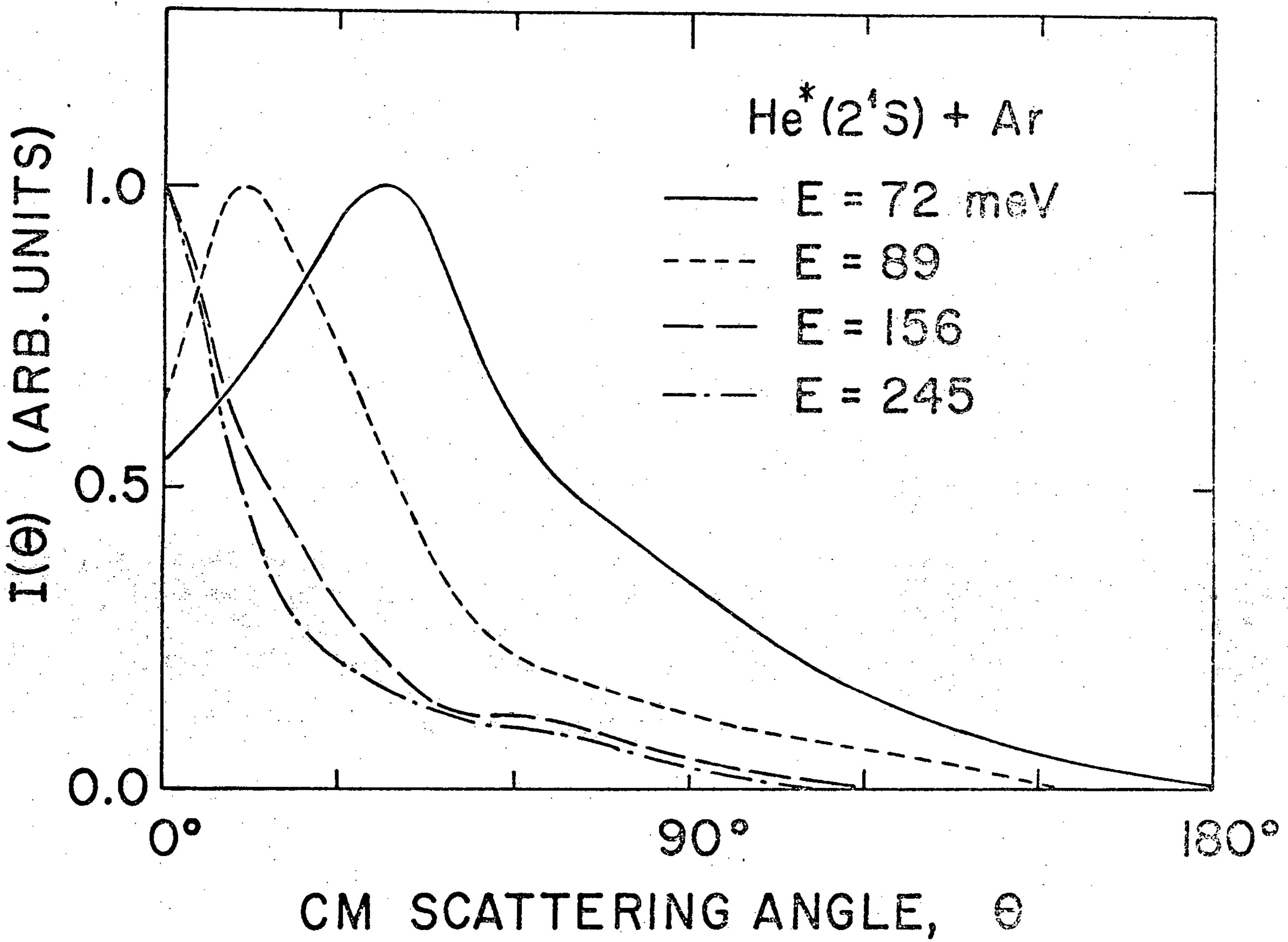
He*(2¹S) + Ar
E = 72 meV
E = 89
E = 156
E = 245
I(Θ) (ARB. UNITS)
1.0
0.5
0.0
0°
90°
180°
CM SCATTERING ANGLE, Θ

Fig. 40

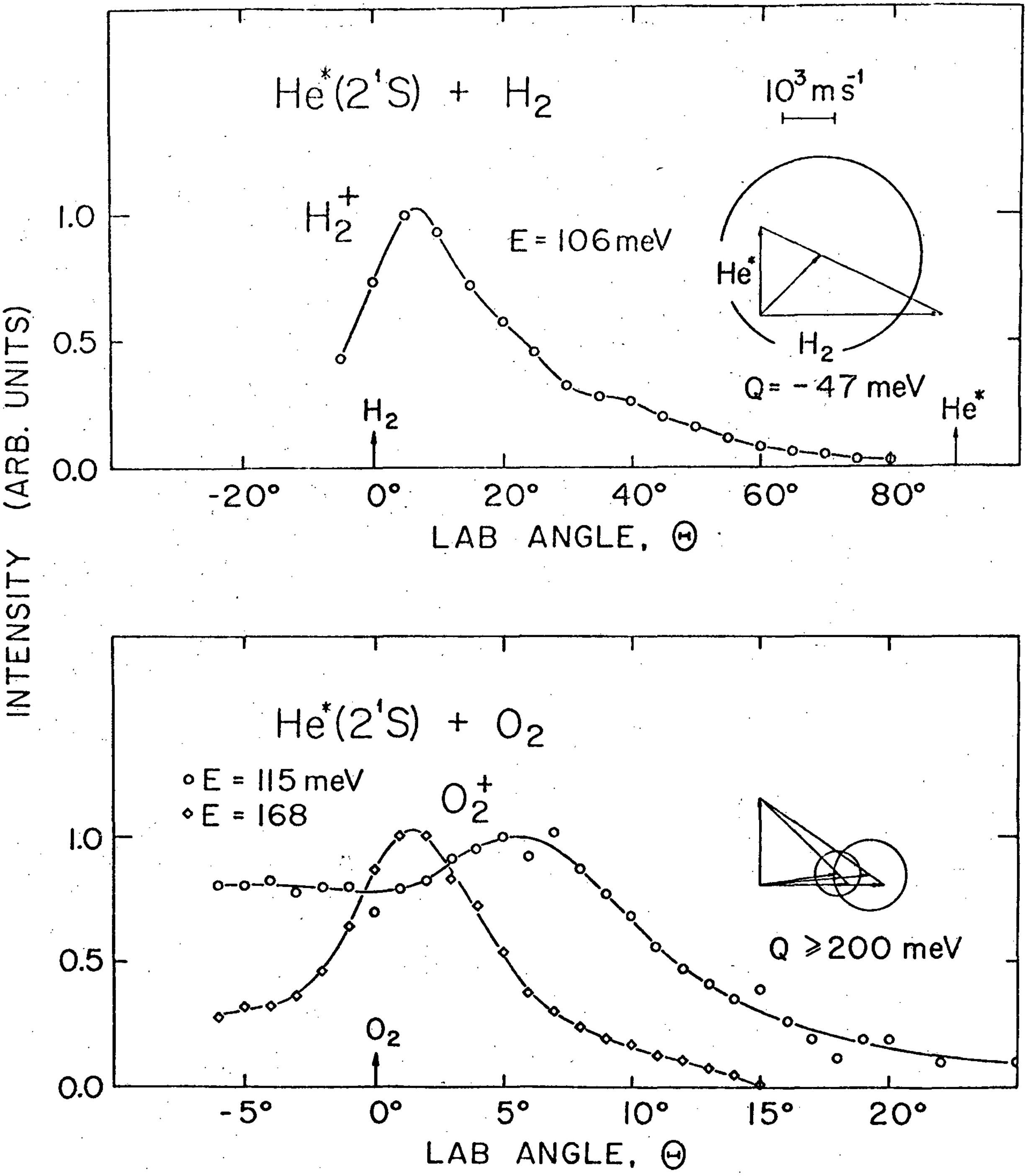
He*(2¹S) + H₂
10³ m s⁻¹
H₂⁺
E = 106 meV
He*
H₂
Q = −47 meV
H₂
He*
1.0
0.5
0.0
-20°
0°
20°
40°
60°
80°
LAB ANGLE, Θ
INTENSITY (ARB. UNITS)
He*(2¹S) + O₂
○ E = 115 meV
◇ E = 168
O₂⁺
Q ≥ 200 meV
O₂
1.0
0.5
0.0
-5°
0°
5°
10°
15°
20°
LAB ANGLE, Θ

Fig. 41

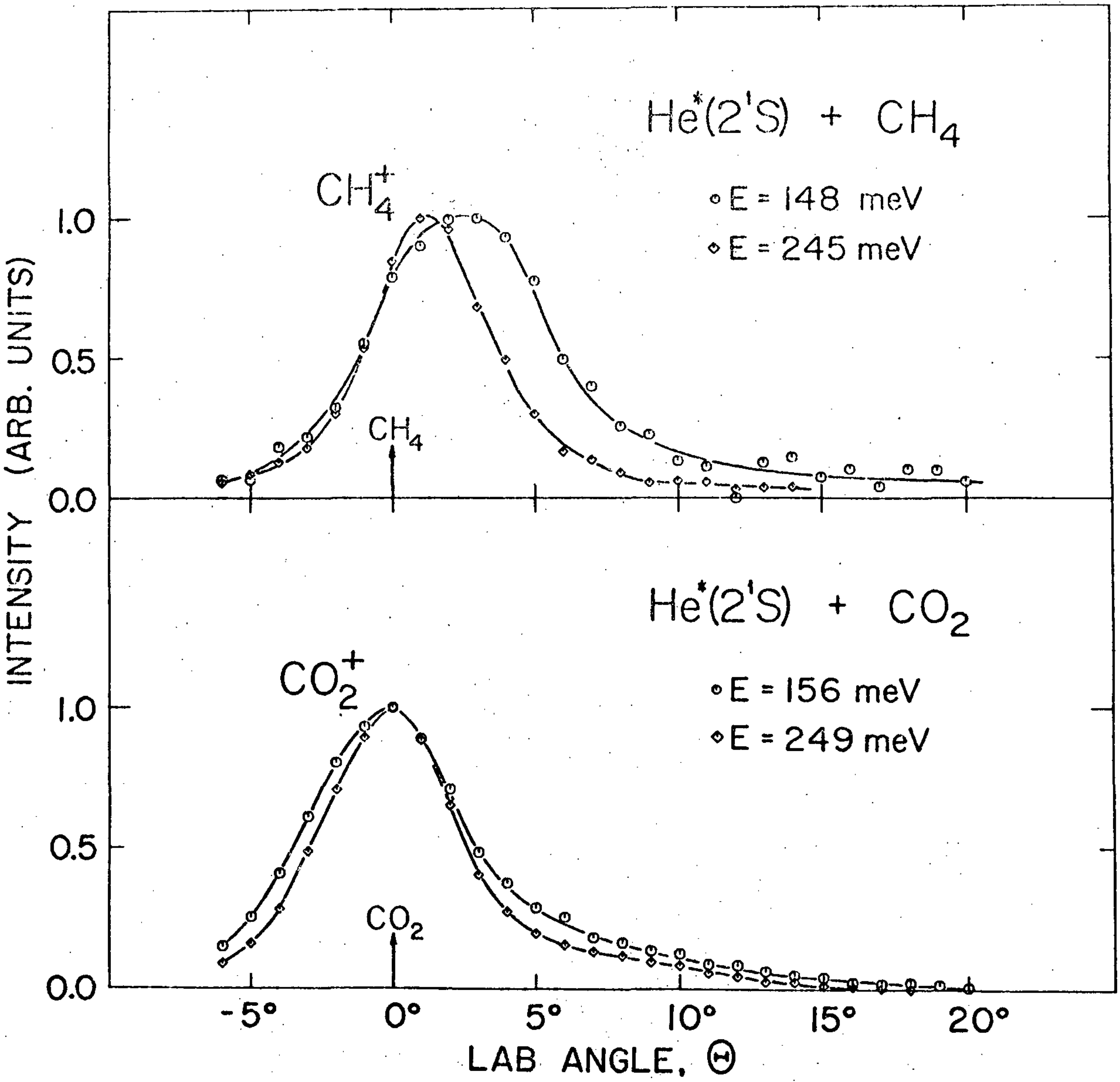
He*(2¹S) + CH₄
CH₄⁺
○ E = 148 meV
◇ E = 245 meV
CH₄
He*(2¹S) + CO₂
CO₂⁺
○ E = 156 meV
◇ E = 249 meV
CO₂
1.0
0.5
0.0
1.0
0.5
0.0
INTENSITY (ARB. UNITS)
-5°
0°
5°
10°
15°
20°
LAB ANGLE, Θ

Fig. 42

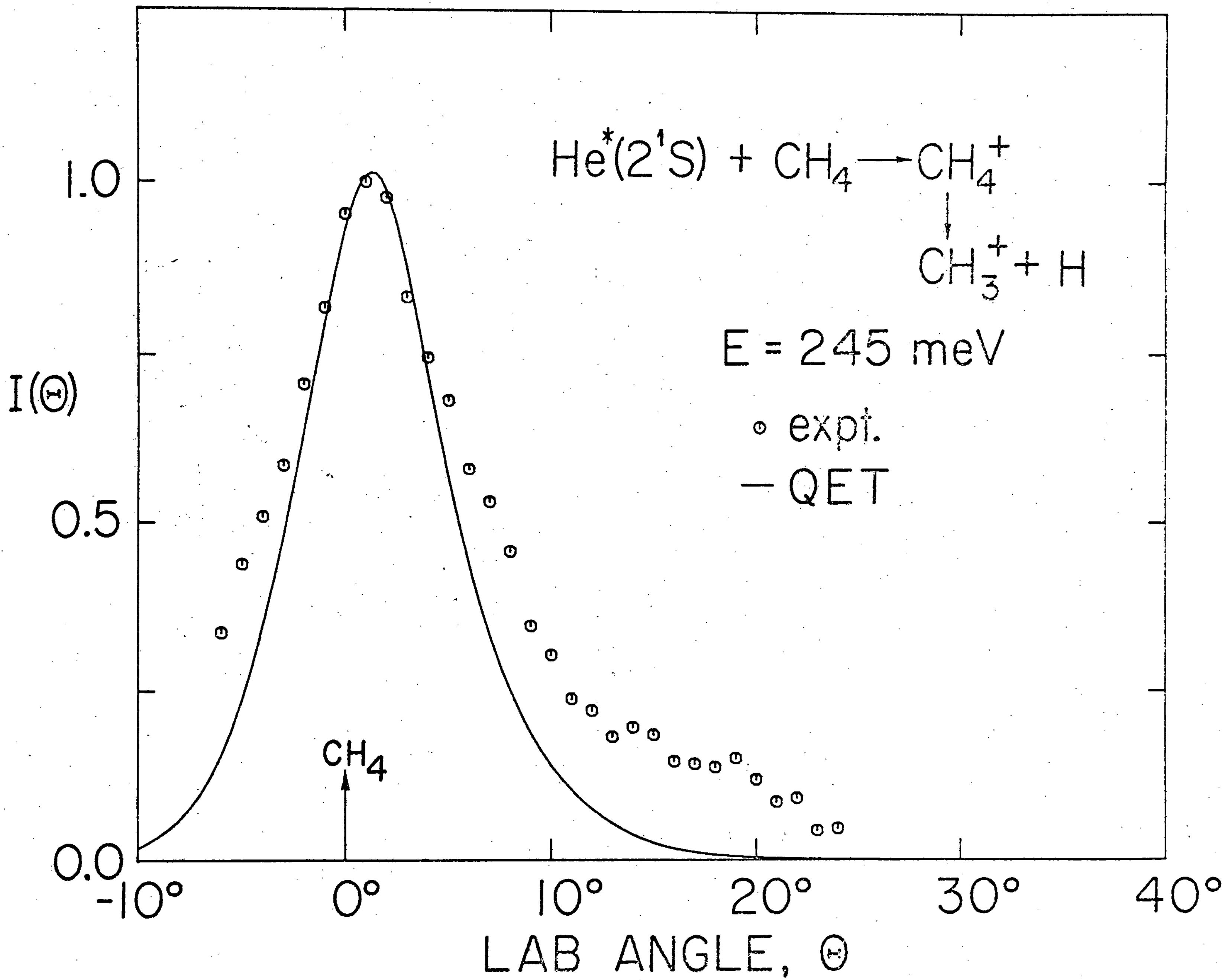
$He^*(2^1S) + CH_4 \longrightarrow CH_4^+$
$\downarrow$
$CH_3^+ + H$
E = 245 meV
○ expt.
— QET
$I(\Theta)$
1.0
0.5
0.0
CH_4
-10°
0°
10°
20°
30°
40°
LAB ANGLE, Θ

Fig. 43

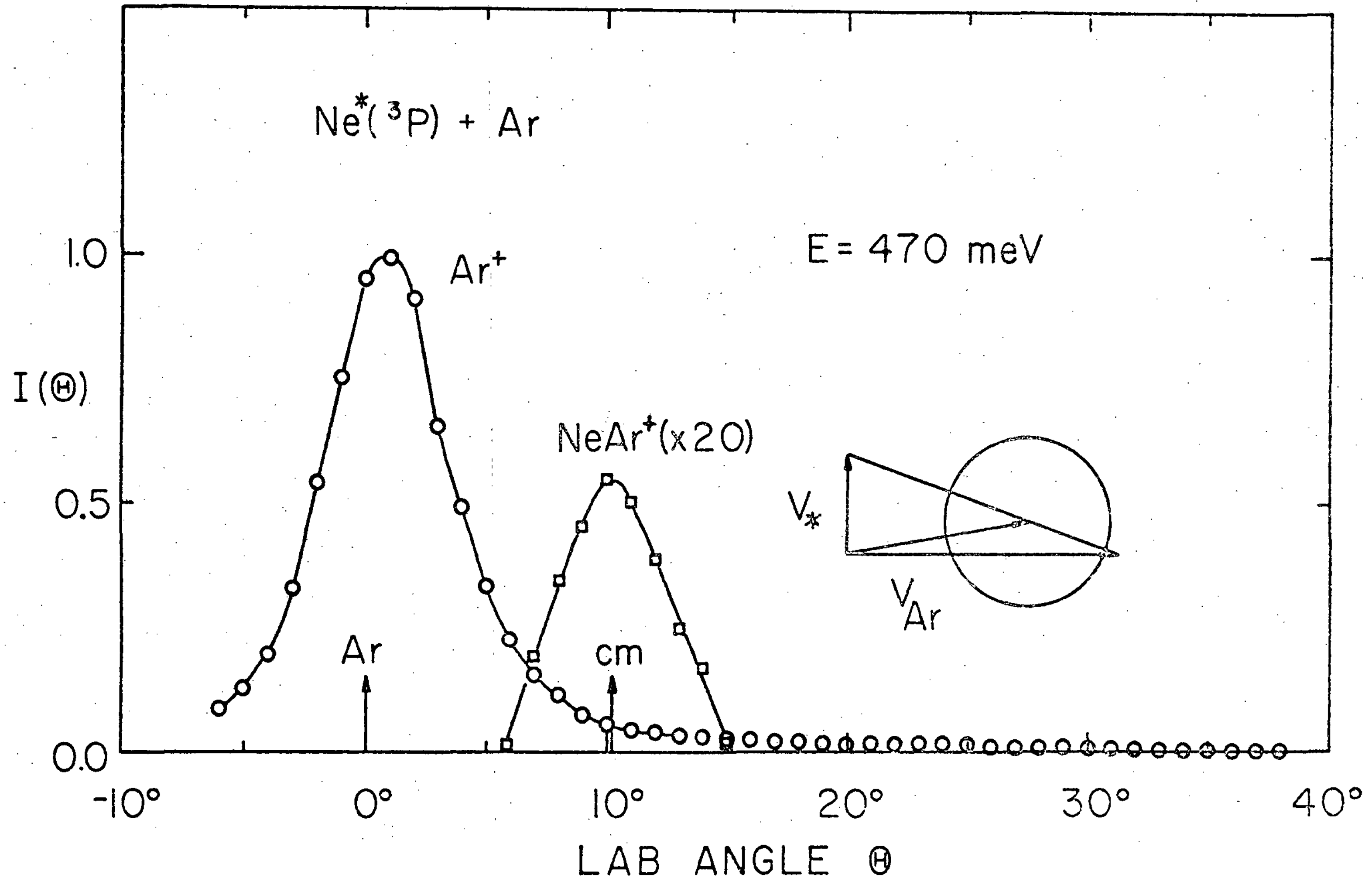

Ne*(³P) + Ar
E= 470 meV
Ar⁺
NeAr⁺(x20)
I(Θ)
1.0
0.5
0.0
Ar
cm
V*
V Ar
-10°
0°
10°
20°
30°
40°
LAB ANGLE Θ

Fig. 44

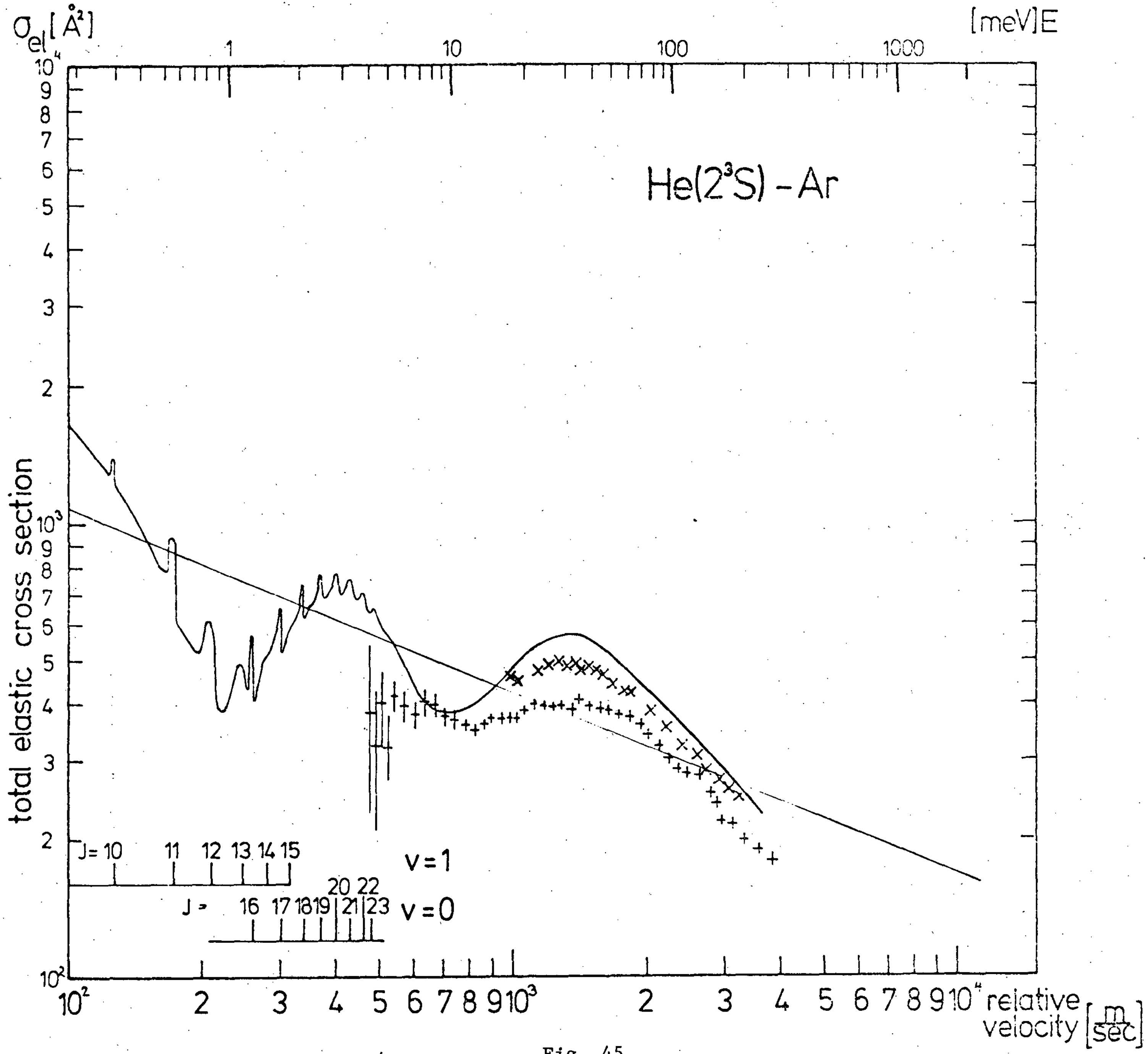

σel [Å²]
[meV]E
1
10
100
1000
10⁴
9
8
7
6
5
4
3
2
10³
10²
He(2³S) - Ar
total elastic cross section
J= 10
11
12
13
14
15
v=1
J =
16
17
18
19
20
21
22
23
v=0
10²
2
3
4
5
6
7
8
9
10³
10⁴
relative velocity [m/sec]

Fig. 45

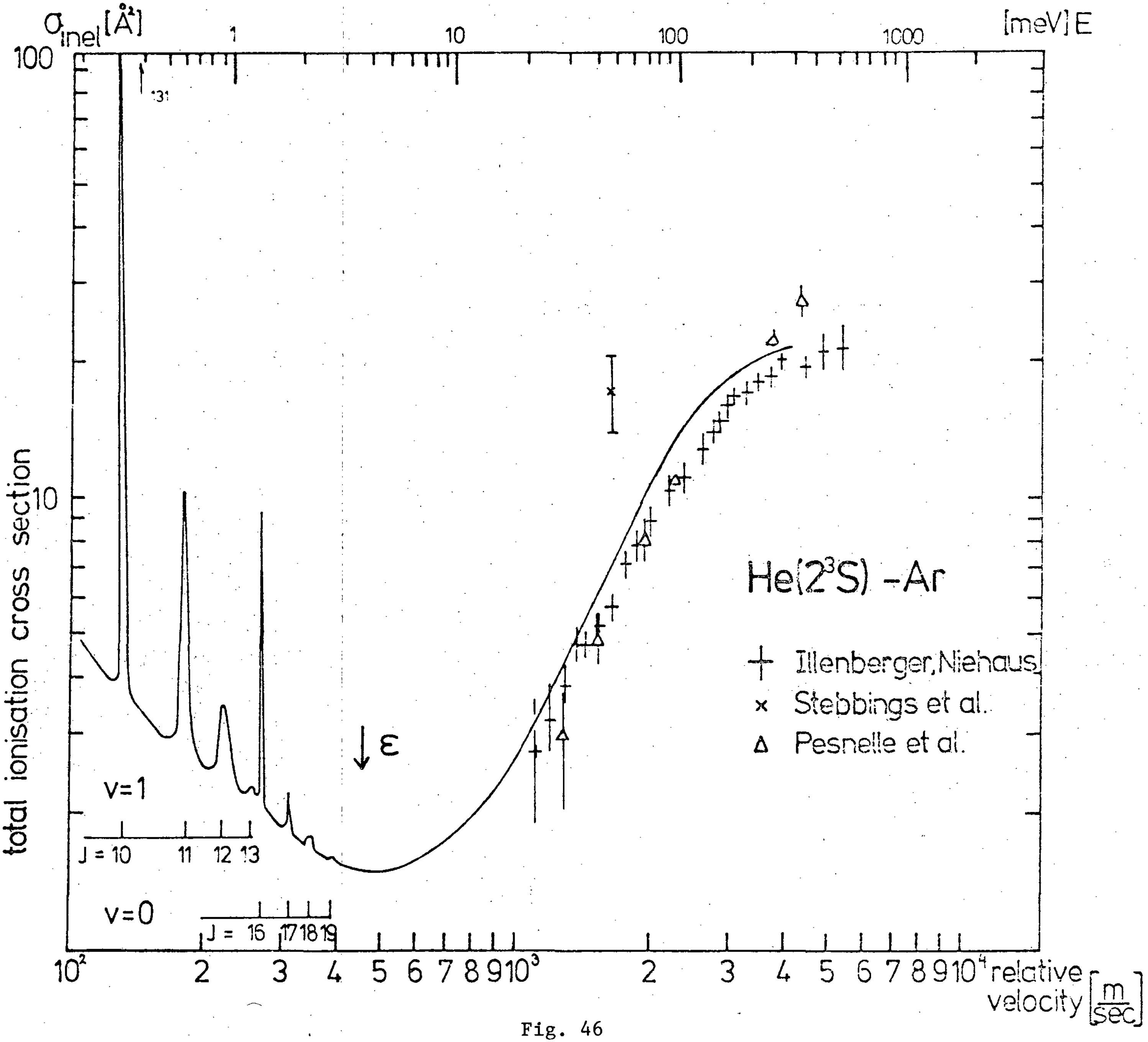

$\sigma_{inel}[\mathring{A}^2]$
1
10
100
1000
[meV] E
100
10
:31
total ionisation cross section
He(2^{3}S) -Ar
Illenberger, Niehaus
Stebbings et al.
Pesnelle et al.
↓ ε
v=1
J = 10
11
12
13
v=0
J = 16
17
18
19
10^2
2
3
4
5
6
7
8
9
10^3
2
3
4
5
6
7
8
9
10^4
relative velocity $\left[\frac{m}{sec}\right]$

Fig. 46

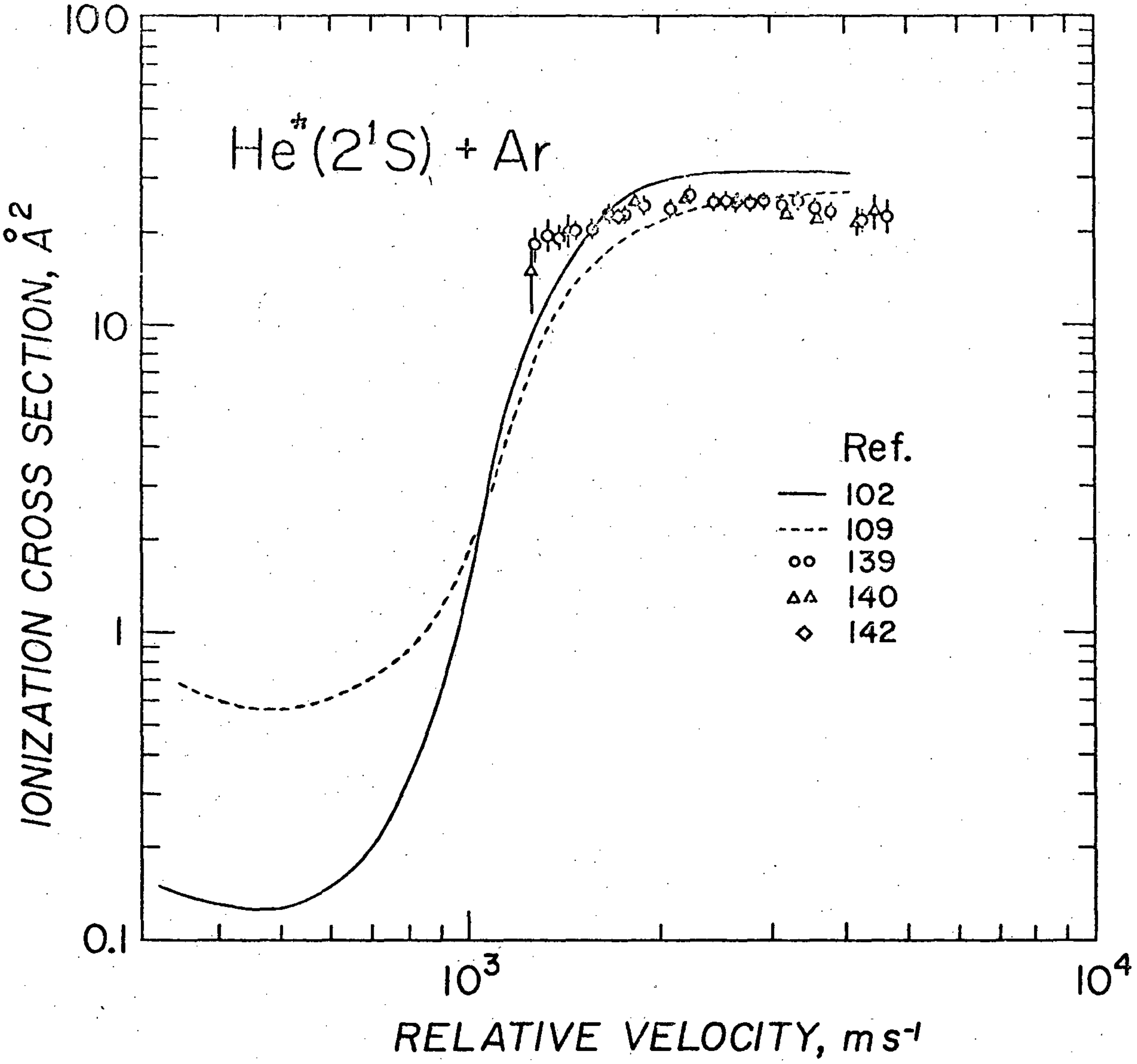

XBL 793-8779

Fig. 47

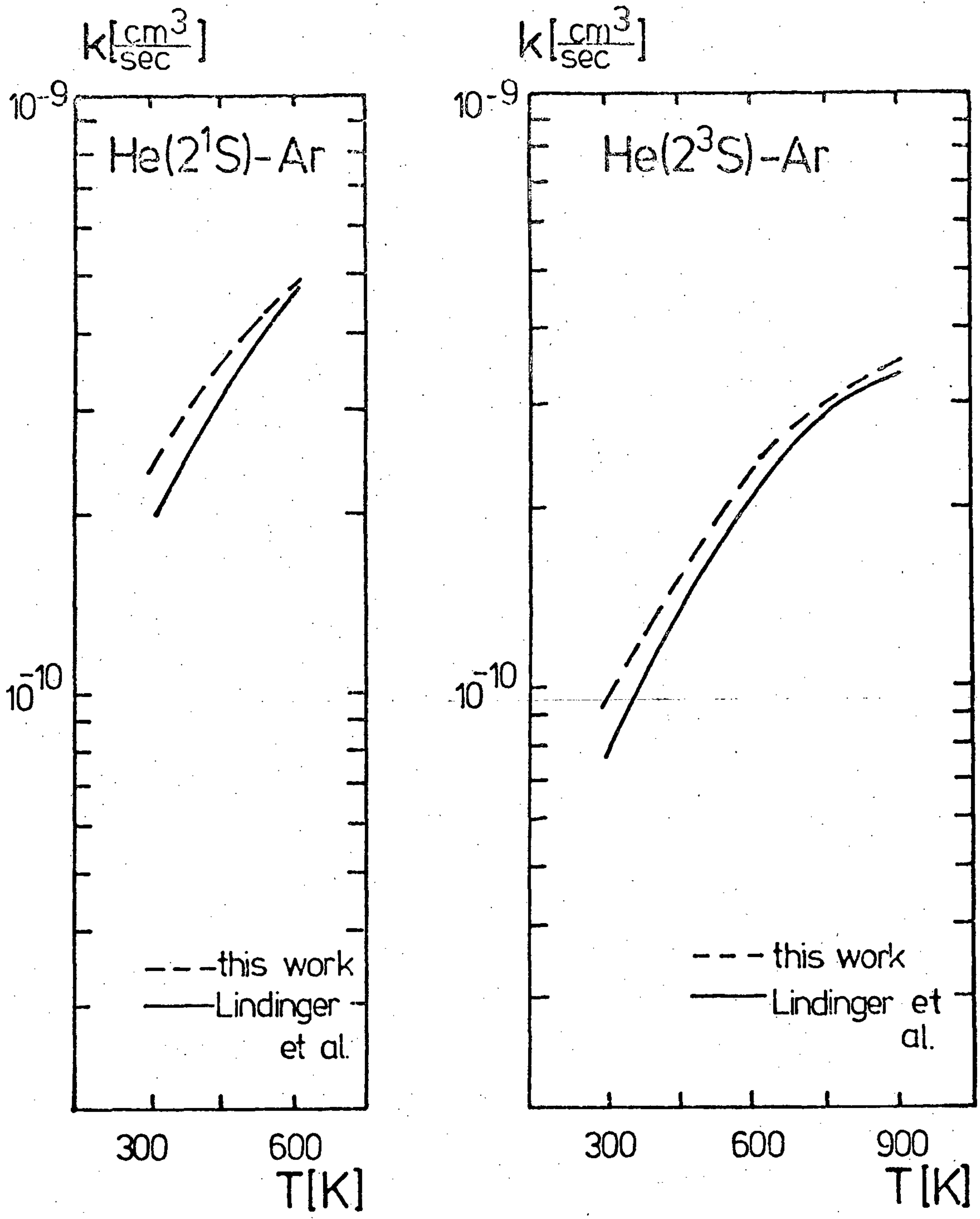
k[cm^3/sec]
10^-9
10^-10
He(2^1S)-Ar
- - - this work
—— Lindinger et al.
300
600
T[K]
k[cm^3/sec]
10^-9
10^-10
He(2^3S)-Ar
- - - this work
—— Lindinger et al.
300
600
900
T[K]

Fig. 48

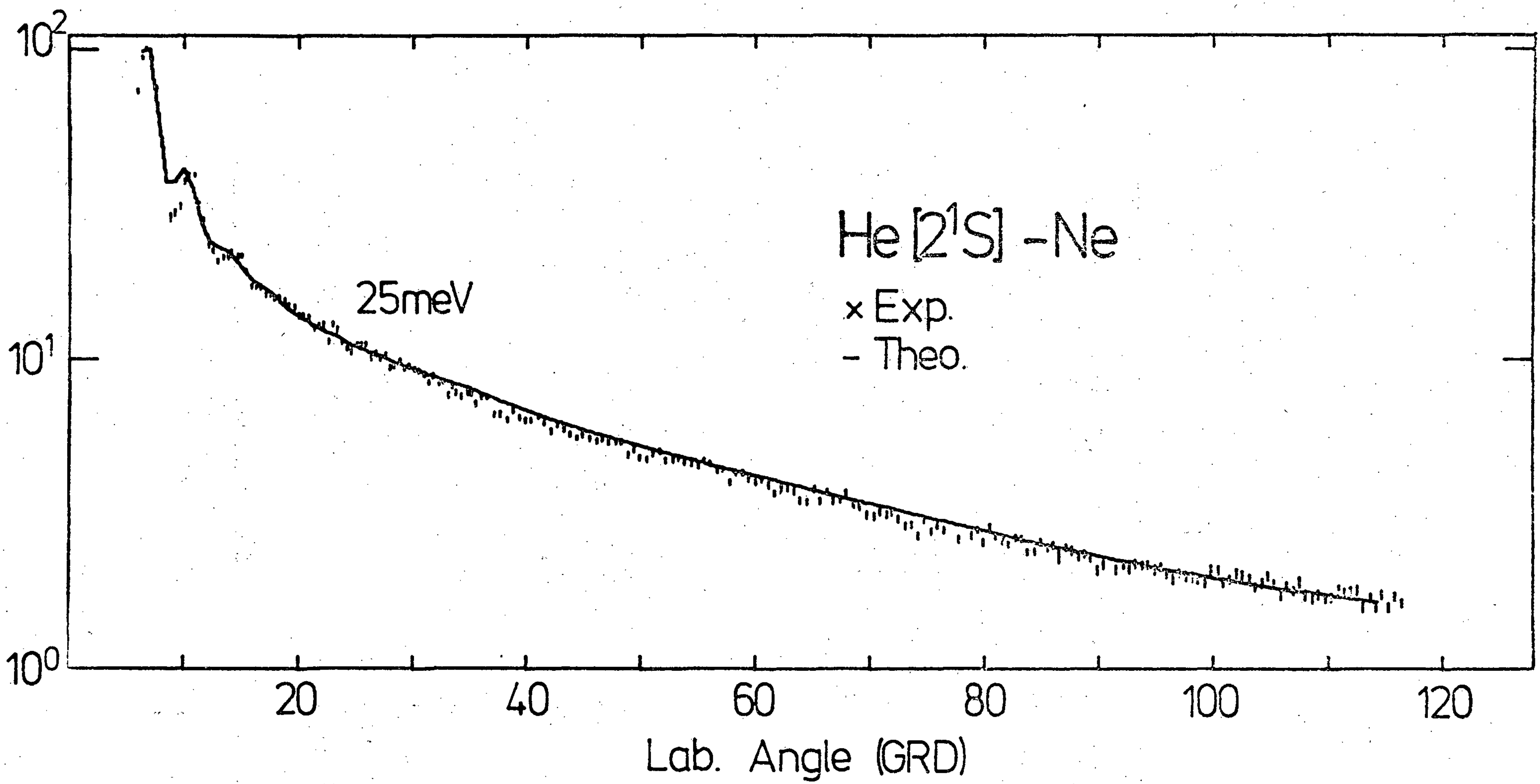
10²
10¹
10⁰
25meV
He [2¹S] -Ne
× Exp.
- Theo.
20
40
60
80
100
120
Lab. Angle (GRD)

Fig. 49

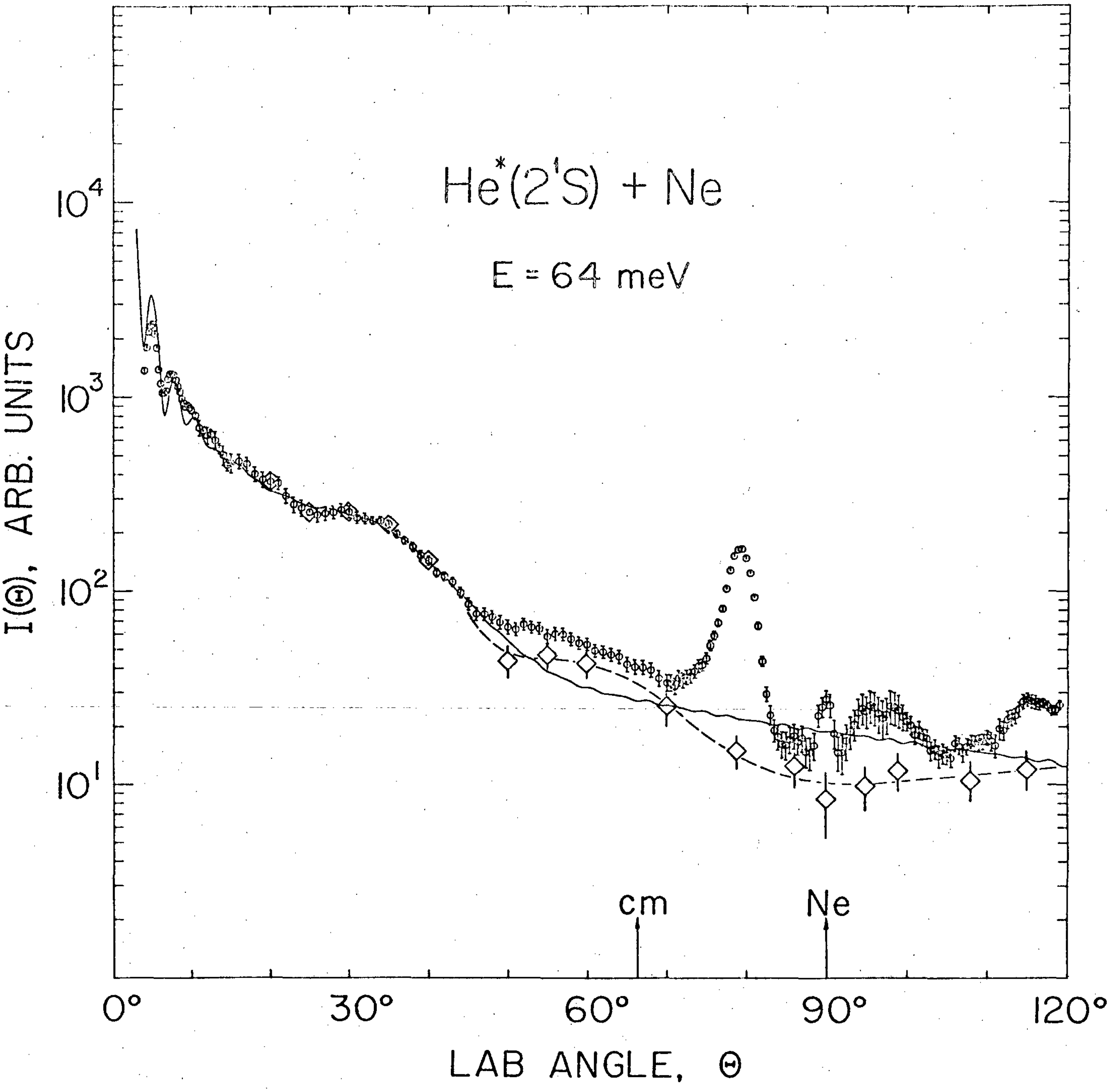

He*(2¹S) + Ne
E = 64 meV
10⁴
10³
10²
10¹
I(Θ), ARB. UNITS
cm
Ne
0°
30°
60°
90°
120°
LAB ANGLE, Θ

Fig. 50

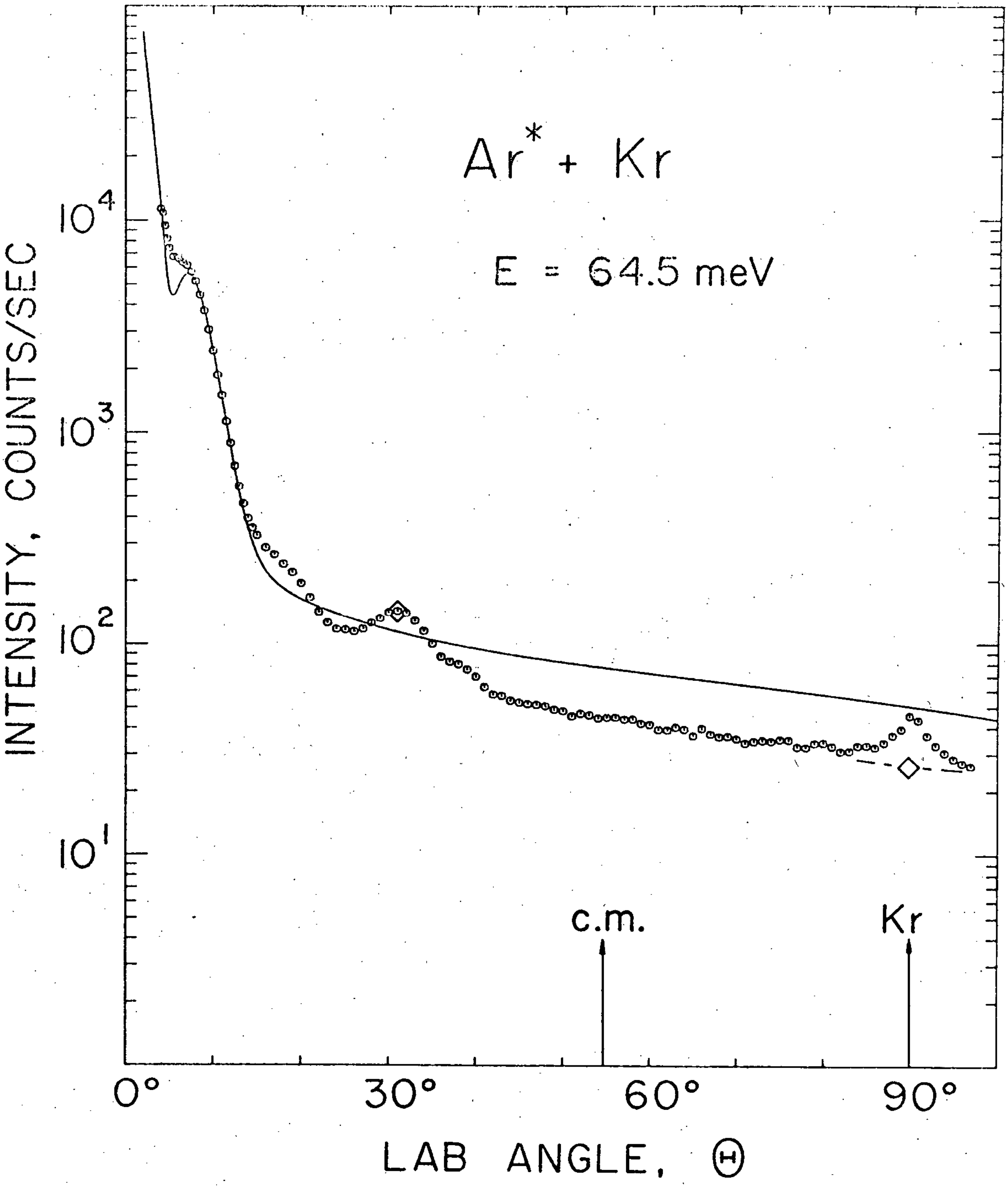

$Ar^* + Kr$
E = 64.5 meV
INTENSITY, COUNTS/SEC
10^4
10^3
10^2
10^1
c.m.
Kr
0°
30°
60°
90°
LAB ANGLE, Θ

Fig. 51

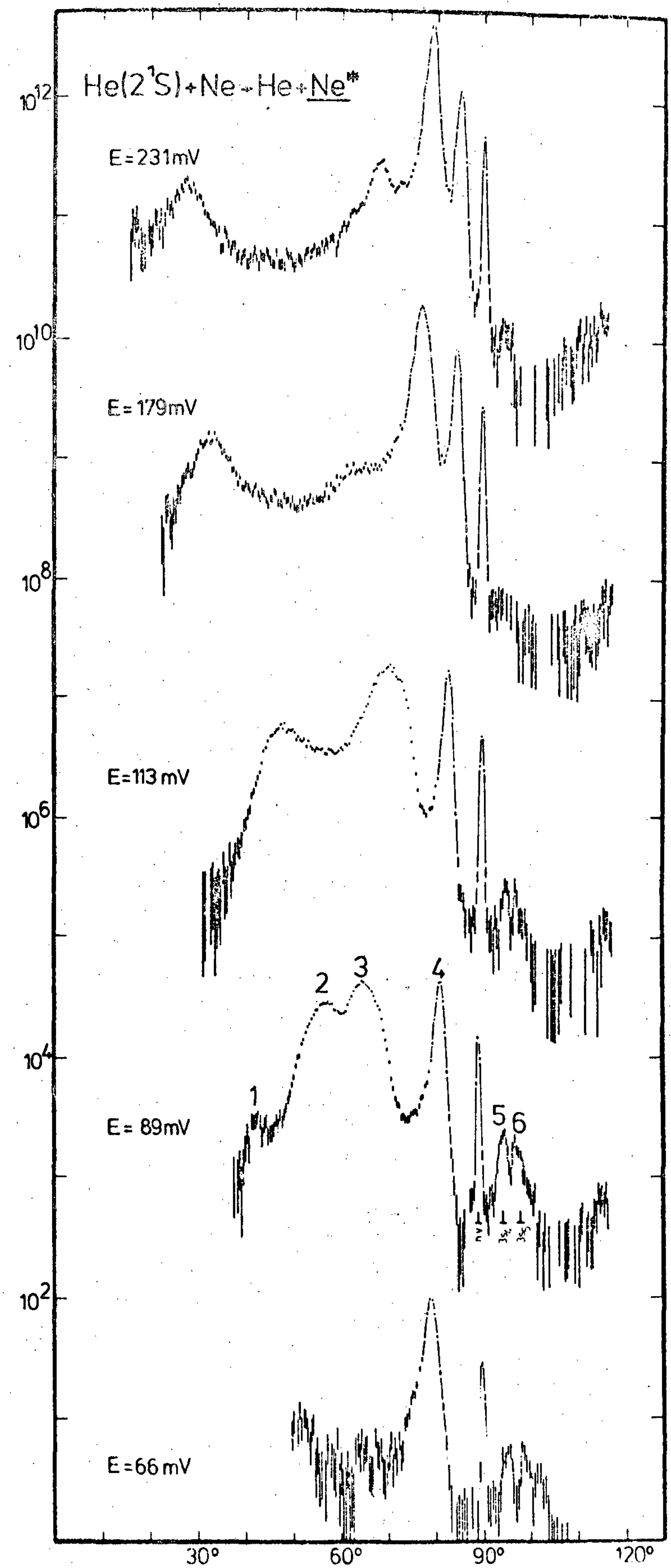

Laboratory differential cross section

Fig. 52

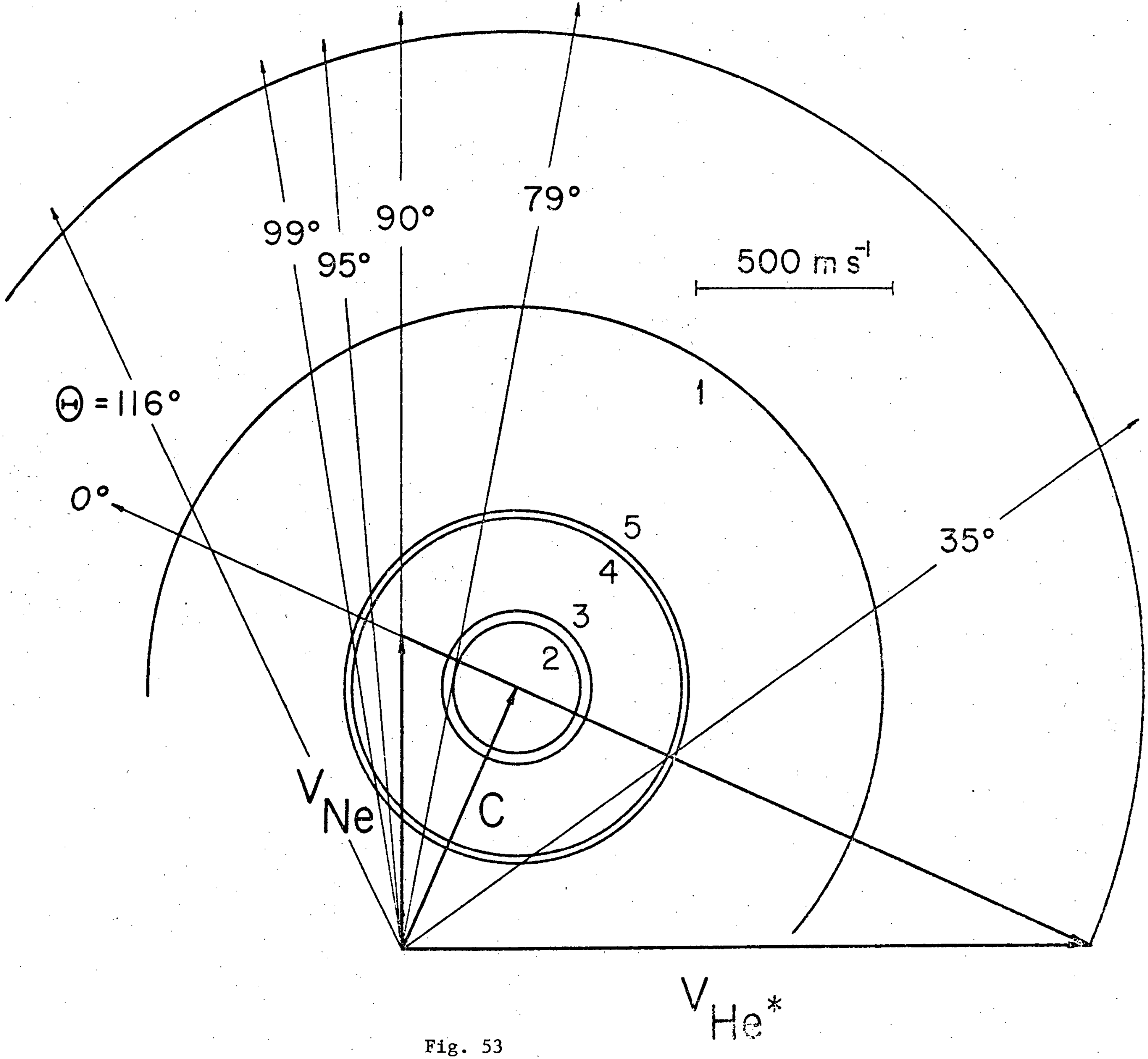

Fig. 53

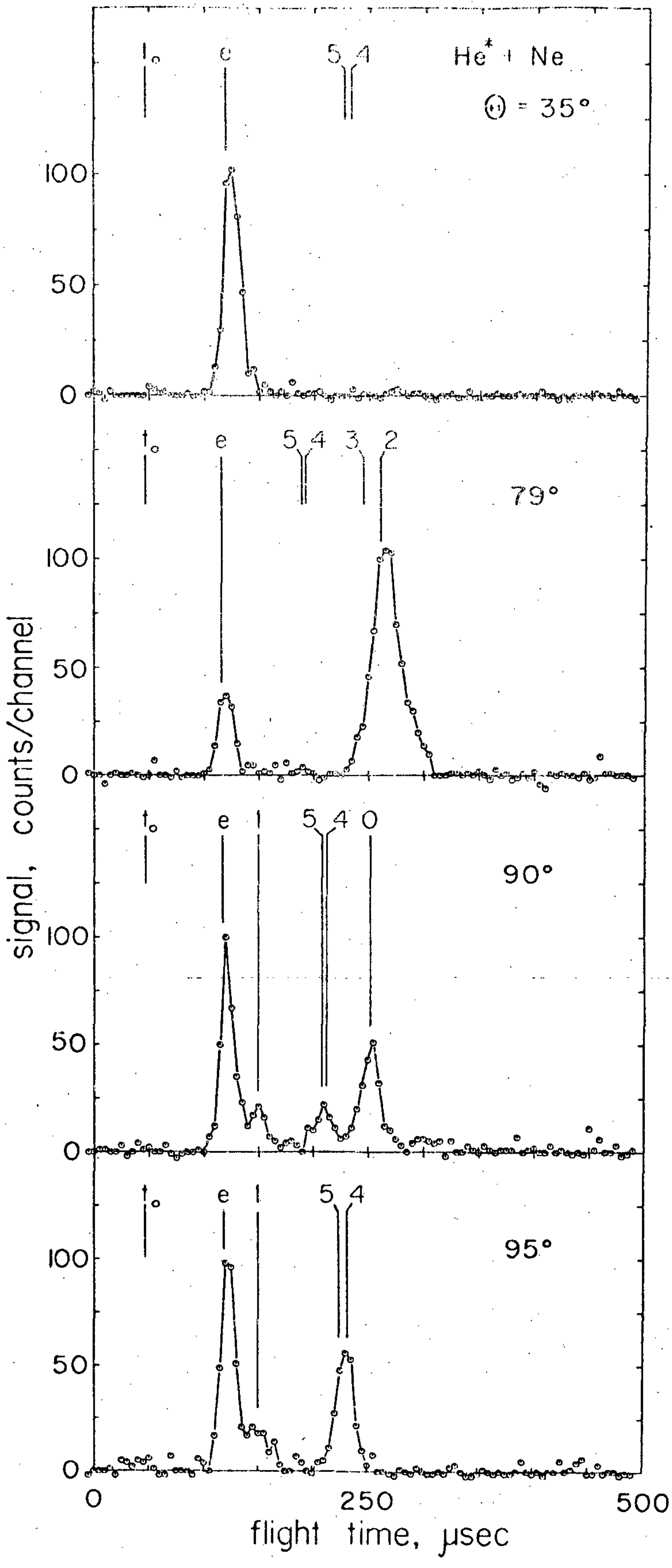
t₀
e
5 4
He* + Ne
Θ = 35°
79°
5 4 3 2
90°
e 1 5 4 0
95°
e 1 5 4
100
50
0
signal, counts/channel
0
250
500
flight time, μsec

Fig. 54

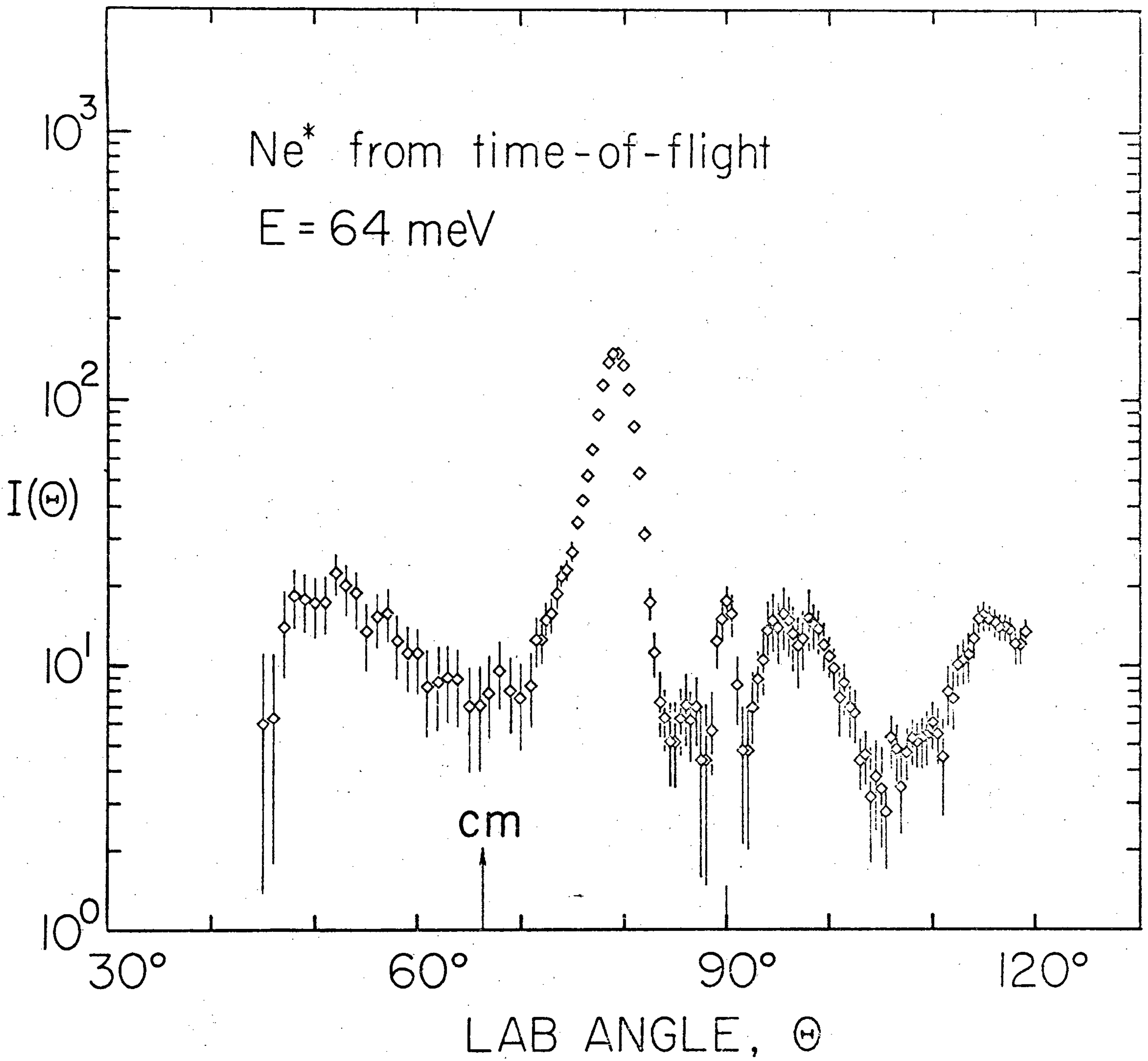
Ne* from time-of-flight
E = 64 meV
I(Θ)
10^0
10^1
10^2
10^3
30°
60°
90°
120°
cm
LAB ANGLE, Θ

Fig. 55

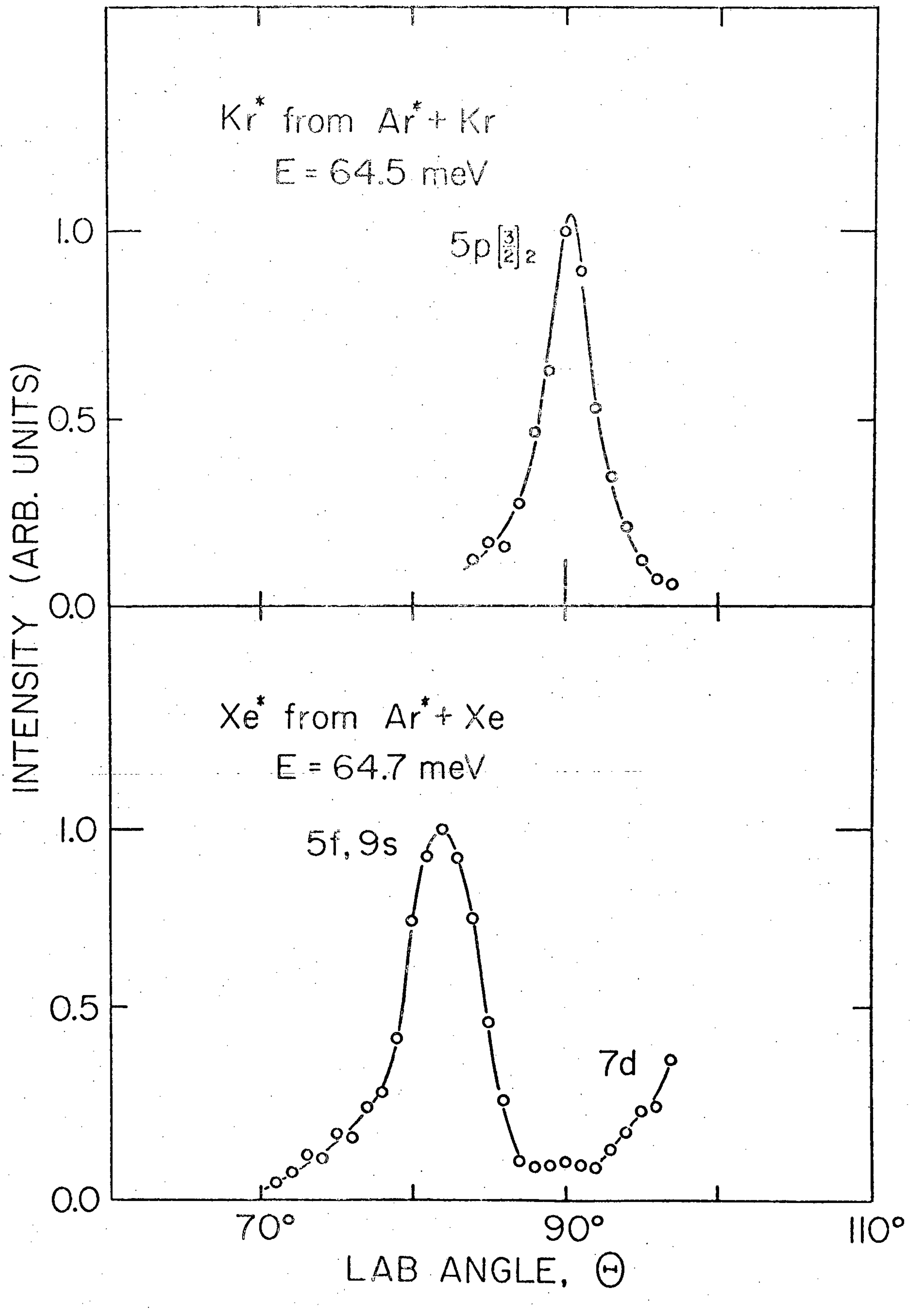
Kr* from Ar* + Kr
E = 64.5 meV
5p[3/2]2
Xe* from Ar* + Xe
E = 64.7 meV
5f, 9s
7d
INTENSITY (ARB. UNITS)
1.0
0.5
0.0
1.0
0.5
0.0
70°
90°
110°
LAB ANGLE, Θ

Fig. 56

TECHNICAL INFORMATION DEPARTMENT
LAWRENCE BERKELEY LABORATORY
UNIVERSITY OF CALIFORNIA
BERKELEY, CALIFORNIA 94720